First Test of the Performance of CMS Muon Chambers inside the Barrel Yoke

von

Emanuel Jacobi

Diplomarbeit in Physik

vorgelegt der

Fakultät für Mathematik, Informatik und
Naturwissenschaften
der Rheinisch-Westfälischen Technischen Hochschule Aachen

im Dezember 2008

angefertigt im

III. Physikalischen Institut A
Prof. Dr. Thomas Hebbeker

Abstract

The *Compact Muon Solenoid* (CMS) is a multi purpose experimental particle detector at the *Large Hardon Collider* (LHC). The goal of this experiment is to do fundamental research in particle physics and in particular to prove the validity of the Higgs model. The CMS muon barrel system provides a precise measurement of the position and the momentum of high energy muons. It consists of 250 drift tube chambers, with rectangular drift cells filled with a gas mixture of 85% Ar and 15% CO_2. Each chamber is equipped with on-chamber readout and trigger electronics.

The chambers for the innermost station have been produced at the Physics Institute IIIA at the RWTH University. After installing the chambers at their final position inside the barrel return yoke for the CMS solenoid magnet, cosmic muons have been recorded individually for all chambers and used to evaluate the detector performance, as this is the last chance to easily access the chambers for hardware interventions. These data also provide a good opportunity to study the reconstruction algorithms and to verify the chamber performance.

In this diploma thesis the work and studies from the chamber commissioning is presented, as well as reconstruction and performance studies.

Zusammenfasung

Der *Compact Muon Solenoid* (CMS) ist ein Vielzweck-Teilchendetektor am *Large Hadron Collider* (LHC). Die Zielsetzung dieses Experimentes ist es Grundlagenforschung im Bereich der Teilchenphysik zu betreiben, insbesondere das Higgs Modell zu überprüfen. Das Barrel Myon System des CMS Detektors erlaubt eine präzise Messung der Position eines Myons und seines Impulses. Es besteht aus 250 Driftkammern, mit rechteckigen Zellen, welche mit einer 85% Ar und 15% CO_2 Gasmischung gefüllt sind. Jede Kammer besitzt eine eingebaute Auslese- und Triggerelektronik.

Die Kammern des inneren konzentrischen Ringes des Myonendetektors wurden am III. Physikalischen Institut A an der RWTH Aachen produziert. Nach der Installation der Kammern an ihrem finalem Platz im Joch des CMS Solenoidmagneten wurde Myonen aus der kosmischen Strahlung mit den einzelnen Kammern gemessen. Die gewonnenen Daten wurden benutzt um die Eigenschaften der Kammern zu bestimmen. Ausserdem wurde intensiv nach möglichen Fehlern gesucht, da nach der Datennahme die Kammern final verkabelt wurden, was den Zugang zu den Kammern und damit Reparaturen sehr erschwert. Gleichzeitig sind mit diesen Daten Studien zu den Rekonstruktionsalgorithmen und der Qualität der Kammer möglich.

In dieser Diplomarbeit werden die Arbeitsschritte und Studien der Inbetriebnahme der Myonenkammern beschrieben, sowie Rekonstruktions- und Gütestudien.

Contents

1 Introduction

Nowadays, fundamental research in elementary particle physics is not a matter of some bright scientists and a well equipped lab, but of hundreds, even thousand scientists and a lab, that only internationally organized collaborations can afford.

The reason for that can be found in the mass-energy equivalence postulated by Albert Einstein in 1905. A particles rest energy equals the rest mass of the particle multiplied by the square of the speed of light in a vacuum. Consequently, the heavier a particle is, the more energy is needed to produce it.

In the last centuries the knowledge about nature has increased exponentially. This, inter alia, was supported by the easy and controlled access to large sources of energy. The length scales being under scrutiny became smaller and smaller, whereas the amount of energy increased continuously.

In terms of particle physics of the last century, after the discovery of the electron by J. J. Thomson the number of known subatomic particles increased rapidly, culminating in the particle zoo of the 1960s, where hundreds of different particles were discovered. The situation has been clarified with the development of the Standard Model of Particle Physics, the successful fundament for modern particle physics. Numerous predictions of the Standard Model have been verified in the last decades. But there is still one crucial missing link, together with several open questions.

Hence, a new experiment has been designed, with more energy, to advance deeper into the secrets of the nature. This experiment is the *Large Hadron Collider* (LHC) at the CERN laboratory near Geneva. This accelerator has been under construction for one decade, and has been completed in fall 2008. This experiment is one of the largest and most complex ever performed. More than 10 000 scientists and engineers from over 100 countries work together, trying to find the missing link in the Standard Model of Particle Physics.

The work performed for this diploma thesis took place at the *Compact Muon Solenoid* (CMS) experiment, where the debris from the particle collisions in the LHC are to be detected. The CMS detector consists of several subdetectors. One of them are the barrel muon chambers. About one quarter of them have been produced at the Physics Institute IIIA at the RWTH University. After installation of the chambers in their final position, they have undergone an intense test with cosmic muons, which is described in the following.

2 The Standard Model

The *Standard Model of Particle Physics* is a quantum field theory describing the known elementary particles and interactions among them. It is the basis of modern high energy physics. The Standard Model is based on very few preconditions: All fundamental interactions described in the Standard Model are deduced by the postulation of the existence of a symmetry. The Standard Model is a very successful theory. It describes most of the phenomena discovered in the experiments of particle physics very accurately and makes many predictions which could be verified in experiments with very good precision, although the theory is yet not adequately tested and still leaves many open questions. By now it is *the* tool for particle physics and the scrutiny of the model is the main task for particle physicists nowadays. In the following, the main ingredients of the Standard Model as well as the theoretical foundations will be discussed.

2.1 Fermions

Fermions are the particles of matter. All known types of matter, including the whole "zoo" of particles discovered in the 20th century, are composed of fermions. There are twelve basic fermions, complemented by their anti-particles. They all have half-integer spin and consequently, according to the *Pauli exclusion principle*, two identical fermions must not be in the same quantum state. There are two types of fermions: *leptons* and *quarks*. Both appear in three generations, which only differ by their masses. Each generation contains two particles and their respective anti-particles.

2.1.1 Leptons

Leptons are particles undergoing weak interaction, the electrically charged leptons additionally undergo electromagnetic interaction [1]. The most familiar lepton is the electron e^-. It is a stable particle. Together with the electron-neutrino ν_e and their anti-particles positron e^+ and anti-electron-neutrino $\bar{\nu}_e$ they form the first lepton generation. The second lepton generation is formed by the muon μ^-, the muon-neutrino ν_μ and their antiparticles. The muon is more than 200 times heavier

[1] Of course all massive particles additionally undergo gravitation. However, gravitation is not covered by the Standard Model and its influence is negligible in todays particle physics experiments.

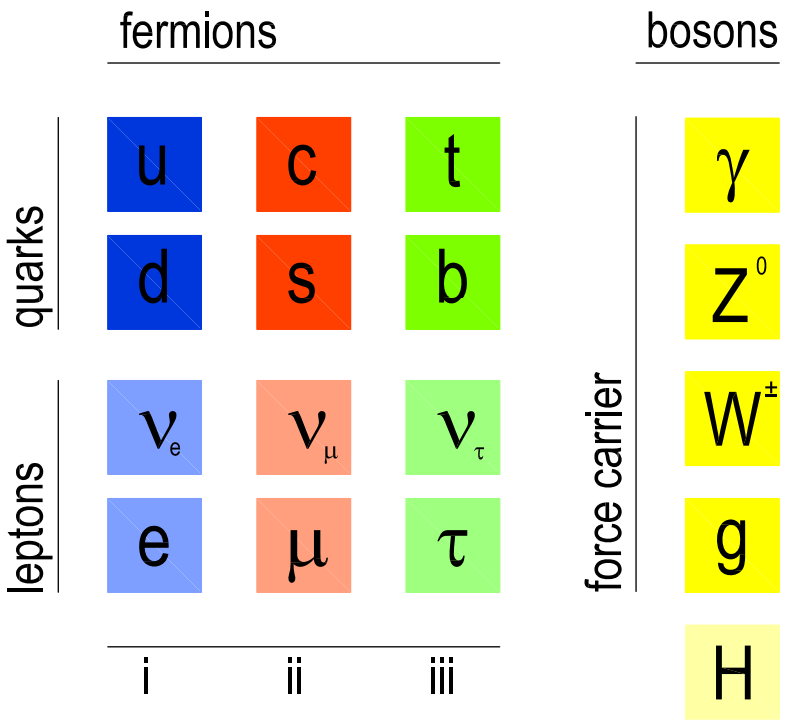

Figure 2.1: *Particles in the Standard Model. Fermions occur in three generations (i,ii,iii). The Higgs boson (H) is predicted, but not yet proofed.*

than the electron. It is not stable and has a mean lifetime of about 2.2μs. The third lepton generation consists of the tau τ^-, a particle nearly 3500 times heavier than the electron with a mean lifetime of $2.9 \cdot 10^{-13}$s, the tau-neutrino ν_τ and their antiparticles.

2.1.2 Quarks

Quarks are particles interacting with strong, weak and electromagnetic force. Six types of quarks, called flavors, are distinguished: *up, down, charm, strange, top* and *bottom*. They all have a fractional electric charge of either $q = {}^2/_3\,\mathrm{e}$ (u, c, t) or $q = -{}^1/_3\,\mathrm{e}$ (d, s, b).

Quarks were first postulated in 1963 by Murray Gell-Mann and George Zweig to explain the numerous discovered hadrons, called the particle zoo. In the quark model hadrons, strongly interacting particles comprise *baryons*, particles composed out of three quarks and *mesons*, particles made up of a quark anti-quark pair. With this model it was possible to predict new hadrons and explain why certain hadrons do not exist.

To avoid the violation of the Pauli exclusion principle Oscar W. Greenberg introduced in 1964 an additional property of the quarks, color. Color is the charge of the strong interaction. Each quark carries a color charge of one of the three colors *red, green* or *blue*, antiquarks carry the corresponding anti-color. All three colors

combine - like visual additive colors do in the RGB model - to white and so do color and anti-color. Observable particles must be white. As a consequence, quarks do not appear as free particles since the strong interaction increases with distance. I.e. for the attempt of separating the two quarks of a meson, so much energy is needed, that immediately a new pair of quarks would be produced out of the vacuum, resulting in two mesons. This characteristics is called *color confinement*. Only for distances converging towards zero, quarks nearly act as free particles. This is called *asymptotic freedom*.

2.2 Bosons

Particles with an integer spin are called bosons. All particles mediating force are bosons. The electromagnetic force is mediated by the *photon*, a massless spin 1 particle. The weak interaction is carried by three massive spin 1 particles: The two electrically charged W^+ and W^- bosons and the electrically neutral Z^0 boson. The strong interaction is mediated by eight gluons, massless spin 1 particles, carrying color and anti color. Since gluons carry the charge they mediate, they can interact with themselves.

force	**relative strength**	**range** [m]	**carrier**
gravitation	$\approx 10^{-39}$	∞	graviton ?
weak	$\approx 10^{-6}$	10^{-18}	W, Z
electromagnetic	$\approx 10^{-2}$	∞	γ
strong	$\approx 10^{0}$	10^{-15}	8 gluons

Table 2.1: *The four fundamental forces with their range and approximate relative strength. (The exact value depends on the momentum transfer.)*

2.3 Gauge Theories

2.3.1 Noether's Theorem

Any continuous symmetry in nature implies a conservation law and vice versa, every conservation law implies a continuous symmetry. This fundamental proposition was first published in a theorem by Emmy Noether in 1918 [1]. For example the principle of conservation of energy is a consequence of the invariance under time translations.

Considering a set of fields $\{\Phi\} := \{\Phi_a(x)\} \mid a = 1, 2, \ldots, M$ with a Lagrangian $\mathcal{L} = \mathcal{L}(\{\Phi\}, \{\partial\Phi\}; x)$, equations of motion given by the Euler-Lagrange equation

$$d_\mu \frac{\partial \mathcal{L}}{\partial(d_\mu \Phi_a)} - \frac{\partial \mathcal{L}}{\partial(\Phi_a)} = 0 \qquad , \quad a = 1, 2, \ldots, M \tag{2.1}$$

and a transformation

$$\Omega = \mathbb{1} + \omega + \mathcal{O}(\omega)^2 \tag{2.2}$$

transforming the coordinates

$$x^\mu \xrightarrow{\Omega} \tilde{x}^\mu := x^\mu + \alpha^\mu \cdot \omega + \mathcal{O}(\omega^2) \tag{2.3}$$

and the fields

$$\Phi_a(x) \xrightarrow{\Omega} \tilde{\Phi}_a(x) := \Phi_a(x) + \beta_a \cdot \omega + \mathcal{O}(\omega^2) \quad . \tag{2.4}$$

The Noether current is then defined [2] as:

$$\mathbf{N}^\mu(x) := \sum_a \frac{\partial \mathcal{L}}{\partial(d_\mu \Phi_a)} \cdot \{\alpha^\nu d_\nu \Phi_a - \beta_a\} - \mathcal{L} \cdot \alpha^\mu \tag{2.5}$$

Noethers theorem reads as follows:

$$d_\mu \mathbf{N}^\mu = 0, \tag{2.6}$$

If the action integral of the system's Lagrangian is invariant under a transformation Ω, then the Noether current $\mathbf{N}^\mu$ is conserved. The conserved quantity can be obtained by spatial integration of the Noether current's time component:

$$\mathbf{Q} := \int_{\text{space}} \mathbf{N}^t d^3x \tag{2.7}$$

2.3.2 Local Gauge Invariance

The interplay between symmetries and conservation laws does not solely connect the classic quantities of conservation like energy, momentum, angular momentum, etc. with underlying symmetries, but it is simultaneously crucial for a whole class of theories, viz. the gauge theories. The underlying symmetry for them is the invariance under *local gauge transformations*, i.e gauge transformations depending on a point in the space-time manifold. According to the state of knowledge all fundamental interactions can be described as local gauge theories. This concept has been introduced by Hermann Weyl in 1918 [3, 4] for the electromagnetic interaction. Chen Ning Yang and Robert Mills generalized this concept in 1954 [5].

In modern particle physics interactions between elementary particles are not described by the effect of a force, but by the exchange of other particles, viz. the gauge bosons.

The Gauge Theory of Quantum Electrodynamics

To illustrate the principle of a gauge theory, in the following Quantum Electrodynamics (QED) will be presented as gauge theory. The deduction follows the explanations from [6] and [7].

The starting point is the *dirac equation* describing a free fermion:

$$(i\gamma^\mu \partial_\mu - m)\Psi = 0 \tag{2.8}$$

The corresponding Lagrangian of a free fermion reads then

$$\mathcal{L} = \bar{\Psi}(i\gamma^\mu \partial_\mu - m)\Psi \quad , \tag{2.9}$$

Considering a unitary transformation:

$$\Psi \rightarrow \Psi' = U\Psi \qquad U = e^{i\alpha} \tag{2.10}$$

One has the freedom to apply the aforementioned transformation, the so-called *gauge transformation*, because it does not change the measured quantity, due to the fact that the probability density $\bar{\Psi}\Psi$ remains unchanged, as the additional exponential factors cancel each other.

Two cases can be distinguished. First, let the phase α be independent from time and space. In this case U is called a *global gauge transformation*. The additional phase is applied globally, and thus everywhere and every time the same. It can be easily verified that $\mathcal{L}$ is invariant under the transformation U, with the conserved current $\partial_\mu(Q\bar{\Psi}\gamma^\mu\Psi) = 0$ and the conserved quantity is the charge Q.

The phase being global is an aesthetically unsatisfactory limitation, as one point in space-time does not "know" about the other point's phases. According to Einstein's relativity principle, the information about them should not be exchanged faster than the speed of light. It should be possible to apply the transformation to different spatial points independently from each other, since it is not clear how these spatial points are causally connected. This leads to the second case, the phase $\alpha = \alpha(x)$ depends on time and space, i.e. it may be chosen arbitrarily. In this case $U = U(x)$ is the so-called *local gauge transformation*. But the Lagrangian $\mathcal{L}$, as written in equation 2.9 is not invariant under the transformation $U(x)$ anymore, due to the fact that it contains a derivative which leads to an additional term $\propto \partial_\mu\alpha(x)$ in the transformed Lagrangian.

The clue about the gauge theories is to postulate [2] the invariance of the Lagrangian under local gauge transformations. To receive the local gauge invariance an additional field, viz. the *gauge field* is introduced: A spin 1 vector field A_μ. When performing the transformation $U(x)$ on Ψ, the gauge field has to be transformed too:

$$A_\mu \rightarrow A'_\mu = A_\mu + \frac{1}{Q} \cdot \partial_\mu\alpha(x) \tag{2.11}$$

The gauge field is introduced into to the Lagrangian by replacing the derivative ∂_μ by the covariant derivative $D_\mu = \partial_\mu - iQA_\mu$.
This replacement, called *minimal substitution*, allows to construct a Lagrangian that is invariant under local gauge transformations. Now, the Lagrangian reads as follows:

$$\mathcal{L} = \bar{\Psi}(i\gamma^\mu D_\mu - m)\Psi = \bar{\Psi}(i\gamma^\mu\partial_\mu - m)\Psi + Q\bar{\Psi}\gamma^\mu\Psi A_\mu \tag{2.12}$$

[2] Physicists like "beautiful theories". The limitation on the global gauge invariance mentioned above, is a flaw of the theory, but does not compellingly lead to the local gauge invariance.

The original version of the Lagrangian 2.9 has been expanded by the term

$$Q\bar{\Psi}\gamma^{\mu}\Psi A_{\mu} = j^{\mu}A_{\mu} \tag{2.13}$$

The vector field A_μ can be identified as the photon-field, which couples to the electron current j^μ. The associated gauge boson is the photon. Thus electromagnetic interactions are mediated by the exchange of photons. To complete the Lagrangian of QED a term for the free photon must be appended. The *Proca-Lagrange Function* describes a spin 1 vector field and provides the missing part:

$$\mathcal{L} = -\frac{1}{4}\cdot F^{\mu\nu}F_{\mu\nu} + \frac{1}{2}\cdot m_A^2 A^{\nu}A_{\nu} \quad , \tag{2.14}$$

with $F^{\mu\nu} = \partial^\mu A^\nu - \partial^\nu A^\mu$. The first term of the Proca-Lagrange Functions is invariant under local gauge transformation, but the second term $\propto m_A^2 A^\nu A_\nu$ spoils the invariance. Fortunately for massless gauge bosons $m_A = 0$ the second term vanishes. The gauge boson has to be massless, which is true for the photon.

The final Lagrangian of QED taking the minimal substitution and free photons into account reads:

$$\mathcal{L} = \underbrace{\bar{\Psi}(i\gamma^{\mu}\partial_{\mu} - m)\Psi}_{\substack{\text{kinetic term and mass for } \Psi \\ \text{(electron-field)}}} - \underbrace{\frac{1}{4}F^{\mu\nu}F_{\mu\nu}}_{\substack{\text{kinetic term for } A_\mu \\ \text{(photon-field)}}} + \underbrace{Q\bar{\Psi}\gamma^{\mu}\Psi A_{\mu}}_{\text{interaction term}} \tag{2.15}$$

Now the elegance of gauge theories can be seen: Just by postulating local gauge invariance a complete theoretical description of the electron-photon interaction can be obtained. The described symmetry is based on the abelian $U(1)_{EM}$ group with the electric charge as conserved quantity.

2.3.3 The Glashow, Weinberg, Salam Model meets Quantum Chromodynamics

QCD

The strong interaction is described by quantum chromodynamics (QCD). It is a non abelian gauge theory with the symmetry group $SU(3)_C$, the group of local gauge transformations in the three dimensional color-space. The color is the charge of the strong interaction and can be *red*, *blue* or *green*. The Lagrangian of QCD is invariant under transformations from the $SU(3)_C$ group. There are eight generators for this group, the linearly independent and hermitian *Gell-Mann* matrices $t^s = {}^1\!/_2\lambda^s$ with $s = 1 \ldots 8$. With the minimal substitution

$$D^{\mu} = \partial^{\mu} - igt_sG^{s,\mu} \tag{2.16}$$

in the Lagrangian, eight gauge fields G_μ, viz the *gluon fields* are introduced, corresponding to the eight generators, and eight massless gauge bosons, the *gluons* are

associated with these gauge fields. g is the coupling constant of QED. Unlike the photons in QED, gluons are both, part of the field and carrier of the field. Since they carry color, gluons can interact with other gluons. Every gluon carries one unit of color and one unit of anti-color. The strong interaction is flavor independent, i.e. the strength of the strong coupling is the same for all types of quarks. For high energies and for very short distances, the strength of the strong interaction decreases. Thus inside nucleons, the quarks and gluons can move as free, non-interacting particles, if probed in high p_T interactions. This is the *asymptotic freedom*, mentioned in section 2.1.2.

GWS

In the 60s of the 20th century Sheldon Lee Glashow, Steven Weinberg and Abdus Salam described a theoretical unification of QED and the weak interaction, the electroweak interaction. The so-called Glashow-Weinberg-Salam (GWS) theory is a non-abelian gauge theory with the symmetry group $SU(2)_L \times U(1)_Y$. The Lagrangian of the electroweak interaction is invariant under local gauge transformations from this group. $SU(2)_L$ is the weak isospin group which only has effect on left-handed fermion doublets. $U(1)_Y$ is the group of the weak hypercharge which additionally couples to the right-handed fermion singlets. Thus the electroweak interaction violates the parity maximally, as shown in the experiment by Chien-Shiung Wu in 1957 [8]. The boson fields of the electroweak interaction $A, Z, W^{\pm}$ are mixed states of the Lagrangian gauge fields:

$$\begin{aligned} A &= \cos\theta_W \cdot B + \sin\theta_W \cdot W^3 \\ Z &= -sin\theta_W \cdot B + \cos\theta_W \cdot W^3 \\ W^+ &= \frac{W^1 + iW^2}{\sqrt{2}} \\ W^- &= \frac{W^1 - iW^2}{\sqrt{2}} \end{aligned} \tag{2.17}$$

The angle θ_W, viz the *Weinberg Angle* is a free parameter and cannot be predicted. The weak neutral current which describes interactions mediated by the electrically neutral Z boson was first described in the GWS theory. The existence of weak neutral currents has experimentally been proven in 1973 [9] with the Gargamelle bubble chamber at CERN. The first sight of a neutral current event took place in Aachen, where Gargamelle data was scanned (see figure 2.2).

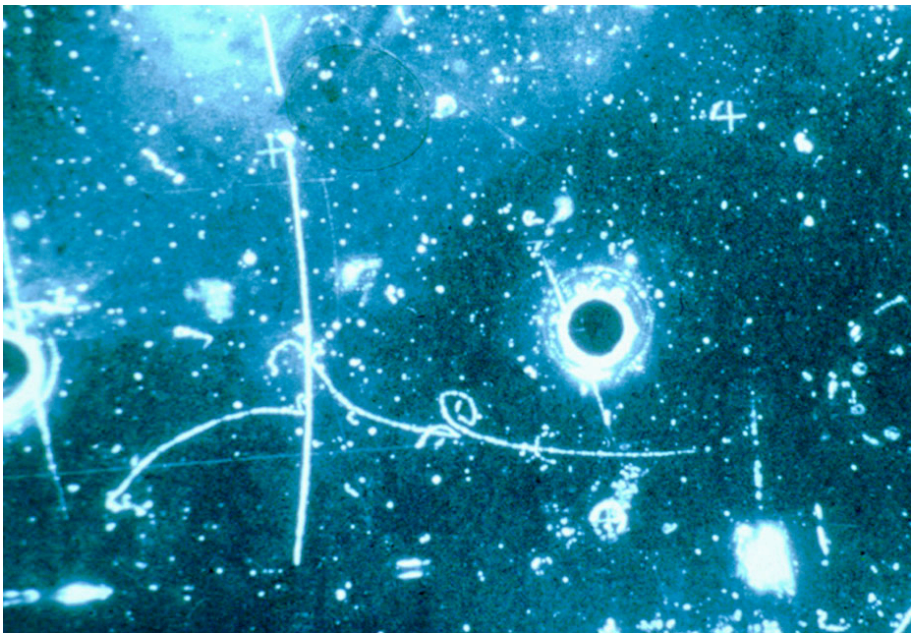

Figure 2.2: *Neutral current event from the Gargamelle bubble chamber. This event was the first sight of a neutral current. A neutrino interacts with an electron (horizontal track) and emerges as a neutrino, without producing a muon. [10].*

In 1979 Glashow, Weinberg and Salam won the Nobel prize for *"for their contributions to the theory of the unified weak and electromagnetic interaction between elementary particles, including, inter alia, the prediction of the weak neutral current"* [11].

The combination of the theory of quantum chromodynamics with the Glashow-Weinberg-Salam theory forms the basis of the Standard Model:

$$SU(3)_C \otimes SU(2)_L \otimes U(1) \tag{2.18}$$

The Lagrangian of the Standard Model reads as follows:

$$\mathcal{L}_{\text{SM}} = \mathcal{L}_{\text{Fermion}} + \mathcal{L}_{\text{Gauge}} + \mathcal{L}_{\text{Higgs}} + \mathcal{L}_{\text{Yukawa}} \tag{2.19}$$

2.3.4 The Higgs Mechanism

The gauge bosons have to be massless, as pointed out above. Photons and gluons are massless, but $W^{\pm}$ and Z are heavy particles with $m_W = (80.403 \pm 0.029)\text{GeV}$ and $m_Z = (91.1876 \pm 0.0021)$ [12]. The mass of these bosons is the reason for the short range of the weak interaction [3]. Thus the local gauge invariance of the Lagrangian of the electroweak interaction is spoiled. A method to re-construct the local gauge invariance is given by the spontaneous symmetry breaking.

[3] The massless gluons could mediate a long range interaction, but due to the absence of a color-singlet and the quark confinement only short range strong interactions can occur. [6]

A symmetry is broken spontaneously, if the Lagrangian is always invariant under transformations from a specific symmetry group, but not the vacuum state. To obtain this, the complex, scalar isospin doublet

$$\Phi = \begin{pmatrix} \phi^+ \\ \phi^0 \end{pmatrix} = \frac{1}{\sqrt{2}} \begin{pmatrix} \phi_1 + i\phi_2 \\ \phi_3 + i\phi_4 \end{pmatrix} \tag{2.20}$$

which couples to the gauge bosons of the $SU(2) \times SU(1)$ symmetry, with the Lagrangian

$$\mathcal{L} = (D_\mu \phi)^\dagger (D^\mu \phi) - V(\phi) \tag{2.21}$$

and the so-called *Higgs potential* $V(\phi)$

$$V(\phi) = -\mu^2(\Phi^\dagger \Phi) + \lambda^2(\Phi^\dagger \Phi)^2 \tag{2.22}$$

is introduced.

The constraint for the vacuum state of the Higgs potential is:

$$\Phi^\dagger \Phi = \frac{1}{2}(\phi_1^2 + \phi_2^2 + \phi_3^2 + \phi_4^2) = \frac{1}{2}v^2 \qquad v \equiv \frac{\mu}{\lambda} \tag{2.23}$$

with $\lambda^2 > 0$ and $\mu^2 > 0$. Figure 2.3 shows an illustration of this potential.

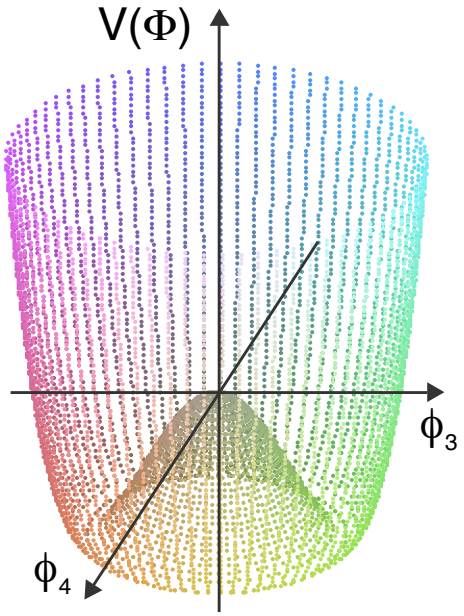

Figure 2.3: *Higgs potential. This potential has a local maximum at the origin, surrounded by a ring of local minima. By choosing a specific minimum state the symmetry is broken spontaneously.*

There is an infinite number of ground states which all fulfill the constraint 2.23, as to be seen in figure 2.3. To identify the mass term, the Lagrangian has to be given in other field variables. They are obtained by expanding the field around

a specific vacuum state, using perturbation theory. To avoid massive photons the specific vacuum state is chosen in a manner that the Lagrangian remains invariant under transformations from the $U(1)_{EM}$ symmetry group of the electromagnetic interaction. Hence ϕ^+ is set to zero and the vacuum state is chosen as:

$$\Phi_0 = \frac{1}{\sqrt{2}} \begin{pmatrix} 0 \\ v \end{pmatrix} \tag{2.24}$$

By choosing a specific vacuum state, the symmetry has been broken spontaneously, since one direction has been selected. According to the *Goldstone theorem* [13] any spontaneous breaking of a continuous symmetry entails the appearance of a massless boson, viz. the *Goldstone boson*. For each broken symmetry generator one Goldstone boson appears. In the case of the Higgs mechanism three Goldstone bosons appear. They correspond to the fluctuations in the direction of the symmetry which are tangential fluctuations for the Higgs potential. The radial fluctuations correspond to a massive boson, viz. the *Higgs boson*, with the mass $m_{\text{Higgs}} = \sqrt{2}\mu$. Since μ is an unknown parameter, the mass of the Higgs can not be predicted. The three massless Goldstone bosons can be hidden by applying a gauge transformation. They then appear as longitudinal polarization of the $W^{\pm}$ and Z bosons, making them massive.

The Higgs mechanism is an elegant way to explain the massive gauge bosons. Mass is not a basic property of a particle, but particles obtain their mass by interacting with the massive scalar higgs field. The Higgs boson is the only not yet discovered particle of the Standard Model.

2.4 Challenges to the Standard Model

The Standard Model still leaves a couple of open questions. First of all it ignores one fundamental interaction, gravitation. There is no convincing way to explain gravitation in terms of particle physics. At energy scales of the experiments verifying the Standard Model, gravitation can be neglected. Nevertheless a satisfying theory must include and explain all known interactions. The mathematical issue is the incompatibility of quantum field theories like the Standard Model and general relativity, the best model to describe gravitation.

Why the strengths of the fundamental forces differ so much is another not understood part of the Standard Model, called the hierarchy problem. The mass of the higgs boson would diverge, by the contribution of loop corrections, unless a fine-tuning over many scales would cancel the radiative corrections and the mass.

It is not understood, why there are three generations of each particle of matter with only the first generation being stable. From Z^0 production measurements it is known, that the number of generations is limited to three, but why is still an unanswered question.

Together with many other unanswered questions, like *why does the electron charge equal the proton charge* or *why is there more matter than antimatter?*, there is plenty of room for the physics of the future.

2.5 Beyond the Standard Model

Apparently, the Standard Model is not the last word in particle physics. It is still necessary to add new features to answer the open questions. These extended models should not contradict the proven features, but predict new features and explain the yet unanswered questions. The extended theories should merge into the Standard Model. Several approaches try to extend the Standard Model. One of the most promising extensions to the Standard Model is the concept of *supersymmetry*, often abbreviated as *SUSY*. According to this theory, for each particle there exists a supersymmetric partner, the *sparticle*. Particle and sparticle differ by half a unit of spin. For every fermion there exists one sfermion with an integer spin. For each gauge boson a gaugino with half-integer spin. This would solve the hierarchy problem, since the sparticles would cancel the contributions of the particles to the radiative corrections. Since no sparticle has been discovered yet the masses of the sparticles have to be greater than 100 GeV.

3 The CMS Experiment at the LHC

At the CERN Laboratories in Geneva, Switzerland a new series of experiments have been designed with the main objective to test the Higgs model of spontaneous symmetry breaking and to advance into an energy range exceeding the current limits to discover potentially new physics and prove or disprove the Standard Model of Particle Physics and theories beyond.

3.1 The Large Hadron Collider

The heart of these experiments is the *Large Hadron Collider* (LHC), a nearly 27 km long storage ring, residing approximately 100 m beneath the surface between the Jura Mountains and Lake Geneva, crossing the border between France and Switzerland. It accelerates protons up to an energy of 7 TeV in two proton beams circulating in opposite directions inside the ring. At four interaction points protons from the two beams are brought to collision, with a center of mass energy of $\sqrt{s} = 14\,\text{TeV}$, an energy never achieved by any man made particle accelerator before. The protons in the beams are packed into bunches, with each bunch containing about 10^{11} protons. The time spacing between two bunches is about 25 ns, resulting in an event rate of 40 MHz. The revolution frequency is 11.246 kHz. A sketch of the LHC can be seen in figure 3.1. A high luminosity is necessary to find rare particles. The LHC design luminosity is $\mathcal{L} = 10^{34}\,\text{cm}^{-2}\text{s}^{-1}$. A number of 1232 dipole magnets keep the beam on the track. These superconducting magnets reach a magnetic dipole field of 8.33 T and are cooled by liquid helium.

The accelerator is located in the tunnel of the former electron-positron accelerator *Large Electron Positron collider* (LEP). The decision to accelerate protons instead of electrons was made because such high collision energies can only be obtained if synchrotron radiation losses are small. The proton mass is approximately 1836 times greater than the electron mass. Since the energy loss is proportional to $\propto m^{-4}$, protons of the same energy emit considerably less synchrotron radiation and are therefore the adequate choice. The price to pay for using protons instead of electrons is that protons are multi parton particles, containing quarks and gluons which share the nominal value of the center of mass energy and generate much higher background than point-like electron-positron collisions.

The accelerator is also capable to run with heavy ions, obtaining a collision energy of up to 1150 TeV, with an energy of about 2.76 TeV per nucleon.

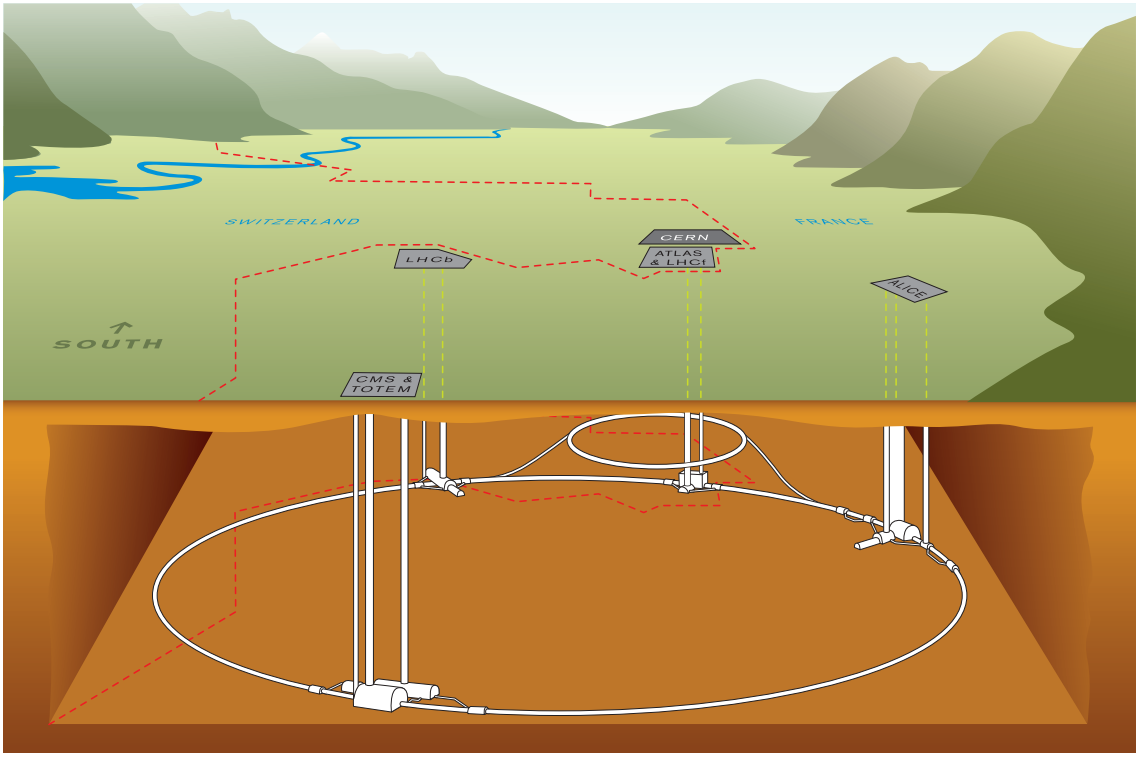

Figure 3.1: *The Large Hadron Collider with the four experiments CMS, ATLAS, LHCb and ALICE. [14]*

Two general purpose detectors, *A Toroidal LHC Apparatus* (ATLAS), and the *Compact Muon Solenoid* (CMS) detect particles generated in the collisions with the aim to explore the physics at the TeV scale, to discover the Higgs boson or neglect its existence and measure the properties of known particles with a higher precision than before as well as to search for evidence of physics beyond the standard model. The *Large Hadron Collider beauty* (LHCb) experiment is specialized for the precise measurement of the CP violation and rare decays. And *A Large Ion Collider Experiment* (ALICE) explores the strong interaction at very high energy densities in collisions with heavy ions. A new phase of matter, the quark-gluon plasma, is expected to exist in such environment.

3.2 The Compact Muon Solenoid

The Compact Muon Solenoid (CMS) is one of the two big multi-purpose detectors at the LHC. Being a collider detector, it is built in an onion-like structure, where specialized subdetectors are built up concentrically around the interaction point, in an order according to the energy loss of the particle to be detected. A liquid helium cooled solenoid magnet provides a magnetic field with a strength up to 4 T, to bend the tracks of charged particles for the determination of their momentum. The detector is optimized to detect a standard model higgs boson with a mass

range between $114\,\text{GeV} < m_H < 1\,\text{TeV}$. But CMS is also appropriate to search for supersymmetric particles or other yet unknown particles with electrons, muons and photons in the final state. Even heavy ion collisions can be surveyed with this detector.

CMS has a mass of 12 500 t, a length of 21.5 m and a diameter of 15 m . It has been assembled on the surface at ground level. Subsequently, the completed detector has been lowered into the cavern in large modules (up to 2000 t) and installed in its final position around the LHC interaction point, approximately 100 m under ground level. The lowering has been completed in early 2008. A sketch of the CMS detector can be seen in figure 3.2 an exploded view shows figure 3.15, whereas figure 3.14 shows the complete path for different particles in CMS.

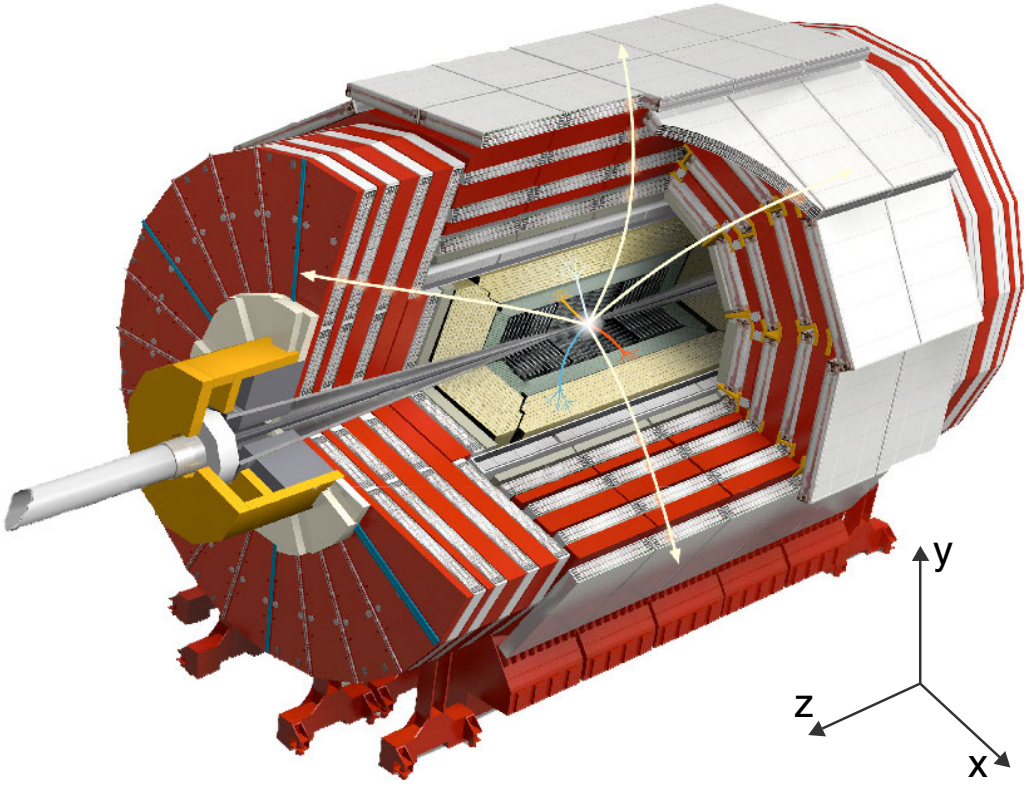

Figure 3.2: *The Compact Muon Solenoid. The interaction point in the center is surrounded onion-like by the subdetectors. Image based on [15]*

3.3 Coordinate Systems in CMS

The CMS detector has a cylindrical symmetry. The origin of the CMS coordinate system is the nominal interaction point in the center of the detector. The y axis is pointing vertically upward, the x axis points radially towards the center of the LHC ring, the z axis is tangential to the LHC ring.

The azimuthal angle ϕ is measured in the x-y plane starting at the x axis, the polar angle θ is measured from the z axis. The radial coordinate is measured in the x-y plane and the pseudorapidity is defined as $\eta = -\ln\tan\left(\frac{\theta}{2}\right)$

In general, the following regions of the detector are defined: The barrel region represents the cylinder surrounding the beam pipe, the endcap regions are the two planes closing the cylinder. The forward region is the high η area, close to the beampipe.

3.4 Tracking System

For the reconstruction of secondary vertices from particles with a lifetime of 10^{-12} s to 10^{-15} s, which fly a few mm before decaying, like B mesons or τ leptons, a very precise tracking is indispensable. The innermost subdetector, the *pixel detector*, fulfills this requirement. Enclosing the interaction point in a distance of a few centimeters, it measures the vertex position of charged particles in high resolution three-dimensional space points. An illustration of the pixel detector can be seen in figure 3.3. It consist of 66 million silicon pixels with a size of $100 \times 150\mu m^2$. Each silicon pixel acts like a diode in reverse bias condition. Charged particles passing a pixel create electron-hole pairs, the resulting flow of charges in the pixel can be read out. To obtain distinguishable track vertices, the granularity was chosen in a manner that the average occupancy is not more than 10^{-4} per pixel and per LHC bunch crossing. As the innermost subdetector the pixel detector is exposed to a very high particle flux of about $10^7\,\mathrm{cm}^{-2}\,\mathrm{s}^{-1}$ charged particles in a distance of 10 cm from the interaction point. Thus radiation hardness is very important. Nevertheless it is expected to have a limited lifetime and need to be replaced after approximately three years. The pixel detector is formed of three barrel layers of pixel modules with a length of 53 cm, mounted in distances of $r = 4.4$ cm, $r = 7.3$ cm and $r = 10.2$ cm from the interaction point. Two endcap disks on each side are installed in a distance of $|z| = 34.5$ cm and $|z| = 46.5$ cm covering a range of $|\eta| \leq 2.5$. The total surface of the pixel detector is $\approx 1\,\mathrm{m}^2$. The resolution is about 10 µm for the r-ϕ measurement and about 20 µm for the z measurement along the beamline.

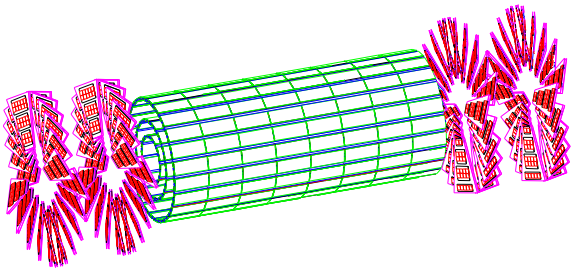

Figure 3.3: *View of the pixel detector.[16]*

In regions with a moderate particle flux and a longer lever arm the tracker uses silicon strips instead of silicon pixels for the detection of charged particles. The barrel part of the silicon strip detector is split into the *Tracker Inner Barrel* (TIB) and the *Tracker Outer Barrel* (TOB). A complete view of the tracker can be seen in

figure 3.4. The TIB covers the space from $r = 20\,\text{cm}$ up to $r = 55\,\text{cm}$ distance from the interaction point with a length from $z = -65\,\text{cm}$ to $z = 65\,\text{cm}$. It is equipped with 320 µm thick silicon strips. The surface of each silicon strip is growing with increasing distance r, the minimum strip size is $10\,\text{cm} \times 80\,\mu\text{m}$, resulting in an occupancy of 2-3% per bunch crossing. The silicon modules are arranged in four layers. The inner two of them are double sided *stereo modules* for a measurement in both, r-ϕ and r-z planes. For this reason, the orientation of the silicon sensors on the stereo modules to each other is rotated under an angle of 5.7°. The TIB reaches a resolution between 23 µm and 34 µm in r-ϕ and about 230 µm in z direction.

The TOB has a radius of about $r = 120\,\text{cm}$ and a length from $z = -110\,\text{cm}$ to $z = 100\,\text{cm}$. It is consist of six layers of sensors containing 500 µm thick silicon strips with a maximum surface of $25\,\text{cm} \times 180\,\mu\text{m}$ per strip. The two inner layers are built as stereo modules, also with a stereo angle of 5.7°. The TOB's resolution is between 35 µm and 52 µm in r-ϕ and about 530 µm in z direction.

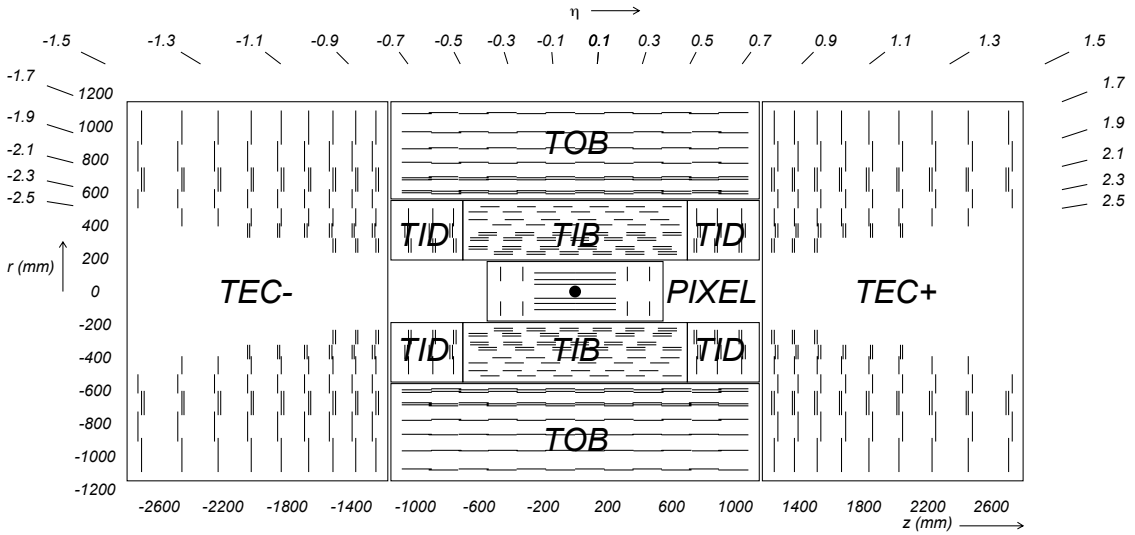

Figure 3.4: *View of the tracker with η range. Stereo modules are drawn with double lines, single modules with single lines. [17]*

The endcap region of the silicon strip detector is divided into the *Tracker End Caps* (TEC) and the *Tracker Inner Disks* (TID). The TID consists of three disks and the TEC of nine disks, equipped with rings of silicon strip modules. The first two rings carry stereo modules. The silicon strips are 320 µm thick, in the outer disks of the TEC 500 µm thick silicon strips have been used. The TEC covers the area from $|z| = 120\,\text{cm}$ to $|z| = 280\,\text{cm}$.

All in all 9.6 million silicon strips are read out in the four strip detector components, with a total surface of more than $200\,\text{m}^2$. An analog readout has been chosen to obtain the information about the deposited charge. Using a *center of gravity* method which accounts the charge of the neighboring strips into the reconstruction, a higher spatial resolution is gained. The tracking system was designed to have as

little material as possible, avoiding showering. It resides in a temperature controlled environment to reduce the radiation damage and will be operated at around $-10\,^{\circ}\mathrm{C}$ for the silicon strip detector and $-20\,^{\circ}\mathrm{C}$ for the pixel detector [18].

3.5 Calorimetry

The CMS calorimetric system measures the energy of the particles using two distinct subdetectors. The *Hadron Calorimeter* (HCAL) for the detection of hadronic particles, the *Electromagnetic Calorimeter* (ECAL) detects electrons and photons. For a precise determination of missing transverse energy E_T^{miss} the calorimetric system was designed hermetically.

Electromagnetic Calorimeter

The ECAL is a scintillating crystal detector for electrons, positrons and photons. It is divided into a barrel section (EB) and two endcaps (EE). An illustration of one quarter of the ECAL is shown in figure 3.6. More than 75 000 lead tungstate ($PbWO_4$) crystals form a hermetic and homogeneous calorimeter. Inside the crystals electrons and positrons emit bremsstrahlung and photons undergo pair production. The incoming particle starts a shower of low-energy particles which lose their energy until the whole shower is absorbed. This induces the crystals to emit scintillation light with a wavelength having a broad maximum at $\lambda = 420\,\mathrm{nm}$, which is blue-green. Photodetectors collect this light, allowing a precise determination of the deposited energy. Lead tungstate fulfills the high demands of the LHC environment with a fast response time of 25 ns for emitting 80% of the light, a compact shower (the radiation length is $\mathrm{X}_0 = 8.9\,\mathrm{mm}$ and the moliere radius 22 mm) and radiation hardness up to 10 Mrad.

The design of the electromagnetic calorimeter was driven by fulfilling the performance requirements for the detection of a Higgs boson with a mass below 140 GeV, decaying in two photons: $H \to \gamma\gamma$. A simulation of this signal can be seen in figure 3.5. The energy resolution of a calorimeter can be parameterized as follows

$$\frac{\sigma_E}{E} \approx \frac{S}{\sqrt{E}} \oplus \frac{N}{E} \oplus C \quad , \tag{3.1}$$

where S is the stochastic parameter, N the noise term and C an offset. The showering is a statistical process and therefore the energy resolution is better for higher energies. The parameters a, b, N are as small as possible, resulting in a good energy resolution and are adjusted in such a manner that they are in the same order of magnitude at photon energies similar to those from $H \to \gamma\gamma$ decays. Testbeam measurements performed in 2004 found (with E given in GeV)

$$\frac{\sigma_E}{E} \approx \frac{2.8\%}{\sqrt{E}} \oplus \frac{0.12}{E} \oplus 0.30\% \quad , \tag{3.2}$$

to provide a typical energy resolution [17]. For energies of 20 GeV the resulting resolution is $\sigma_E/E \approx 1\%$, for 200 GeV it is $\sigma_E/E \approx 0.4\%$ [16].

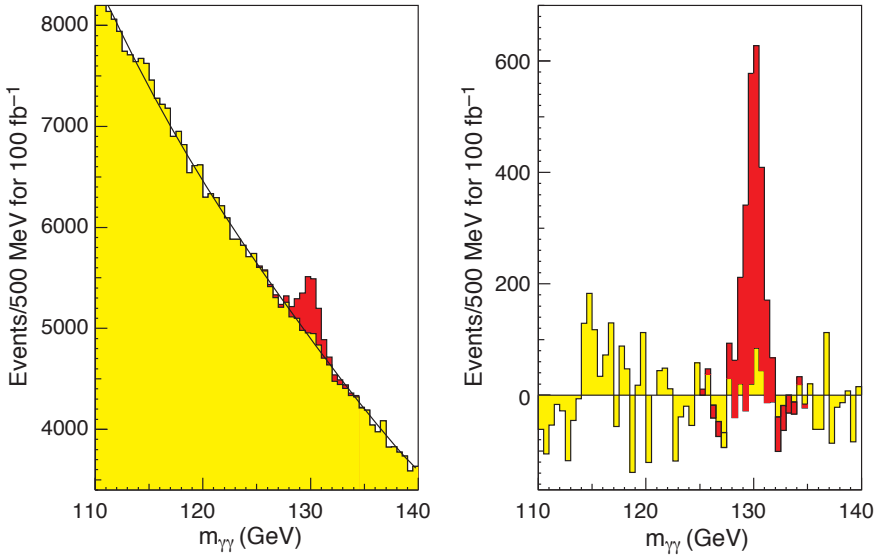

Figure 3.5: *Simulated signal of a $H \to \gamma\gamma$ decay. Shown is the invariant mass distribution of two photon events for 100 fb^{-1} data and an assumed Higgs mass of 130 GeV, the signal in red, the background in yellow. The left plot is with full background, on the right side the background has been subtracted.[19]*

The EB starts in a distance of $r = 129$ cm from the interaction point with a length from $z = -3.045$ m to $z = 3.045$ m, covering a pseudorapidity range of $|\eta| < 1.479$. It is built out of 36 *supermodules*, each carrying 1700 lead tungstate crystals. The crystals front side surface - with a size of about $22 \times 22\,\text{mm}^2$ - corresponds to the moliere radius and the length of 23 cm matches about 26 radiation lengths at $\eta = 0$ to avoid that the shower leaks out of the calorimeters back, since the longitudinal shower leaking limits the energy resolution. The crystals are mounted such that their front face is tilted by 3° with respect to the line connecting the crystals front face center with the interaction point. Additionally the crystals are tilted by 3° in ϕ to obtain a non-pointing geometry in η and ϕ. The photodetectors used in the EB to register the scintillation light are silicon avalanche photodiodes (APDs). Their signal is first pre-amplified and then digitized for the read-out. Due to their immunity to high magnetic fields they can be positioned close to the scintillating crystals inside CMS, without the need of long fiber optics, which degrade the time resolution.

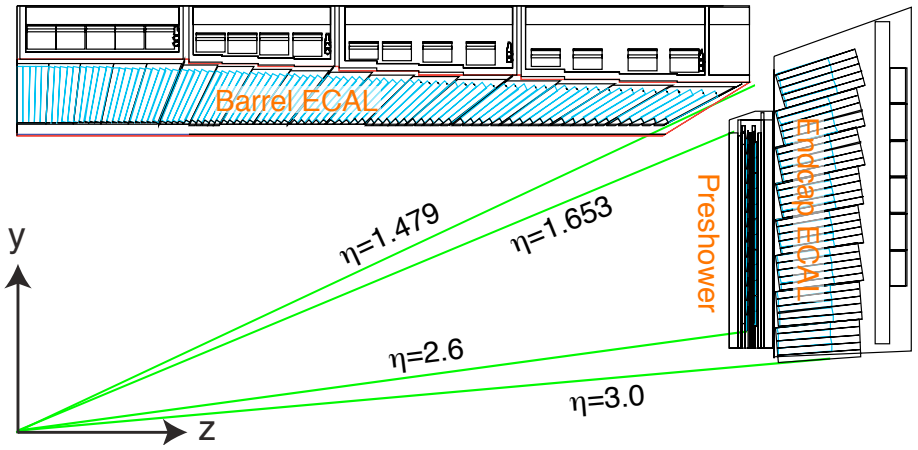

Figure 3.6: *One quadrant of the ECAL. The crystals are mounted such that their front face always directs to the interaction point, but tilted by 3°. [16]*

The endcaps are placed at $|z| = 3.14\,\text{m}$ corresponding to $1.479 < |\eta| < 3$. Each EE is built of two semi-circle shaped *Dees* equipped with 3662 crystals, structured in 156 *supercrystals*. The endcap crystals have a front surface of $28.6 \times 28.6\,\text{mm}^2$ and a length of 22.0 cm. In the endcaps the scintillation light is registered using vacuum phototriodes (VPTs).

The amount of scintillation light varies with the temperature by nearly 2% per °C at room temperature. On that account, the temperature environment in the electromagnetic calorimeter is strictly regulated with a cooling system extracting the heat of the electronics and keeping the crystal temperature stable within ±0.05 °C.

Before the endcaps, in the forward region of $1.65 < |\eta| < 2.6$, the CMS preshower detector (ES) is installed. The ES is a sampling calorimeter, with silicon strip sensors, intended for the γ-π^0 separation. By determining the position of the impact of the electromagnetic shower with fine granularity, the preshower detector can separate single showers from overlaps of two showers due to a π^0 decay. It is built up of more than 4300 modules with a size of $6.3 \times 6.3\,\text{cm}^2$, each containing 32 silicon strips, 300µm thick, with a pitch of 1.9 mm, covering a total surface of approximately $16\,\text{m}^2$. The preshower detector consists of two planes of silicon strip detectors, each behind a lead absorber for the activation of a shower, with a thickness of one, respectively two radiation lengths. [19]

Hadronic Calorimeter

The HCAL is a sampling calorimeter for the detection of hadronic particles and jets and the measurement of their energy. Due to the hermetic construction the HCAL also allows the determination of missing transverse energy E_T^{miss} for the indirect detection of neutrinos or potentially existing neutral supersymmetric particles. The HCAL is built out of four components: The *Hadron Barrel* (HB), the *Hadron Endcap*

(HE), the *Hadron Forward* (HF) and the *Hadron Outer* (HO), also referred to as *tail catcher* (TC).

The HB and HE are made of layers of brass plates, parallel to the beam axis, acting as absorber material followed by 3.77 mm thick tiles of scintillator plates with a granularity of $\Delta\eta \times \Delta\phi = 0.087 \times 0.087$. Each tile is connected with a wavelength shifting fiber, which is spliced to a clear fiber at the end of the tile. The read out is done by multi-channel hybrid photodiodes, mounted in optical decoding units. Brass as absorber material has the advantage of a sufficient short interaction length and being non-magnetic [20].

The HB is divided into two half-length barrels residing inside the magnet coil. Each half barrel is formed of 18 identical wedges, 20° wide in ϕ, with 17 layers of scintillator, divided in 16 sectors (η towers) in η direction. The radial extension is of $r = 177\,\text{cm}$ to $r = 295\,\text{cm}$, covering the pseudorapidity range $|\eta| < 1.3$ [16]. The inner and the outer absorber layer is made of stainless steel, followed by a 9 mm thick scintillator. The total depth of the HB is 5.82 interaction lengths at $\eta = 0$ and increases up to 10.6 interaction lengths at $|\eta| = 1.3$ [17].

The two HE endcaps are completing the HB inside the magnet coil. They are built in a 18 fold geometry, matching the wedges of the barrel. The HE spans a pseudorapidity range between $1.3 < |\eta| < 3$. Above $\eta > 1.74$ the granularity increases from $\Delta\eta \times \Delta\phi = 0.087 \times 0.087$ to $\Delta\eta \times \Delta\phi \approx 0.17 \times 0.17$. 19 layers of scintillator register the showering of hadronic particles. The design was optimized to minimize cracks between the single parts of the hadronic calorimeter to tighten the construction for a hermetic calorimetry.

Since the radial extension and therefore the total amount of material of the HB is limited by the magnet and the electromagnetic calorimeter, an additionally tail catcher, the HO, is placed outside of the magnet, covering the pseudorapidity range of $|\eta| < 1.26$. Made up of scintillator layers, ordered in five rings with twelve sectors of 30° in ϕ, the HO is matching the geometry of the muon system. An 18 cm thick iron plate is followed by a 10 mm thick scintillator placed at $r = 4097\,\text{mm}$ distance from the interaction point. The central ring has an additional layer of scintillator placed before the iron plate at $r = 3850\,\text{mm}$. The magnet coil acts as additional absorber for the HO. In the same manner as in the HB and HE, the scintillation light is collected by wavelength shifting fibers, spliced to clear fibers and read out with photodetectors located around 10 m away.

Two forward calorimeters HF are placed in a distance of $z = \pm 11.2\,\text{m}$ from the interaction point, detecting forward jets and improving the missing transverse energy measurement by providing a better hermeticity. Since the HF is exposed to very high particle fluxes the design was driven by constructing a radiation hard calorimeter. For this scope the HF is designed as a cherenkov detector using quartz fibers as active material embedded in steel absorber. The HF is sectioned in 18 wedges with a depth of 165 cm. The quartz fibers pass parallel to the beam line, two different types of fibers are altering in a distance of 5 mm: Full length fibers, running through

the complete absorber and shorter fibers starting in a depth of 22 cm. Both types of fiber are readout separately. The cherenkov threshold for electrons is $E \geq 190\,\text{keV}$ and therefore the HF is most sensitive to the electromagnetic part of showers. The material of the HF correspondes to about 10 interaction lengths [17].

In the very very forward region two additional calorimeters are placed, intended for the detection of debris from heavy ion collisions and for *forward physics* from proton proton collisions. The *Centauro And Strange Object Research* (CASTOR) is a quartz tungsten sampling calorimeter at $|z| = 14.38\,\text{m}$ from the interaction point. CASTOR is a cherenkov detector similar to the HF covering the pseudorapidity range from $5.2 < |\eta| < 6.6$. In a distance of $|z| \approx 140\,\text{m}$ from the interaction point the *Zero Degree Calorimeter* ZDC is located. It measures neutrons and very forward photons in two subdetectors, the electromagnetic (EM) and the hadronic (HAD) section, both working as sampling calorimeter.

3.6 The Solenoid

For a precise measurement of the momentum from charged particles a strong magnetic field is crucial. The CMS magnet is a superconducting solenoid, providing a central magnetic induction of 4 T. Yet it will be operated at a nominal field strength of 3.8 T. A schematic view of the solenoid can be seen in figure 3.7. The cylinder shaped magnet resides on the outer side of the HB, as visible in figure 3.15. The free inner bore has a diameter of 6 m and a length of 12.5 m. Four layers of NbTi windings, cooled with liquid helium form the solenoid coil. The total amount of energy stored in the magnetic field is up to 2.6 GJ. The magnet is surrounded by a return yoke made of 10 000 t of iron. Due to the solenoid coil and the superconducting windings, the magnet is - compared to its strength - moderately sized. Nevertheless it is the worlds largest superconducting solenoid.

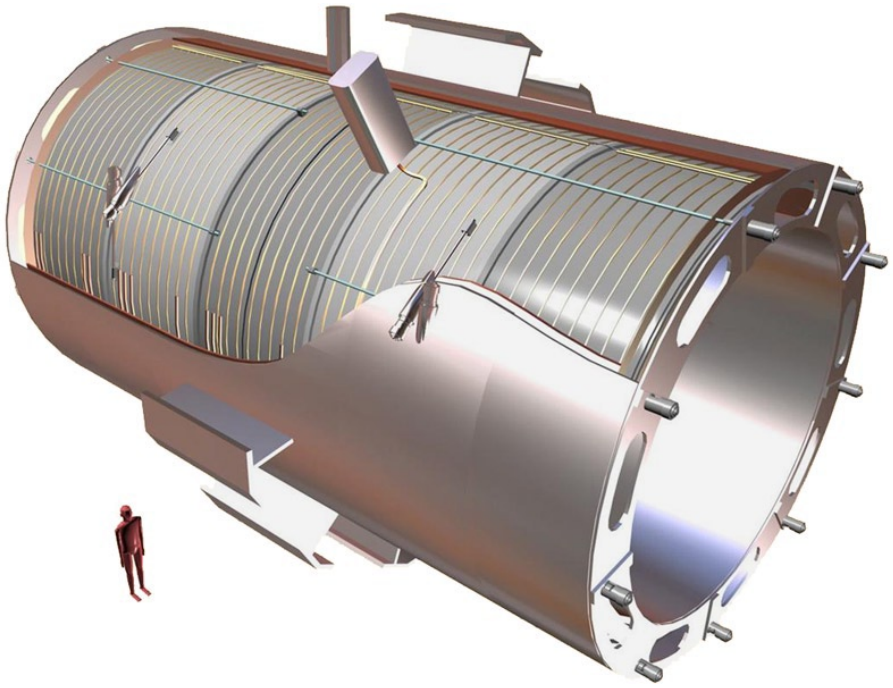

Figure 3.7: *View of the solenoid magnet. [17]*

3.7 Muon System

Muons provide a crucial signature for many decays. For example a promising predicted decay mode for the higgs boson is $H \rightarrow ZZ^{(*)} \rightarrow \mu^+\mu^+\mu^-\mu^-$, which provides a clear signal and thus has been referred to as the "Golden Channel". But also various supersymmetric particle decays are predicted to have muons in their final state. Consequently, CMS has a highly efficient and accurate muon system, representing the "M" of CMS [1], which fulfill three main tasks: Identifying muons, measuring the muon momentum and charge as well as providing a trigger signal. The CMS muon system consists of three subdetectors: *drift tubes* (DT) in the barrel region, *cathode strip chambers* (CSC) in the endcap regions and *resistive plate chambers* (RPC) in the barrel and the endcap regions for a fast bunch crossing identification. A sketch of the muon system is shown in figure 3.8. The design of the muon system was driven by obtaining a good momentum resolution and charge identification over the whole kinematic range with a reliable, robust and relatively inexpensive detector. The momentum resolution of the muon system is about

$$\frac{\Delta p_T}{p_T} = 0.1 \tag{3.3}$$

for 100 GeV muons with $\eta < 0.8$, strongly depending on the muon momentum and the pseudorapidity [17]. Figure 3.11 shows the momentum resolution for different momenta and η ranges for the muon system, the tracker and both combined.

[1] CMS = Compact **Muon** Solenoid

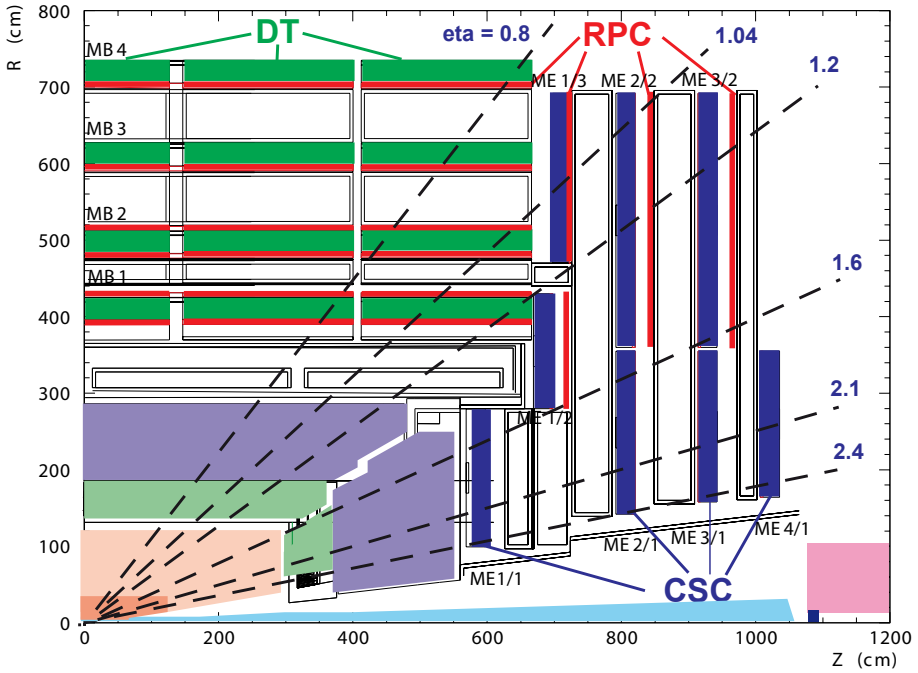

Figure 3.8: *One quarter of the CMS muon system. In the barrel part four stations of DT chambers (green) can be seen, along with RPCs (red), covering up to $\eta = 1.2$. The endcaps are equipped with RPCs up to $\eta = 1.6$ and CSCs (blue) up to $\eta = 2.4$. [16]*

Drift Tube Chambers

The drift tube muon system reside in the magnet's return yoke in the barrel of CMS. The *yoke barrel* (YB) is a cylinder, split into five wheels, numbered from YB-2 for the outer wheel in $-z$ direction to YB+2 for the outer wheel in $+z$ direction. Each wheel contains four stations, forming concentric cylinders around the beam line, called MB1 at $r \approx 4.0\,\text{m}$, MB2 at $r \approx 4.9\,\text{m}$, MB3 at $r \approx 5.9\,\text{m}$ and MB4 for the outermost station at $r \approx 7.0\,\text{m}$. Each station is divided into 12 azimuthal sectors covering 30° in ϕ, labeled in the order of increasing ϕ, starting with sector S1 at $\phi = 0$. Finally each sector contains one muon chamber. In the MB4 station the top and the bottom sector is equipped with two chambers to cover the complete extend. The chambers in sector S3 and sector S4 in the wheels YB+1 and YB-1 are called chimney chambers. They are 40 cm shorter in z direction, to leave a gap for the magnet's cryogenic lines. All in all 250 drift tube chambers are mounted in the yoke barrel wheels. A traversal view on one wheel showing its muon chambers is given in figure 3.9. Among the stations the chambers are staggered to shift the position of the gap between the sectors. A high p_T muon in the vicinity of the sector borderline should pass at least three chambers. The drift tubes chambers cover a pseudorapidity range of $|\eta| < 1.2$ The drift tube chambers are described in detail in section 4.2.1. During the commissioning phase the sectors S1 and S7 were not

equipped, since at these positions the crane should carry the wheels for lowering them in the underground cavern.

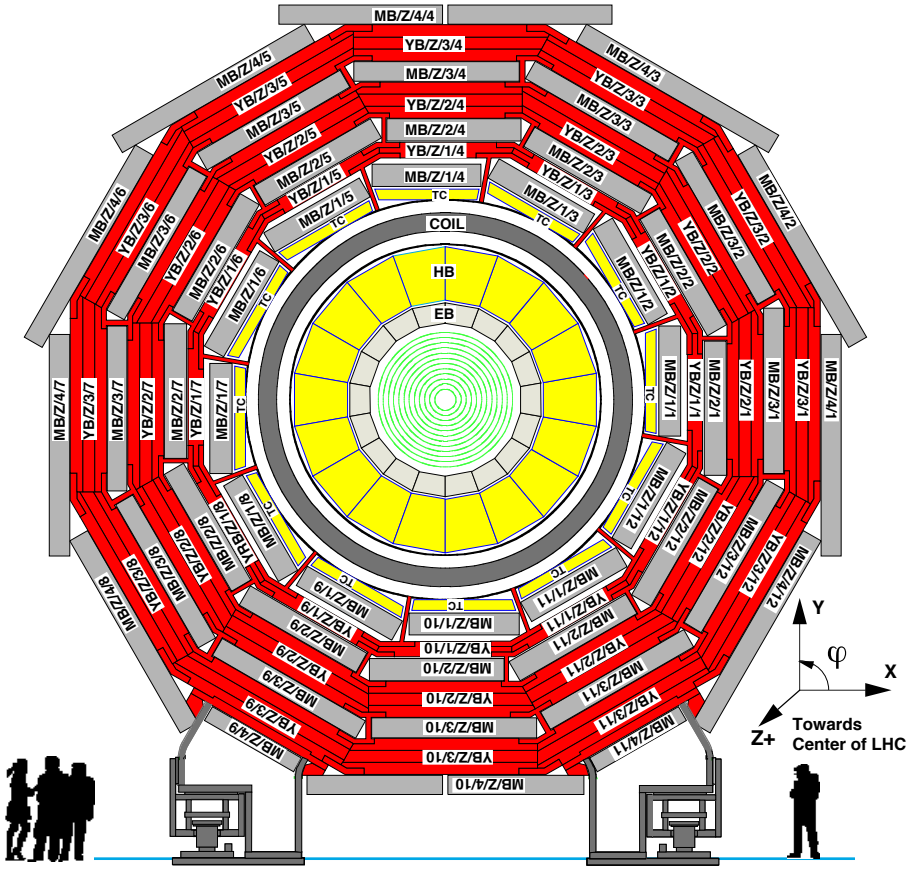

Figure 3.9: *Traversal view of one wheel of CMS. The muon chambers (marked in grey) are mounted in-between the iron of the return yoke (marked in red). Labeling: Name/Wheel/Station/Sector. [21]*

Cathode Strip Chambers

The CSCs are multi-wire proportional chambers in the endcap region of the muon system. They consist of six layers of 9.5 mm wide, gas filled gaps with planes of radial cathode strips, 8.4 mm to 16 mm wide and perpendicular anode wires with a spacing between 2.5 mm and 3.2 mm. The gas is a mixture of 40%Ar, 50%CO_2 as quenching gas and 10%CF_4 to prevent polymerization on the wires [17]. Muons traversing the gaps ionize the gas; the electric field between the cathode and the anode accelerate the ions to the cathode and the electrons to the anode, where they start an avalanche (4.1). Both, wires and strips are readout simultaneously and since they are perpendicular each layer can measure a three dimensional space coordinate (r, ϕ, z).

As shown in figure 3.8, four stations, called ME1 to ME4 are equipped with rings of trapezoidal CSC modules. The inner ring (MEz/1) of each station (MEz) consists

of 18 modules, each covering 20° in ϕ, the outer rings are formed of 36 modules, each covering 10° in ϕ. Due to the strong magnetic field, the ME1/1 modules have a slightly different geometry with thinner gas gaps and a changed pitch. The wires in these modules are tilted, to compensate the Lorentz angle. Altogether 468 modules are arranged in an overlapping geometry in ϕ (except ME1/3) to hermetically cover a pseudorapidity range of $0.9 < |\eta| < 2.4$ [17, 22].

Resistive Plate Chambers

To provide a very fast response, the muon system is additionally equipped with resistive plate chambers. The drift-time in the DT chambers can be up to 380 ns, but the bunch crossing (BX) distance is 25 ns. With their very good time resolution of $\sigma_t < 1.3\,\text{ns}$ [23] the RPC can unambiguously assign the correct bunch crossing (BX) to a muon track, even in a high particle rate environment.[2] The RPCs are gaseous parallel-plate detectors made of two gaps, 2 mm wide, filled with a gas mixture of 96.2% $C_2H_2F_4$, 3.5% iC_4H_{10} and 0.3% SF_6 admixtured with water vapor to reach a humidity of 45% [17]. Each gap is surrounded by highly resistive (more than $10^{10}\,\Omega \cdot \text{cm}$) bakelite plates. The inner side of the bakelite is treated with linseed oil, the outer surface is coated with graphite electrodes. In-between these two bakelite surrounded gaps are - separated from the graphite coat by a thin isolating PET layer - aluminum strips for the readout. A sketch of the RPCs can be seen in figure 3.10. To deal with high rates of particle flux, the chambers are operated in avalanche mode. A muon traversing the gap ionize the gas, due to the electric field an avalanche (4.1) is started. Before the electrons reach the graphite, a charge is induced in the aluminum strips, which is read out. The induced charge in a strip is the sum of two single gap signals. This leads to a higher efficiency than in single gap chambers.

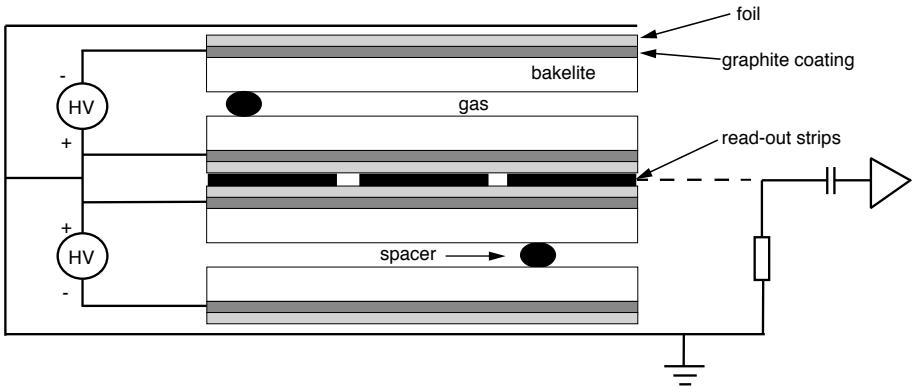

Figure 3.10: *Sketch of a RPC. [16]*

[2] Nevertheless, the DT chambers have their own bunch crossing identification. See section 4.3

In the barrel region, a total of 480 chambers with $2400m^2$ active surface are installed in six concentric cylinders. Two RPCs sandwich each of the inner DT stations MB1 and MB2. The two outer DT stations MB3 and MB4, are each accompanied by one adjacent RPC on the inner side of the DT chamber. In the endcap region, three stations of RPC chambers are installed The stations consist of three rings of trapezoidal modules, each module covering 10° in ϕ, apart from the inner ring in RB2 and RB3, which is built with modules covering 20° in ϕ. The modules overlap to avoid dead regions. The RPC covers a pseudorapidity of $\eta < 2.1$. In the startup phase of LHC the RB stations will not be instrumented completely and hence the covered pseudorapidity range is then $\eta < 1.6$.

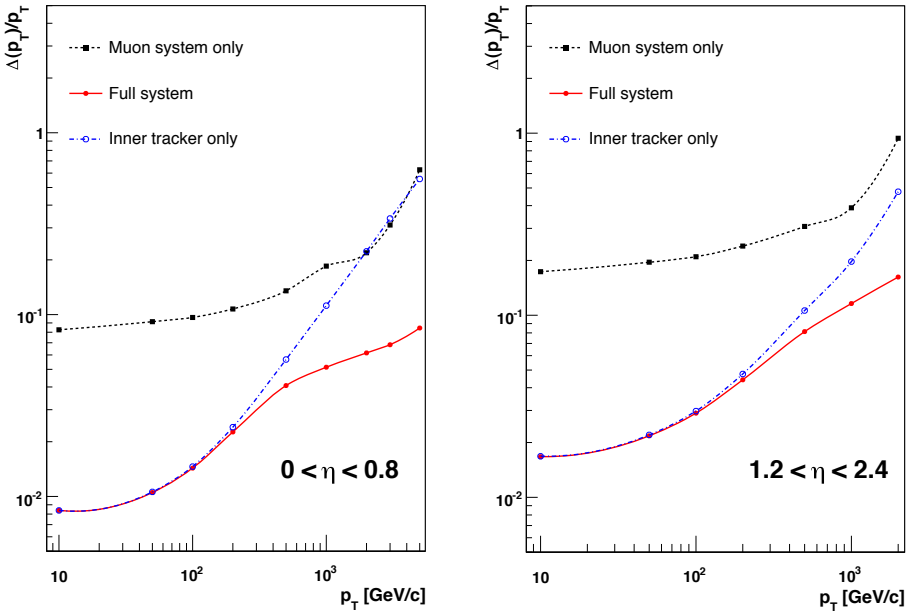

Figure 3.11: *Muon transverse momentum resolution as a function of the transverse momentum for different pseudorapidity ranges. The black marks indicate the resolution of the muon system only, the blue marks indicate the inner tracker's resolution. The combined resolution is drawn in red. [17]*

3.8 Trigger and Data Acquisition

At the LHC design luminosity of $\mathcal{L} = 10^{34}\,\mathrm{cm}^{-2}\mathrm{s}^{-1}$, about 20 pp collisions per bunch crossing of 25 ns are expected. To deal with the resulting huge amount of data with an event rate of nearly 1 GHz, it is inevitable to reduce the event rate. Therefore, CMS contains a sophisticated trigger system, which is also the begin of the physics event selection. The trigger consists of two levels: the *Level-1 trigger* (L1) and the *High-Level trigger* (HLT). The L1 trigger is implemented as hardware with custom designed electronics. It considers information from the calorimetry and the muon systems, as well as correlations between both systems. Events from the tracker and pre-shower not considered, since their amount of data is too much. All information

about an event is stored in a 3.2 µs long pipeline. In this time the trigger has to make the decision if an event is accepted or refused. Every 25 ns the trigger has to make a new decision to process the data from each bunch crossing. The accepted data are moved to a buffer for readout. The L1 trigger identifies objects such as photons, electrons, muons, jets and missing transverse energy. These objects are tested against p_T and E_T thresholds. A pattern recognition decides on the basis of the global combination of these objects whether to accept the event or not. The design rate of events accepted by the Level-1 trigger is about 100 kHz. In normal operation it will be around 30 kHz, providing a safety factor of three [17]. At design luminosity this corresponds to a rejection rate of 10^4.

Level-1 Trigger

The L1 trigger is made up several components, as seen in figure 3.12. The first one is the local component, based on track segments and hit patterns with bunch crossing assignment in the muon chambers. The local trigger for the drift tube chambers is described in section 4.3. For the calorimeter the local level is called *Trigger Primitive Generator* and identifies so-called trigger primitives with bunch crossing assignments, energy sums and lateral extension for the HCAL and the ECAL, which are compared to a threshold. The regional component combines this information to candidates for objects like electrons or muons in a limited region. The quality of the trigger object is determined and ranked.

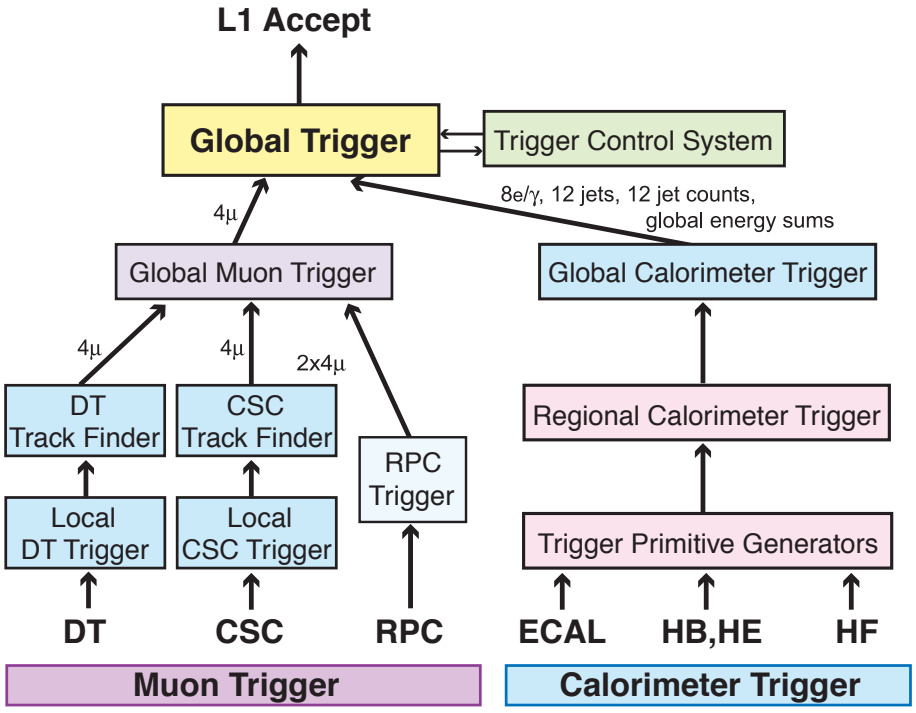

Figure 3.12: *The data flow in the Level-1 trigger. [17]*

The global muon component and the global calorimeter component chooses the best candidates of all regional ones, for the muon system respectively the calorimeters. Finally a global trigger decides whether to reject or accept the event.

The physics requirements for the L1 trigger are the following: over a pseudorapidity range of $|\eta| < 2.5$ the trigger should select leptons and jets above a selected transverse momentum threshold with a very high efficiency. For single leptons with a transverse momentum of $p_T > 40\,\text{GeV}$ and dileptons with $p_T > 20\,\text{GeV}$ for the first and $p_T > 15\,\text{GeV}$ for the second lepton full efficiency ($> 95\%$) is required in this pseudorapidity range. The single photon and diphoton triggers should have the same thresholds as the leptons. Over the whole pseudorapidity range of $|\eta| < 5$ jets and multijets are required to be triggered with a well-defined efficiency. For higher transverse momenta the jet trigger is required to be fully efficient.

The missing transverse energy trigger is required to have a threshold of about 100 GeV. With these requirements, a high efficiency for hard scattering physics is obtained, including signals such as top decays into electrons and muons, higgs decays into two photons or four leptons, W-W scattering, supersymmetry, $Z^{(*)}$ and top decays. [24]

Data Acquisition and High-Level Trigger

Due to the capacity and speed of mass storage systems, the output rate from the Level-1 trigger is still too high. Therefore, a second selection process is performed in the High-Level trigger. The HLT is implemented in software, running on a filter farm with commercial CPUs. Collecting data from all sources at the maximum L1 output rate of 100 kHz produces a data stream of about 100 GB/s. This is done by the *Data Acquisition* system (DAQ). The architecture of the DAQ is shown in figure 3.13.

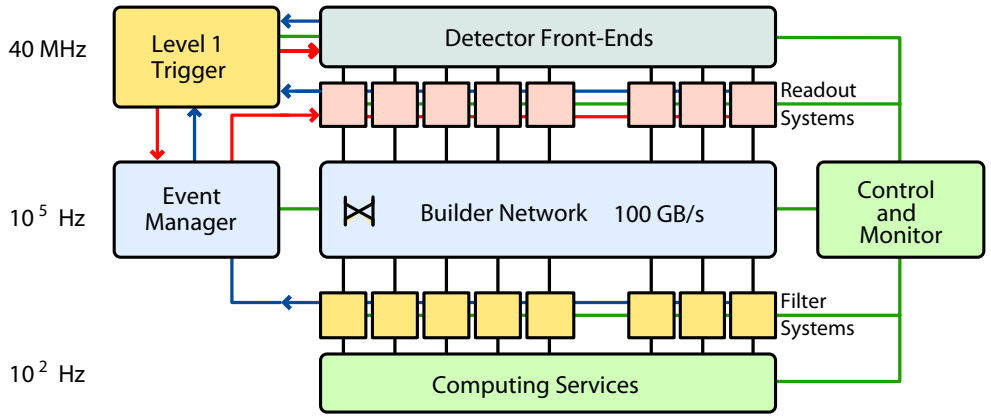

Figure 3.13: *The architecture of the DAQ system. [17]*

The data from events which passed the L1 trigger are readout from the subdetectors front-end electronics in parallel by multiple units and stored in buffers. A large switched network, the *Builder Network* connects these buffers with the HLT filter farm. The *Event Manager* controls the data flow through the DAQ [25]. The DAQ does also operate the *Detector Control System*, which supervises environmental parameters such as pressure, electrical power supply, cooling, gas flow, etc. and therefore ensures the correct operation of CMS.

The HLT software runs on a farm of about 2500 worker nodes. On a farm of processors, one event is analyzed by one processor, instead of a massive parallel use of processors where all processors analyze one event. The advantage of a farm is a much easier data handling and programming, for the price of a higher latency, which requires large buffers. The design of the HLT is capable of scaling with the state of the art technology, since processor and network technology evolve very fast. Also the algorithms of the HLT software will evolve with time and experience.

The HLT can consider the complete read-out data and performs complex calculation, similar to those made in the offline analysis software. Physics selection algorithms are applied to the data to identify the events with the most interesting physics content. The HLT provides a clean particle signature, effective mass cuts and event topology, track reconstruction, event reconstruction and data analysis. It is required to tag all events as candidates for specific physics processes.

The event rate reduction factor by the HLT is about 1000, resulting in an output rate of about 100 Hz. This data is stored for archiving and later offline analysis.

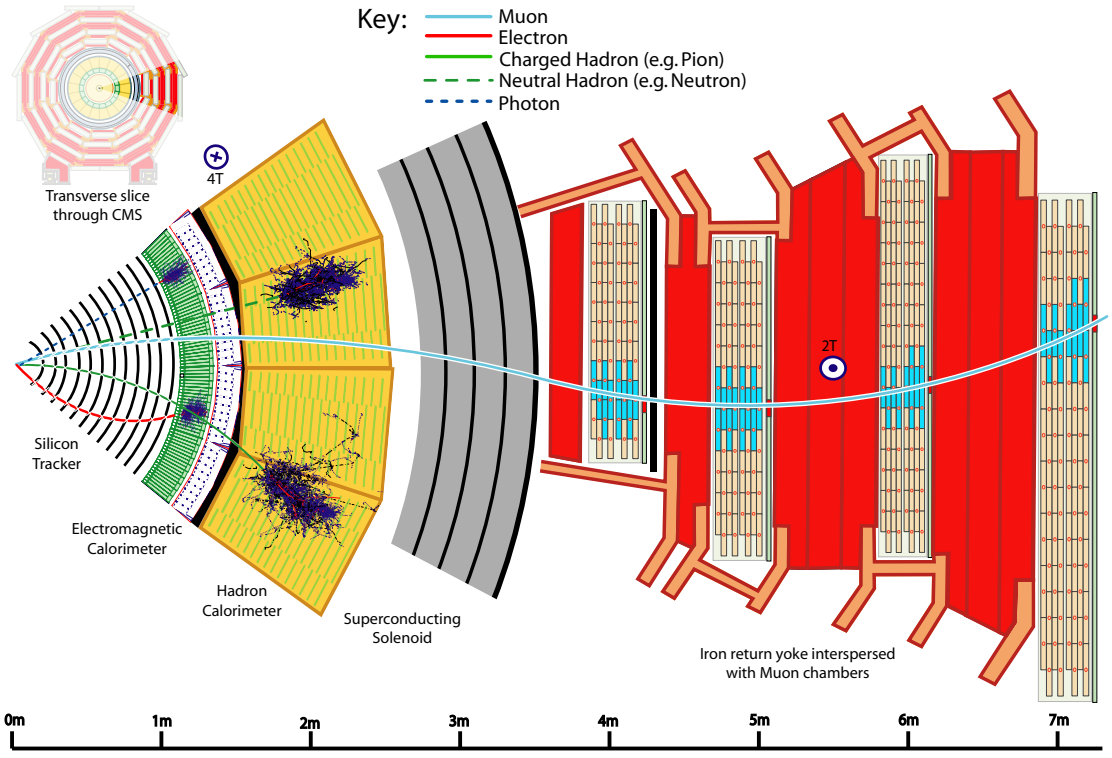

Figure 3.14: *Slice through CMS showing the particles incident on the different sub-detectors. In this picture the complete path of different particles in the CMS detector is shown. Electrons and Hadrons shower in the electromagnetic calorimeter. Hadrons are stopped in the hadronic calorimeter. Only muons can traverse the material of the calorimeter, the magnet and the yoke, providing a signal in the muon chambers. The trajectory of charged particles is bended due to the magnetic field, allowing the determination of their momentum. [21]*

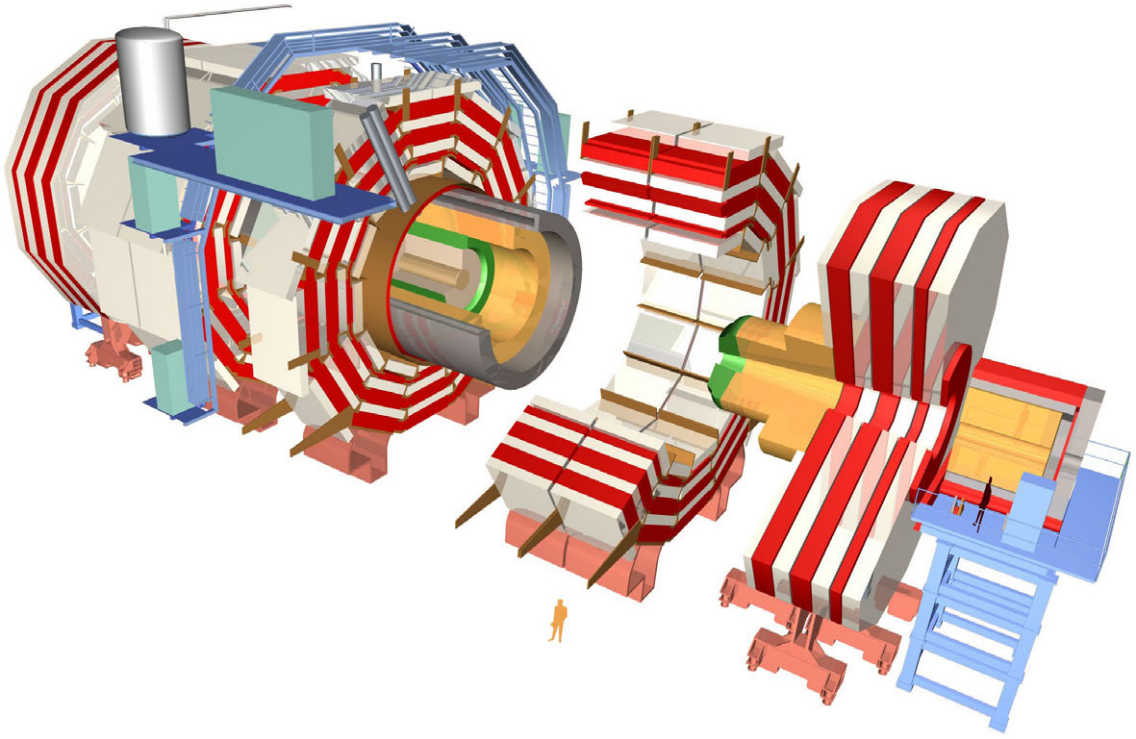

Figure 3.15: *Exploded view of CMS. [21]*

4 The CMS Drift Tube Chambers

4.1 Basic Principle

The mechanism underlying various types of gaseous detectors is the flow of charged particles in a gas after particles of ionizing radiation pass the detector. All these detector types have a common structure: Inside a gas filled enclosure is an anode on a high electric potential. Particles crossing the detector ionize the gas, the electric field accelerates the ionization electrons to the anode as well as the ions to the cathode. The movement of the electrons can be measured as an electric pulse. The accelerated electrons can ionize other gas molecules (respectively atoms) which then are also accelerated, an avalanche starts, increasing the charge drifting toward the anode wire.

Passage of particles through matter

When traversing matter, a charged particle interacts with it. Among all possible interactions, the dominant one is the electromagnetic. All types of detectors are based on electromagnetic interaction of primary or secondary particles with the detector material. In gaseous detectors the direct interactions between the electromagnetic field of the incoming charged particle and the electron sheath of the gas atoms is the primarily used mechanism for detection. Electrons are set free in ionization and accelerated towards the anode, where they can be detected. Some gaseous detectors register the photons emitted when an excited molecule returns to the ground state. Processes like bremsstrahlung or transition radiation are negligible for particle detection [26]. The interaction of particles in matter is a statistical process and underlies fluctuations, especially for thin materials, since the deposition of energy consists of many single scattering processes, each with a variable energy transfer. For a particle with a given momentum, the probability distribution of the energy loss can be approximated by a Landau distribution. If the energy transfer in a single scattering process is high enough ($> 1\,\mathrm{keV}$), the ionization electron can ionize other gas molecules by itself. These electrons are referred to as δ-rays.

The mean energy loss per path due to ionization and excitation is described by the *Bethe-Bloch formula* [7]:

$$-\left(\frac{dE}{dx}\right)_{\text{e,ion.}} \approx \frac{4\pi N_A \alpha^2}{m_e} \cdot \frac{Z}{A} \cdot \rho \cdot \frac{1}{\beta^2} \cdot \left(C + \ln \beta^2\gamma^2\right) \ . \tag{4.1}$$

$N_A = 6.022 \cdot 10^{23}\text{mol}^{-1}$	Avogadro constant
ρ	Density
$\alpha = \frac{e^2}{4\pi\epsilon_0\hbar c} \approx \frac{1}{137}$	Sommerfeld fine-structure constant
$m_e =$	Electron mass
Z	Atomic number
A	Atomic mass number
$\beta = \frac{v}{c}$	Velocity of the incoming particle in units of the speed of light
$\gamma = \frac{1}{\sqrt{1-\beta^2}}$	Lorentz factor
$C \approx 8$	Constant, weakly depending on the material

This equation is valid for particles with a charge of $\pm e$ and velocities of $\beta > Z \cdot \alpha$. For particles with the same velocity β, the energy loss is independent of the mass (if $m \gg m_e$) and independent of the type of particle. It depends only on the speed β of the incoming particle, since $\frac{Z}{A} \approx \frac{1}{2}$ the energy loss per density is almost independent of the traversed material.

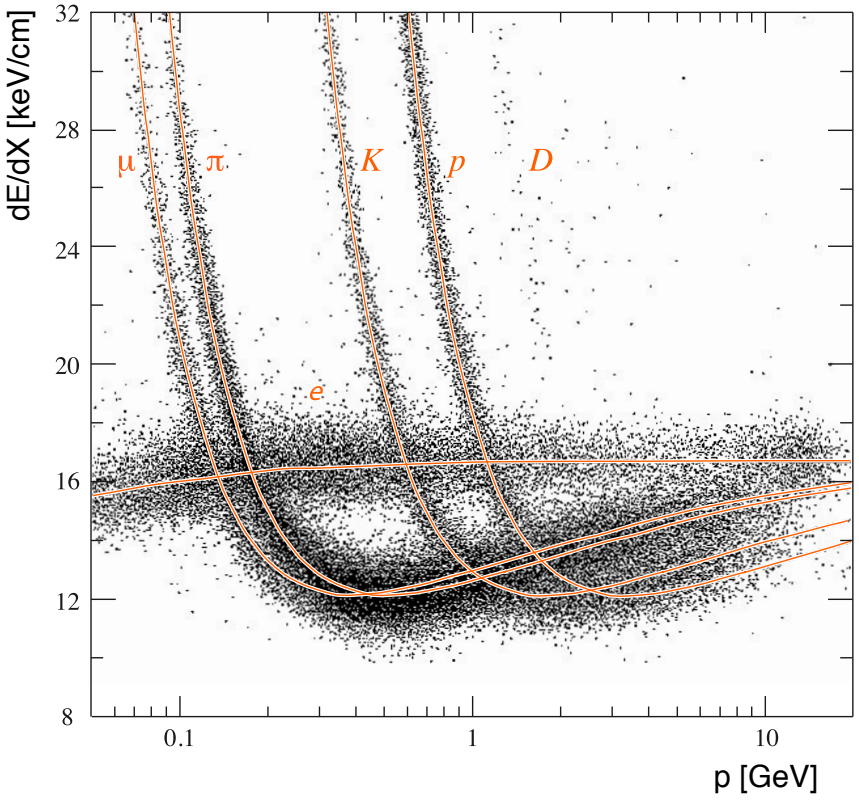

Figure 4.1: *Mean energy loss per path in dependence of the momentum for different types of particles. [12]*

For electrons with an energy of $E_{e^-} < 10\,\mathrm{GeV}$ the Bethe Bloch formula 4.1 has to be modified, since the interaction takes place between identical particles. The mean energy loss per length for electrons in matter due to ionization is [7]:

$$-\left(\frac{dE}{dx}\right)_{\mathrm{e,ion.}} \approx \frac{4\pi N_A \alpha^2}{m_e} \cdot \frac{Z}{A} \cdot \rho \cdot \left(\frac{\ln \gamma^2}{2} + D\right) . \tag{4.2}$$

Where $D \approx 7$ is material dependent value. For electron energies of ($E_{e^-} > 10\,\mathrm{GeV}$) the energy loss due to ionization is nearly the same as for heavy particles, as seen in figure 4.1.

For very high energetic electrons the overall energy loss is dominated by bremsstrahlung: due to their deceleration in the coulomb field of an atomic nucleus from the traversed material, the electrons emit electromagnetic radiation. The energy loss due to bremsstrahlung for relativistic electrons reads as follows [7]:

$$-\left(\frac{dE}{dx}\right)_{\mathrm{brems.}} \approx \frac{4 N_A \alpha^3}{m_e^2} \cdot \frac{Z^2}{A} \cdot \rho \cdot \ln\left(\frac{183}{Z^{1/3}}\right) \cdot E \tag{4.3}$$

where E is the energy of the electron, which is proportional to the energy loss. Figure 4.2 shows the energy loss for electrons as a function of the energy.

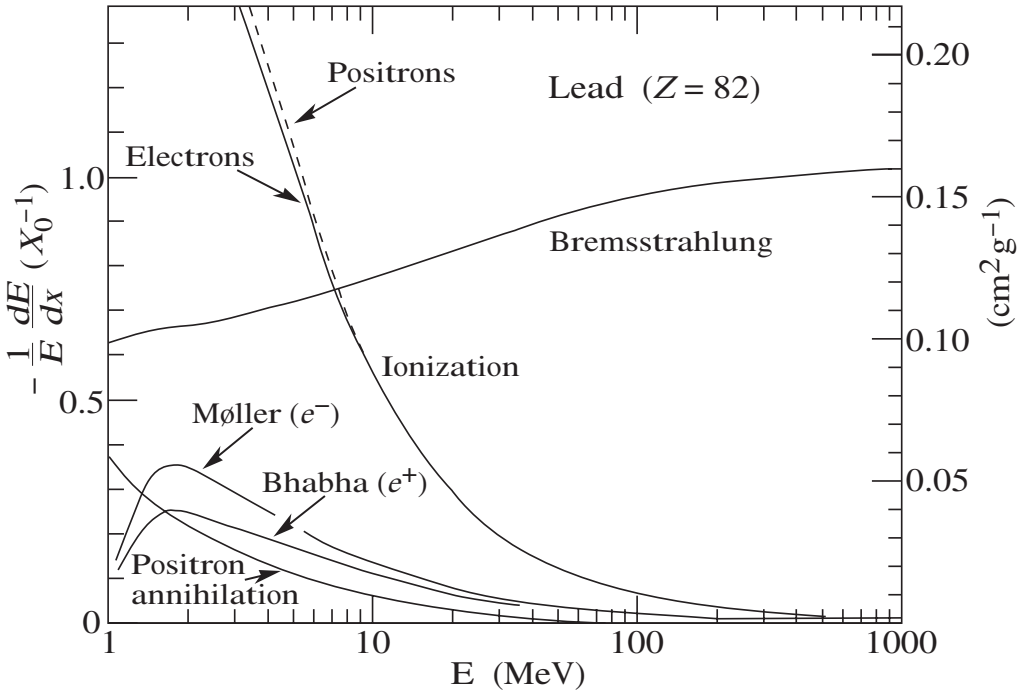

Figure 4.2: *Fractional energy loss per radiation length as a function of the energy for electron and positrons in lead. The dominating effect is ionization up to an energy of about $E = 10\,\mathrm{MeV}$. For higher energies the dominating effect is bremsstrahlung. For energies of $E < 10\,\mathrm{MeV}$ there is a small additional contribution from electron-electron scattering (Møller) or electron-positron scattering (Bhabha) and positron annihilation. [12]*

Electron drift

Electrons liberated in a gas due to ionization, rapidly lose their energy in collisions with the gas molecules until they only perform the random thermal motion. Following the kinetic theory of gases, the velocity is *Maxwell-Bolzmann* distributed:

$$f(v) = 4\pi v^2 \left(\frac{m}{2\pi kT}\right)^{3/2} \cdot \exp\left(\frac{-mv^2}{2kT}\right) \tag{4.4}$$

where $f(v)$ is the probability density, v the velocity of the electron, $m = m_e$ is the mass of the electron, $k = 1.38 \cdot 10^{-23} J \cdot K^{-1}$ the Boltzmann constant and T the temperature. The root mean square velocity is

$$\bar{v} = \sqrt{\frac{3kT}{m}} \ . \tag{4.5}$$

If an outer electric field is applied, the electrons get accelerated in the field, gaining more and more kinetic energy, until they collide with a gas molecule. A part of the kinetic energy gets lost in the collision, and the electron gets accelerated again. This motion superimposes the random thermal motion. When the mean acceleration and deceleration due to collisions obtain an equilibrium, the electrons drift with a constant velocity. The simplest approach for the determination of the electron's macroscopic drift-velocity is [27]:

$$v_D = \frac{eE}{m_e} \cdot \tau(E) \ , \tag{4.6}$$

where E is the strength of the electric field, e the charge of the electron, m_e its mass and τ the mean time between collisions, which depends on the electric field, the pressure and the type of gas. An additional impact on τ has the *Ramsauer-Townsend Effect*, the change of the cross-section when the *De Broglie wave* of the electron interferes with the De Broglie waves of the shell electrons of the gas atoms/molecules.

Townsend Avalanche

If the electric field is strong enough, so that electrons gain sufficient kinetic energy to ionize other molecules, they produce secondary electron-ion pairs. When the kinetic energy of the secondary electrons reaches the ionization potential V_0 of the gas molecules after the next collision the process starts over, a so-called *Townsend avalanche* begins. The probability of a secondary ionization per unit path length is given by the first Townsend coefficient

$$\alpha = \frac{1}{\lambda} \ , \tag{4.7}$$

where λ is the free mean path. Considering a liberated electron in a region of a constant field, strong enough to allow secondary ionization. After a mean drift

distance of α^{-1} an ionization occurs and two electrons will drift towards the anode. And after a next distance of α^{-1} it will be four of them. For n electrons and a drift distance dx the increase of the number of electrons will be

$$dn = n \cdot \alpha \; dx \; , \tag{4.8}$$

and therefore the total number of electrons

$$n = n_0 \cdot \exp(\alpha x) \; . \tag{4.9}$$

For the general case of a non uniform field, the first Townsend coefficient becomes a function of position: $\alpha = \alpha(x)$.

Several analytic approximations for α exist, valid for different gases and different strengths of the electric field. A general approach follows the assumption that all electrons having enough or more energy to ionize a gas molecule will ionize a molecule in a collision. It is assumes, that the collision is not elastic and the electron loses most of its energy in each collision. Consequently the electron needs to gain enough energy to produce an ionization within one free path [28]. If this requirement is fulfilled, the avalanche starts, since the field increases towards the wire and subsequent collisions happen with more energy. An empirical expression for α is:

$$\alpha = pA \cdot \exp\left(-B \cdot \frac{p}{E}\right) \tag{4.10}$$

where A and B are constant parameters. Table 4.1 shows typical values of A and B for different gases [26].

Gas	$\boldsymbol{A}$ [$\mathrm{cm^{-1}\,Torr}$]	$\boldsymbol{B}$ [$\mathrm{V\,cm^{-1}\,Torr}$]
He	3	34
Ne	4	100
Ar	14	180
Xe	26	350
CO_2	20	466

Table 4.1: *Parameters for the approximation of the Townsend coefficient*

Types of gaseous detectors

Based on the principle of accelerating ionization electrons in an electric field and measuring the resulting charge pulse in the gas, several kinds of detectors are distinguished. If the strength of the electric field is in a range that each collision occurs independently from other avalanches, the total amount of charge reaching the anode wire is proportional to the amount of charge freed in the traversal of the particle. Detectors using this principle are called *Proportional Chambers*. If the electric field

is too weak to allow the production of secondary electron-ion pairs, no avalanche takes place. Detectors working in this area are called *Ionization Chambers*. If the electric field is stronger than in a proportional chamber, the amount of charge saturates and is no longer proportional to the energy of the particle. When the entire gas in the volume is ionized the *Geiger Plateau* is reached. The readout is simpler due to the high amount of charge at the anode, but simultaneously the complete ionization causes a continuous current to flow. This discharge has to be quenched, resulting in a dead time. A typical gas ionization curve is shown in figure 4.3.

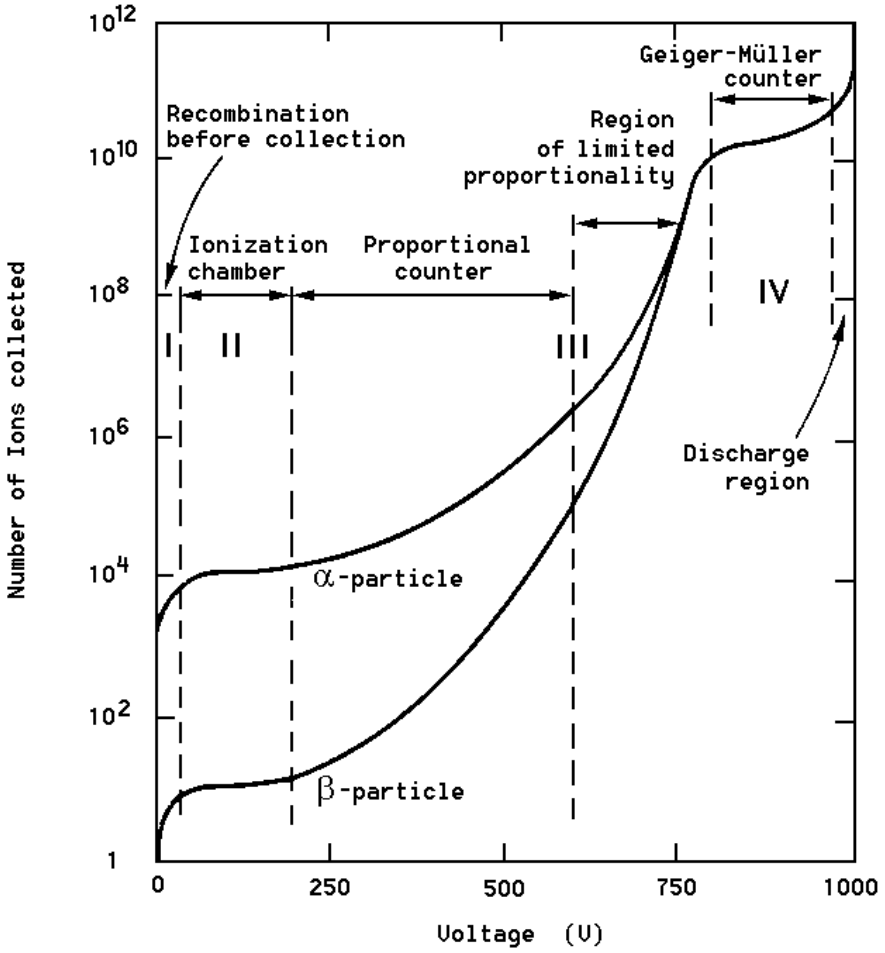

Figure 4.3: *Gas ionization curve. The number of collected ion pairs are plotted against the voltage between cathode and anode. The exact values depend on the geometrical structure of the detector and the electrodes as well as on the gas inside the volume. Taken from [29].*

The combination of many anode wires allows to follow the trace of the particle in a *Wire Chamber*, respectively a *Multi Wire Proportional Chamber* if the detector is working in the proportional region. Given the exact time of the traversal of the particle (i.e. by an external trigger) and the drift-velocity for electrons in the gas, the drift-time in the gas volume can be measured to improve the spatial resolution

of the detector. Detectors using this principle are called *Drift Chambers*. The CMS barrel muon chambers are of the latter type.

4.2 The Design of the CMS DT Chambers

The CMS barrel muon chambers use the processes of ionization and electron drift in the gas to detect muons in CMS. Due to the relatively low expected muon rate and the good resolution, the chambers can be used as tracking detectors. In the following section an overview of the DT muon chambers is given. In detail its design is described in [22].

4.2.1 The CMS DT Chambers

The CMS barrel muon chambers are drift tube (DT) chambers, consisting of three independent units, called *superlayer* (SL). Each superlayer is made of four layers of drift tubes[1], staggered by half a cell pitch. The superlayers are stacked on top of each other. Figure 4.4 shows a sectional view of a barrel muon chamber. The outer superlayers measure the projection of the muon trajectory onto the r-ϕ plane (CMS bending plane) and are therefore called Φ_1- and Φ_2-superlayer. The inner superlayer is rotated by 90°, in respect to the outer ones and measures the projection to the r-z plane (along the beam direction); this superlayer is called Θ-superlayer. A honeycomb structure used as spacer to provide a longer lever arm is mounted between the Φ_1-superlayer and the Θ-superlayer. Together with the known position of the chamber, the complete three dimensional spatial information of the muon trajectory can be determined with one chamber. The muon chambers in the MB4 station have no Θ-superlayer. In the final position inside the yoke, the Φ_1-superlayer faces the interaction point, the Φ_2-superlayer faces the outer edge of CMS. The wires in the Φ-superlayers are parallel to the beamline and in the Θ-superlayer perpendicular.

Local Chamber Coordinates

For the local measurement of angles by single chambers, local chamber coordinates are used. The angle φ is the angle to the normal to the chamber in the CMS r-ϕ plane, whereas ϑ is the angle to the normal to the chamber in the CMS r-z plane. A transformation between CMS coordinates (3.3) and local chamber coordinates can be performed by subtracting the inclination of the chamber from the CMS coordinate ϕ to obtain the local chamber coordinate φ. Since all chambers are mounted with no inclination in r-z plane, the local chamber coordinate ϑ is identical with the CMS coordinate θ.

[1] Since the drift tubes are the smallest repeated entity in the chamber they are often referred to as cell. Both terms can be used interchangeably.

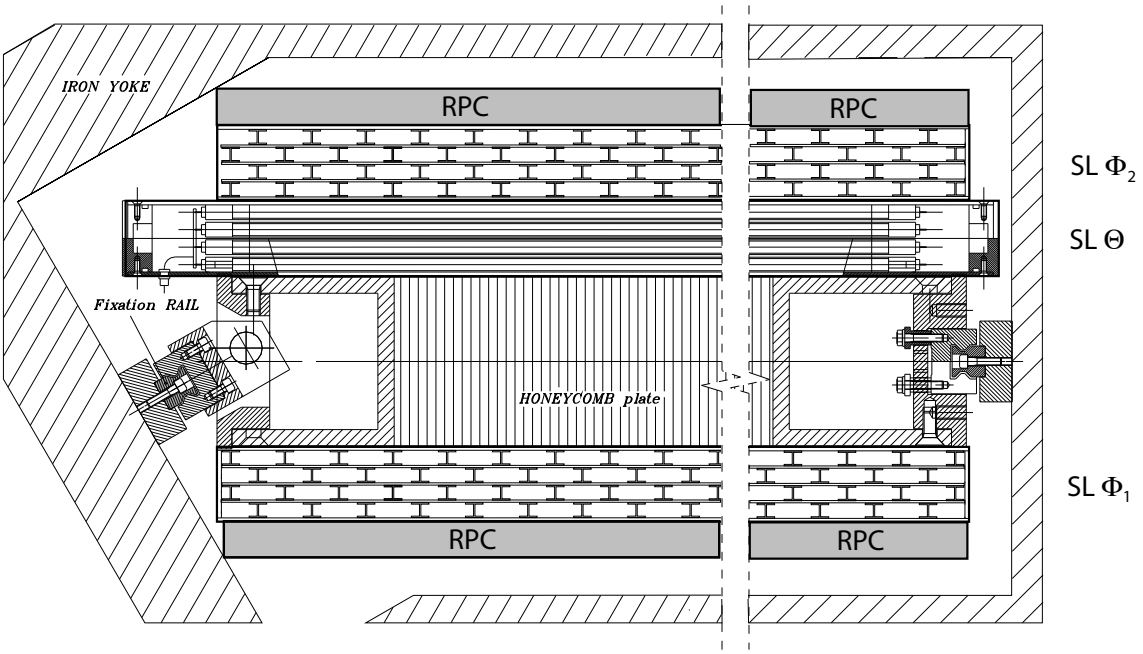

Figure 4.4: *Sectional view of a CMS barrel muon chamber. On top is the Φ_2-superlayer, and thereunder the Θ-superlayer, which is rotated 90° in respect to the Φ-superlayers. Between the Θ-superlayer and the Φ_1-superlayer is a honeycomb structure to provide a longer lever arm. The drift tube chamber is sandwiched between two RPCs (only in station MB1 and MB2) and mounted in the iron yoke. [17]*

The Drift Cell

Each drift tube has a 42 mm×13 mm cross-section. The length is different, depending on the type. Drift tubes for Φ-superlayers are 2531 mm long. Drift tubes for Θ-superlayers vary in the length for each station from 1990 mm for MB1 chambers up to 4190 mm for some MB4 chambers. The number of drift cells per layer in Φ-superlayers varies between 49 for MB1, 60 for MB2, 72 for MB3 and up to 92 for some MB4 chambers. In Θ-superlayers each layer has 57 drift cells. Altogether, the barrel muon chambers have 172 000 drift cells. The cells are filled with a 85% Ar and 15% CO_2 gas mixture at atmospheric pressure.

A sectional view of a drift cell is shown in figure 4.5. In the center of a drift tube is the anode, a stretched gold plated stainless steel wire, with a diameter of only 50 µm to utilize the $1/r$ dependence of the electric field. In the vicinity of the wire the field gets stronger, starting a Townsend avalanche increasing the charge up to a factor of 10^6. The anode voltage is +3600 V. Although the CMS drift tubes work in the proportional region only drift-times are measured, not the charge. The kinetic energy of the muons is determined by the bending of the trajectory due to the magnetic field.

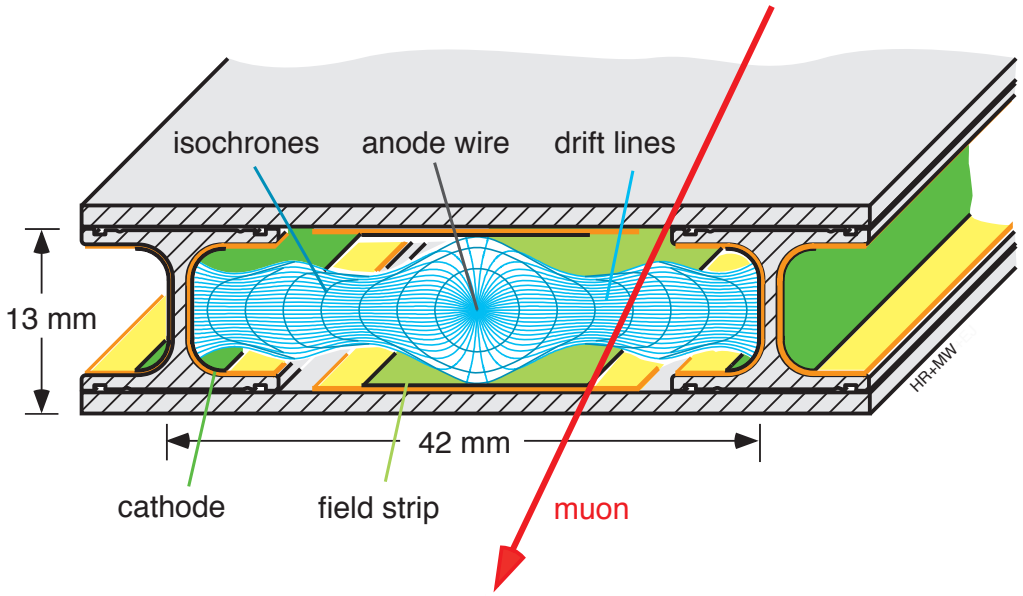

Figure 4.5: *Drift cell. The cathode at the I-beams is marked in dark green, the field strips in light green. Insulators are yellow. The electric field is drawn in the cell. [30]*

The cathodes with a voltage of −1200 V are integrated in the I shaped bar on the edge of a cell, as shown in figure 4.6. They are made of 50 µm thick and 11.5 mm wide aluminum tape, glued on a 100 µm thick and 19 mm wide insulating mylar tape. Additional field shaping electrodes with a voltage of +1800 V are placed on the upper and lower edge of the cell, also made of aluminum tape but 16 mm wide, glued on 23 mm wide mylar tape.They form the electric field as uniform as possible, to achieve a nearly linear time-to-drift-distance relation, especially under the influence of the magnetic field.

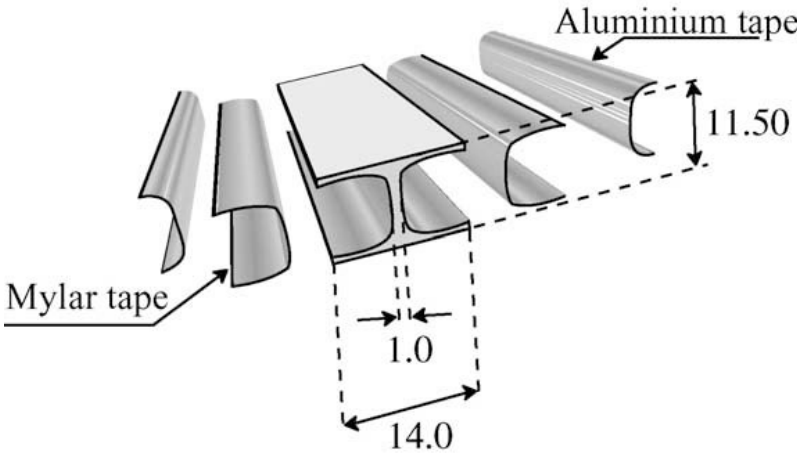

Figure 4.6: *The I-Beam is the structure dividing the cells and shoring the layer. Insulated by a mylar tape, an aluminum tape is applied an the inner side, forming the cathode of the cell. All values are in* mm. *[31]*

4.3 The On-Chamber Electronics

The CMS drift tube chambers contain a highly integrated electronics for readout, trigger and service. To handle the huge amount of data, a very fast preprocessing of the data is inevitable, performing a local reconstruction to provide a trigger signal and a bunch crossing identification. The readout can be restricted to the moment of an event, reducing the data overhead. A sophisticated electronic is mounted in the chamber to perform this task.

The Front End Board

After arriving at the anode wire, the signal from the avalanche of drifting electrons, generated by a muon passing the gas volume is first amplified and compared with a programable threshold value, typically between 15 mV and 25 mV. This is done in the front end boards, mounted inside the gas volume at the superlayers front side. It provides a discriminated signal for further processing in the read out chain. To reduce power consumption and potential noise sources, the task is performed in *Application Specific Integrated Circuits* (ASIC), developed for this purpose [32]. These integrated circuits, called MAD are made in 0.8 µm BiCMOS technology, it's input lines are connected via a 470 pF capacitor with the drift tubes wire. Each chip has the capability to process the signal from four wires, each front end board contains four MAD chips and hence can serve 16 channels. A photo of a front end board is shown in figure 4.7.

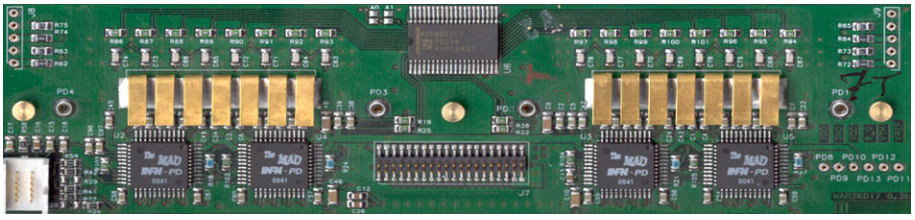

Figure 4.7: *Front End Board. In the bottom part of the board the four MAD chips can be seen. [17]*

MiniCrate

The on chamber electronics, referred to as *MiniCrate* (MC) provide the readout and the local DT trigger as part of the Level-1 trigger (3.8) for the drift tube chambers. The MiniCrate is made of an aluminum frame, mounted on the honeycomb structure of a drift tube chamber, housing the electronics. Each MiniCrate consists of several sub-components, namely a *Server Board* and a *Central Control Board* (CCB), three to seven *Read Out Boards* (ROB) and *Trigger Boards* (TRB), depending on the size of the chamber as well as two link boards: for communication purposes the *ROB Link Board* and for controlling the *CCB Link Board*. The setup of sub-components

for each MiniCrate type can be seen in figure 5.7, a schematic view of an MB1 MiniCrate is shown in figure 4.8.

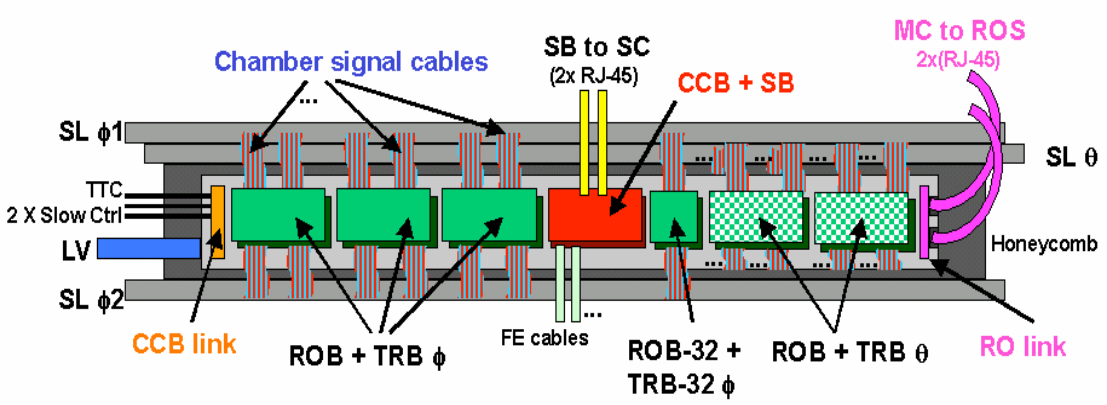

Figure 4.8: *Schematic view of the MiniCrate of an MB1 chamber. [33]*

The read out boards receive the analog signal from the front end boards and digitize the data. For the digitization high performance *time to digital converters* (TDC) are used. These TDC were developed by the CERN Microelectronics group [34] in IBM 25 µm CMOS technology and each provide 32 channels using the delay locked loop (DLL) principle. The TDC is clocked by the 40 MHz LHC timing, thus one clock cycle is 25 ns long and the size of one time bin computes to $^{25}/_{32}$ ns = 0.78 ns. This corresponds to a RMS time resolution of 265 ps. One read out board subsumes four TDCs in a clock synchronous token ring with a bypass on error logic, maintaining 128 channels and thus 128 drift tube cells. The *timing and trigger control* (TTC) signals are received by the ROB from the CCB.

For the identification and selection of segment candidates, corresponding to each ROB one trigger board is installed in the MiniCrate. The trigger boards contains two major entities, the *bunch crossing and track identifier* (BTI) and the *track correlator* (TRACO). The BTI is an ASIC implemented in 0.5 µm CMOS Standard Cell technology for the purpose of searching patterns of a minimum of three aligned hits. One BTI observes nine adjacent channels, distributed over all four layers of one superlayer, as seen in figure 4.9. The trigger candidates are selected independently for the Φ- and the Θ-superlayers. Two neighboring BTIs overlap by five channels to cover the whole range of possible track angles. Since the maximum drift-time in a cell is 380 ns, but the bunch crossing rate is one BX per 25 ns an assignment of the hits to a bunch crossing is crucial. Each signal from a wire is stored in a shift register where it remains as long as the maximum drift-time lasts. The BTI compares the relative positions of the hits in the register at each clock using a meantimer method [35]. Once a hit pattern is identified it can be assigned to a bunch crossing.

The TRACO correlates the segment candidates of the two Φ-superlayers, to obtain a pair of segments that fits the best track, with improved precision. It selects up

to two trigger candidates for further processing. The TRACO is an ASIC made in CMOS 0.35 µm Gate Array technology. One TRACO evaluates the signals from four BTIs of the inner Φ-superlayer and twelve BTIs of the outer Φ-superlayer to cover the full angular range.

Figure 4.10 shows the trigger acceptance for the combined BTI and TRACO algorithms as a function of the incident angle, measured by the TRACO. Up to ±35° the trigger acceptance is flat and about ²/₃ of the events are correlated. Beyond ±35° the fraction of uncorrelated events increases, while the fraction of correlated events decreases up to about ±55°. For higher angles the acceptance decreases and muons with an incident angle more than approximately ±60° does not trigger the chamber.

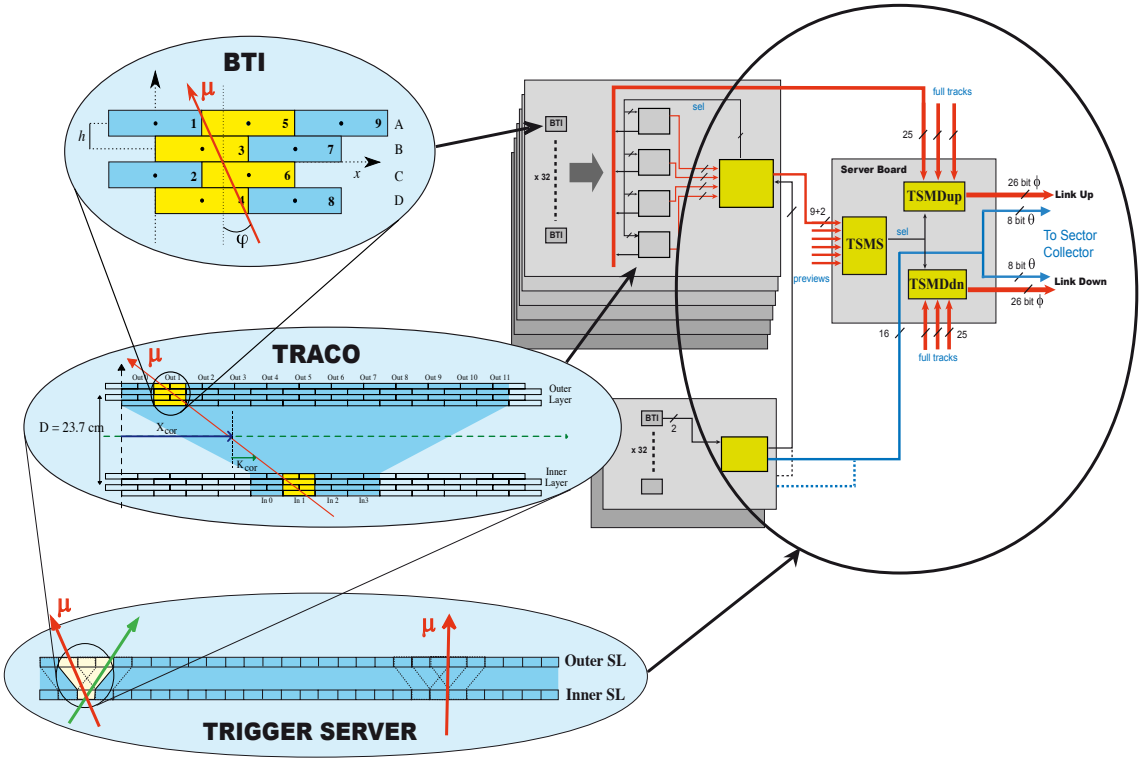

Figure 4.9: *Local trigger of the muon drift tube chambers. [17]*

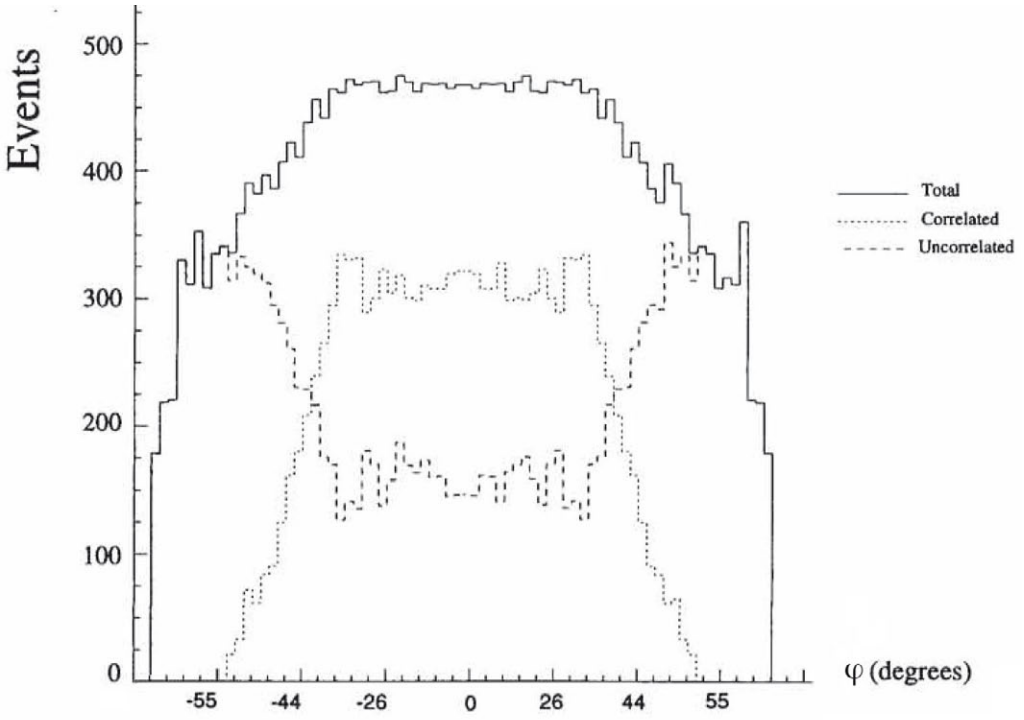

Figure 4.10: *Angular acceptance of the trigger combined for BTI and TRACO as a function of the local incident angle φ. The dotted line shows the acceptance for segments from both Φ-superlayers correlated by the TRACO, the dashed line indicates uncorrelated segments. The total acceptance is drawn with the solid line. [22]*

5 Commissioning

5.1 Cosmic Ray Muons

For the commissioning and testing of the performance of a muon spectrometer one needs muons. During the commissioning of CMS, the LHC accelerator was still under construction. Thus an additional highly available and convenient muon source was necessary. A test with a muon test beam has been performed for several chambers [36], but is not suitable for commissioning purposes, since the chambers should be operated in their final positions, and working on the chamber while taking data with a test beam is not possible due to reasons of radiation protection. Fortunately a persistent source of muons free of cost is provided by nature: *Cosmic Ray Muons* which hit the earth's surface at a constant rate, high enough to collect a sufficient amount of data in a reasonable time. The following explanation is based on [12], [37], [38] and [39].

Sources of cosmic rays

Cosmic rays are ionizing particles from outer space, interacting in the earth's atmosphere with an event rate of about $1000\,\mathrm{cm}^{-2}\mathrm{s}^{-1}$ [37]. Various processes and sources are contributing to the cosmic ray spectrum. They consists of 98% nuclei[1] and 2% electrons. The energy spectrum of cosmic rays can be approximated by the following equation:

$$\frac{\mathrm{d}N}{\mathrm{d}E} \propto E^{-\gamma} \tag{5.1}$$

Where $\gamma \approx 2.7$ for nuclei with an energy up to about $10^{15}\,\mathrm{eV}$ and $\gamma \approx 3$ for nuclei with an energy above $10^{15}\,\mathrm{eV}$. The maximum particle energy can exceed $10^{20}\,\mathrm{eV}$. The steepening in the energy distribution around $10^{15}\,\mathrm{eV}$ is called the *knee* of the spectrum. Around $10^{19}\,\mathrm{eV}$ the spectrum flattens again, this is called the *ankle*. Figure 5.1 shows the energy spectrum of primary cosmic rays. The distribution is hitherto not completely understood and subject of several ongoing experiments.[2] One possibility is, that the knee is a saturation limit on the maximum energy for accelerating galactic processes like supernovae or pulsars. The ankle could reflect the

[1] Where 87% of the nuclei are protons and 12% are α particles. The remaining one percent are nuclei from heavier elements.

[2] Especially to be mentioned here is the Pierre Auger Observatory [40], which examines ultra high energetic cosmic ray particles with combined ground based and air-fluorescence-detectors.

energy where extragalactic sources contribute more than galactic ones. For nuclei with an energy around 1 GeV the dominating source is solar. Nuclei with an energy above 10 GeV approach the earth isotropically, below 10 GeV the interaction between charged particles and the earth's magnetic field creates a directional dependence.

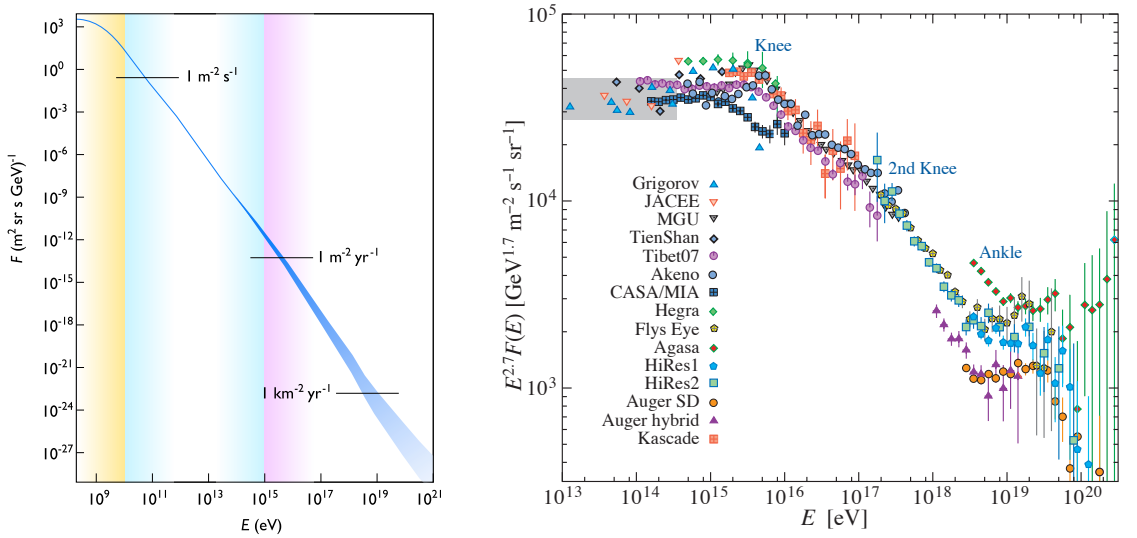

(a) *Cosmic ray energy spectrum. The yellow region is dominated by solar cosmic rays, the blue one by galactic and in the purple region extragalactic cosmic ray are most frequent.* [41]

(b) *Detail of the cosmic ray energy spectrum. The flux is multiplied by $E^{2.7}$ to emphasize the knee and ankle. The data points are from air shower measurements, except the ones in the grey shaded area which have been measured directly.* [12]

Figure 5.1: *Flux of the cosmic ray in dependence of the energy.*

The origin of cosmic ray muons

When cosmic ray particles interact with the molecules of the air in the upper atmosphere, a cascade of particle interactions, called air shower gets initiated. This air shower consists of three components: A hadronic, an electromagnetic and a muon component. An illustration of an air shower is shown in figure 5.2.

In multiple inelastic collisions between the cosmic ray nuclei and the nuclei of the air molecules particles like pions, K or η mesons and others are produced. Before they decay, these particles can interact again with nuclei from air molecules, starting a cascade, until the energy per particle is below the pion production threshold. Together with fragments from the nuclei these particles form the hadronic component of the air shower.

The neutral pions decay almost instantaneously, with a mean lifetime of $\tau = 8.4 \cdot 10^{-17}$ s, predominantly (98.8%) in two photons [12]:

$$\pi^0 \rightarrow 2\gamma \tag{5.2}$$

This is the starting point for an avalanche. The high energy photons interact with nuclei from air molecules forming an electron - positron pair, which subsequently emit photons again, when they pass close by a nucleus and get accelerated in their electromagnetic field. These photons again undergo pair production, a process which repeats until the photon energy is below the pair production threshold of $2 \times 0.511\,\mathrm{MeV}$, forming the electromagnetic component of the air shower.

The charged mesons decay into muons and neutrinos, e.g. the charged pions decay with a branching ratio of 99.99% and a mean lifetime of $\tau = 2.6 \cdot 10^{-8}\,\mathrm{s}$ into a muon and a neutrino [12].

$$\pi^+ \rightarrow \mu^+ \nu_\mu \qquad \pi^- \rightarrow \mu^- \bar{\nu}_\mu \qquad (5.3)$$

Muons have a mean lifetime of $\tau = 2.2 \cdot 10^{-6}\,\mathrm{s}$ and decay into an electron and two neutrinos [12].

$$\mu^- \rightarrow e^- \bar{\nu}_e \nu_\mu \qquad \mu^+ \rightarrow e^+ \nu_e \bar{\nu}_\mu \qquad (5.4)$$

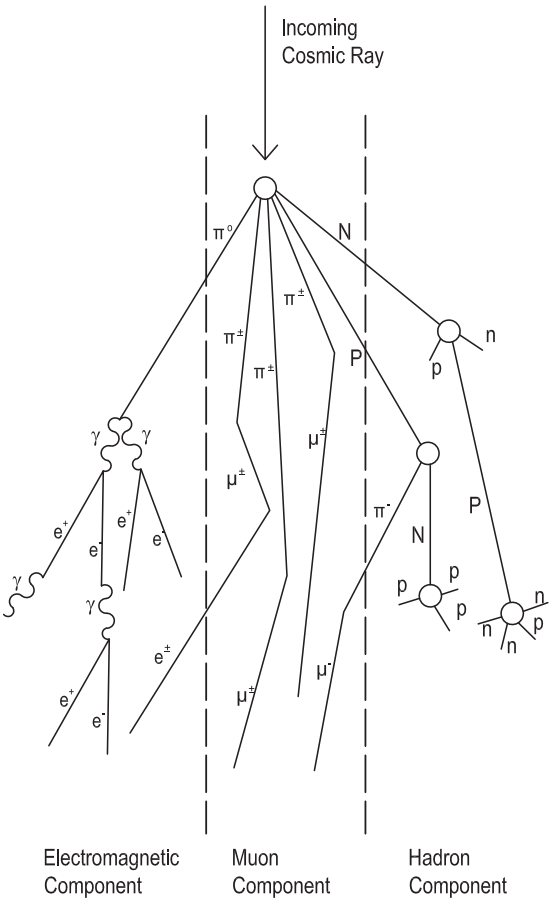

Figure 5.2: *Air Shower*

The electrons from the muon decays are counted as part of the electromagnetic component. Due to the fact, that the muons are relativistic, a high fraction of the muons can reach the earth surface before decaying[3], although produced in altitudes around 15 km. They form the muon component of the air shower.

Characteristics of cosmic ray muons

On their way down to the earth's surface, the muons lose about 2 GeV due to ionization, as described in the Bethe-Bloch equation (4.1). The mean energy at sea level is $\approx 4\,\mathrm{GeV}$. The flux of muons with an energy of a few GeV is affected at the 10% level by geomagnetic effects and the solar activity. The muon spectrum between 10 GeV and 100 GeV is dominated by the pion decay. For higher energies the spectrum decreases more, since the primary spectrum decreases and above $\epsilon_\pi = 115\,\mathrm{GeV}$ a hadronic interaction is more likely for pions than a decay [42] and the primary

[3] 2.4 GeV muons have a decay length of about 15 km, which is reduced by energy loss in the air to 8.7 km [12]

spectrum is decreasing. The spectrum for cosmic muons is shown for two different incident angles in figure 5.3. For large incident angles, the spectrum shifts to higher energies, since parent mesons travel longer through thin areas of the atmosphere, increasing their likeliness to decay while low energy muons are more likely to decay due to the increase of the flight paths length [12].

Vice versa, the angular distribution of cosmic ray muons depends on the energy. Muons with energies below the GeV scale are distributed steeply around the zenith. The distribution flattens for higher energies to a $\cos^2 \alpha$ shaped distribution for muons with a few GeV. For muons at very high energies of $E_\mu \gg \epsilon_\pi = 115\,\text{GeV}$ the angular distribution is shaped as a $\sec \alpha$ distribution for angles $\alpha < 70°$. The parent mesons of these muons are more likely to perform a hadronic interaction, unless their incident angle is high, then they may decay in the thin areas of the atmosphere, leading to a superior number of high energy cosmic muons for large incident angles.

For the overall flux of cosmic ray muons, the dependence on the zenith angle α reads as follows:

$$I_\mu = \frac{dN}{d\cos\alpha} \propto \cos^2 \alpha \tag{5.5}$$

Positive muons μ^+ dominate over negative muons μ^- by a factor of $\frac{N_{\mu^+}}{N_{\mu^-}} \approx 1.3$. This charge ratio depends on the muon energy, since several competing processes contribute to the muon production. Basically, the charge ratio is dominated by the excess of positive charged particles, in particular protons. Further information and results about measurements of the cosmic ray muon charge ratio can be found in [43, 44].

The flux of cosmic muons at sea level is $I \approx 70\,\text{m}^{-2}\text{s}^{-1}\text{sr}^{-1}$ for vertical muons with an energy above 1 GeV [12]. For a horizontal detector without shielding an event rate of $I \approx 1\,\text{cm}^{-2}\text{min}^{-1}$ is expected at sea level. In the CMS assembly hall at an altitude of $\approx 500\,\text{m}$ the flux is expected to be a few percent higher, providing a perfect source of muons for the commissioning of the CMS muon detector.

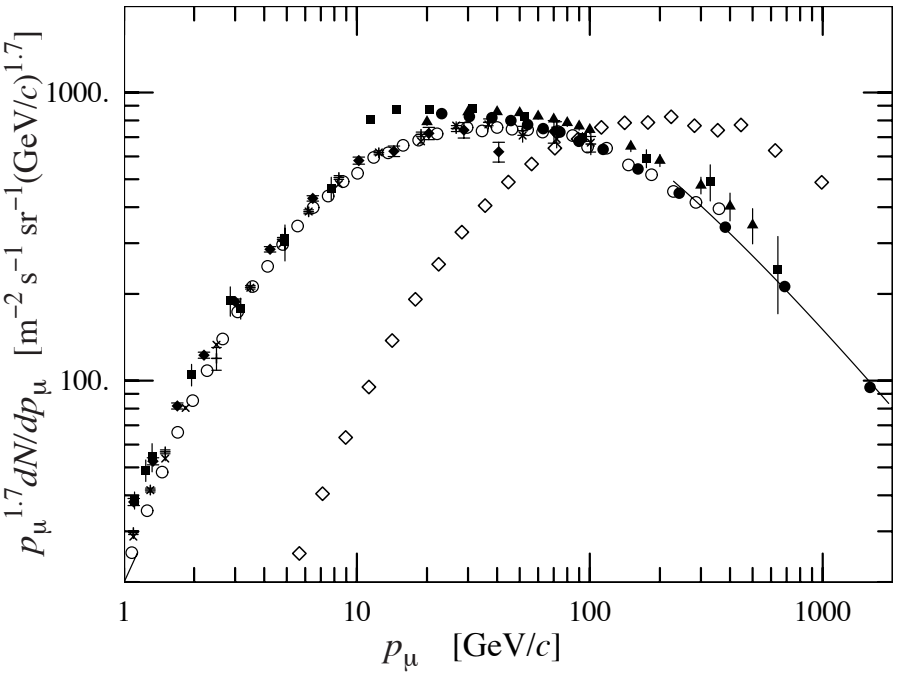

Figure 5.3: *Cosmic ray muon spectrum at sea level. The ⋄ indicate an incident angle of $\alpha = 70°$, the other markers are from perpendicular muons with $\alpha = 0°$ taken in different experiments [12]. The spectrum is shifted to higher energies for large angles since the traveling path in the atmosphere is longer: low energy muons decay before reaching the earth's surface and high energy pions decay before they interact.*

5.2 The Commissioning Procedure

The drift tube chambers for the station MB1, as well as the "feet chambers" in sector S9 and sector S11 of the station MB4, have been produced at the III. Physikalisches Institut A at RWTH Aachen University between 2001 and 2006.

Before the chambers were transported to CERN, they have undergone a series of training and testing steps at the production sites [45], [46]. The chamber performance was verified at the test stand in Aachen, but with proprietary electronics, rather than the final on-chamber and off-chamber electronics. After arrival at CERN, the chambers were completed with the on-chamber electronics (MiniCrate) (4.3), which have been developed and produced at the INFN Bologna, INFN Legnaro and the Ciemat Madrid, and tested again. It should be noted that all of these tests were conducted with a horizontal chamber orientation. After installation in their final positions in the iron yoke, other chamber orientations were available. Although optimized for muons from pp interactions (which would always hit the chamber plane more or less vertically) cosmic ray muons provide again a useful (and the only available) source of particles to verify the chamber performance.

The commissioning procedures are qualitatively different from the preceding steps, since the chamber position inside the yoke (and hence their orientation) is final, as well as the readout and trigger electronics mounted on the chamber. The chamber electronics, described in more detail in section 4.3 is much more advanced than the muon electronics used in previous experiments, for example its capability for online segment reconstruction and bunch crossing identification. Final electronics was mostly unavailable for earlier testbeam and cosmic ray tests. It is therefore not surprising that the commissioning turned out to largely test the electronics rather than the chambers. It is the last chance to have easy access to the chambers and their electronics, since the final cabling is running tightly over the chamber electronics, hence preventing later access to the chamber's front-end electronics. Access to the Θ-superlayer is already limited after mounting the chamber in its tray in the barrel yoke. Thus, it is very important to find and fix any possible failure. During commissioning, about $^1/_3$ of all chambers had to be accessed for minor repairs. Among other problems, a commonly occurring intervention - about 10% of the chambers - was a repair or replacement of the trigger board (TRB). About 5% of the chambers had cabling errors and about 1% of the link boards got exchanged. Only few problems had an impact on the whole chamber, for example a broken CCB. More often interventions concerned a group of channels, like TRB related problems. Due to the zero error policy, the corresponding part got exchanged, even if only a single channel was effected.

These commissioning procedures include a series of tests completed by an extensive acquisition of data from cosmic ray muons. The electronics testing consists of the following parts:

1. Connecting fibers and cables. A temporarily cabling is brought up by hand, to connect the chamber with the data acquisition (DAQ) setup, including TDC and trigger data lines, chamber control lines and clock signal as well as power lines.

2. Testing the MiniCrate with fixed electronics pattern. Several tests of the successful operation of the electronics are performed. These tests are done with controlling software only, no cosmic ray muons are required.

3. Configuring the MiniCrate for the relevant chamber type. The on-chamber electronics is not chamber specific per se, but the MiniCrates firmware can be configured to match the chamber type. Depending on the sector and station type, the number of readout and trigger boards varies from chamber to chamber, and so do the left/right shift between Φ_1- and Φ_2-superlayer, as shown in figure 5.7.

4. Configuring the DAQ. Since the data acquisition system used in the commissioning is not the final one, it needs a configuration for each chamber type,

like the MiniCrate do, including the station and the shifts between the Φ_1- and Φ_2-superlayers, as shown in figure 5.7.

5. Measuring the signal latency with test pulses. Each channel in each chamber has a unique latency, which is determined at this commissioning step.

6. Starting the data acquisition. About one million events of cosmic ray muons are recorded per chamber. Several runs with different trigger configurations are performed to obtain a sufficient amount of data.

7. Performing the data quality monitoring (DQM). The data has to be verified instantaneously to ensure the quality of the recorded input, since an accidental misconfiguration of the MiniCrate or the DAQ can result in useless data.

One of the CMS specifics is the assembly of subdetector components in the surface (SX5 hall) thus providing the clear advantage of a significantly higher cosmic ray muon flux than underground. During this step the single chamber commissioning took part. After assembly, the wheels of CMS have been lowered into the underground cavern (UXC55). Since other subsystems simultaneously work at the CMS surface assembly hall, like the alignment, the magnet or groups from other subdetectors, all detector operations have to respect a well defined and tight time schedule. For that reason there are two - later even three - setups for the commissioning of several chambers in parallel.

5.2.1 Cabling

As the first step, each chamber has to be provisionally connected to power supplies and the DAQ readout. A temporarily cabling is used in order to potentially allow access to the chamber if needed. Several connectors have to be plugged onto the chamber: The low voltage, high current power supply which is to be connected to the low voltage patch panel box next to the chamber as seen in 5.4 (b), the low voltage power supply for the splitter board 5.4 (c), two twisted pair cables for the trigger signal output, two twisted pair cables for the TDC data output, one optical fiber for the time and trigger control (TTC) signal and one optical fiber for the communication with the MiniCrate.

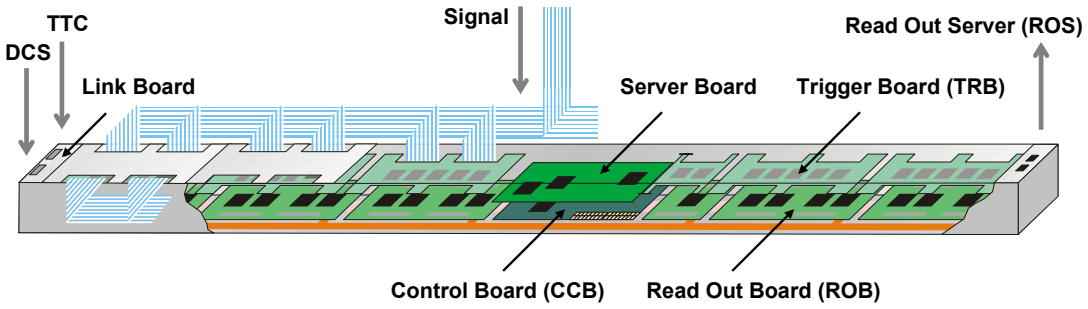

(a) *schematic view of the MiniCrate with input and output links. [47]*

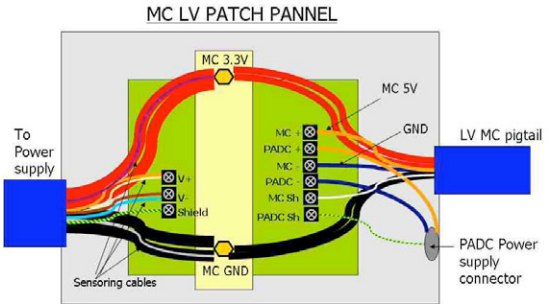

(b) *Drawing of the patch panel for the low voltage supply. [48]*

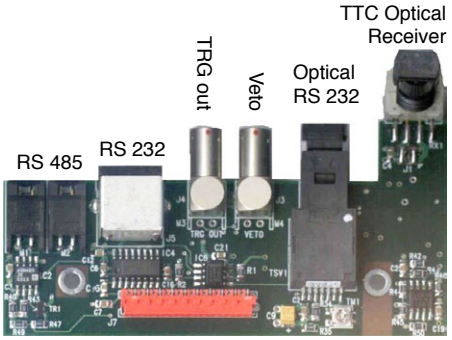

(c) *Link board for the connections to the TTC and the detector control system (DCS). [48]*

Figure 5.4: *Connections and connectors to and from the MiniCrate.*

5.2.2 MiniCrate Tests

Once connected, the on-chamber electronics is being configured and subsequently tested. Several test programs used during the MiniCrate assembly also allowed detailed check-up's. The first test is a *boundary scan*, a standardized procedure to test the interconnections inside a circuit without having physical access to the circuit [49]. For that purpose the MiniCrate has a JTAG port through which the access to the circuit is realized. Via JTAG a signal is driven onto a pin of an integrated circuit which follows a given trace to an output pin. There the state is read and compared with the correct result already saved before. This is done in sequence one-by-one for all pins of the integrated circuits.

After verifying with the boundary scan that the hardware is in good condition, test programs for the various functions are executed. The software for these tests is programmed using LabVIEW [50], a visual programming language. The LabVIEW programs appear as so-called "Virtual Instruments" which allow to operate the tests on a visualized front panel, as seen in figure 5.5 and figure 5.6. The test series include the following steps:

- FE TEST: A general examination of the front-end board's functioning.

- TDC DISPLAY: A scheme of the used TDC channels. Each of the 32 channels from a TDC is visualized by a LED. Depending on the chamber type specific channels have to be active. The shown patterns have to match the channel assignment for the chosen chamber type. An example screenshot is shown in figure 5.5.
- TDC CROSSTALK: This test verifies that no crosstalk between the channels of the TDC occurs.
- CROSSTALK: In this check-up the crosstalk in general in the electronics is measured.
- TP THRESHOLD: An evaluation of the test pulse threshold. The fine-tuning of the threshold is important, since a lower threshold increases noise and crosstalk, but a too high threshold results in missing events. The final threshold value is 15 mV. In the chamber commissioning the threshold was raised up to 25 mV.
- TP CABLE: Is a test for validating, that all signal cable connections inside the chamber are correct and no cables are unplugged or swapped.
- PU TIMING: In this test it's verified that the clock to the serializer on the server board is in correct phase.
- TRB emulator: To testify the BTI on each trigger board, the recognition of imitated track patterns is confirmed. Generated track patterns are transmitted to the trigger board and the result is compared with the input.
- TRB TP: A test pulse based check of the trigger board.

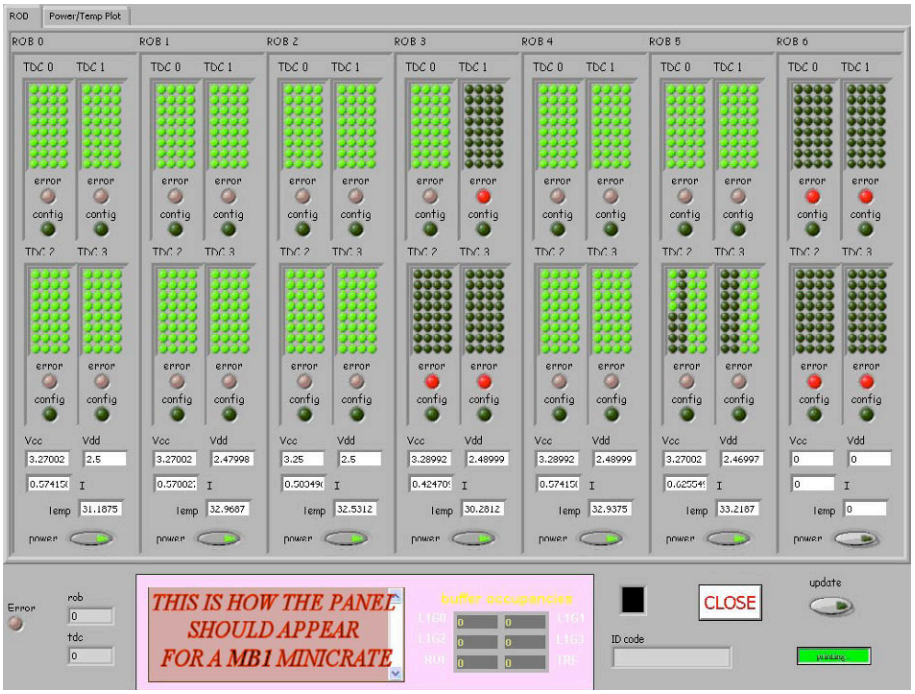

Figure 5.5: *MiniCrate Test: TDC Display. The read out boards (ROB) are illustrated schematically in columns of two TDCs. Every ROB contains four TDCs which are illustrated as blocks of 32 LEDs. Each LED represents one channel. This test reads and displays the active channels. The result is to be compared with a reference layout of each chamber type. The chamber type shown here is an MB1 chamber: ROB 6 is not used (see figure 5.7), as well as the TDCs 1,2,3 in ROB 3 and some channels in TDC 2,3 ROB 5*

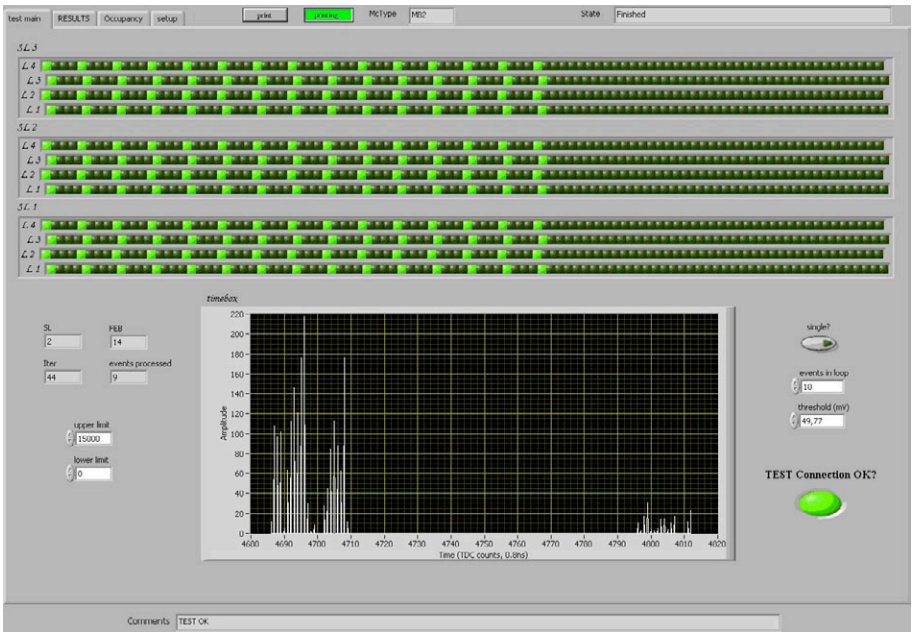

Figure 5.6: *MiniCrate test: test pulse cable connection. This test verifies all cable connections. In each cable all channels are masked, except the first one. This allows the easy identification of swapped cables. If everything is correct, each fourth LED is on, as seen above. The number of channels refers to the chamber type. Here an MB2 chamber is shown.*

5.2.3 Trigger

In the commissioning a dedicated trigger configuration has been used, since only single chambers were readout. The final trigger uses coincidence of two chambers. In its final position in the barrel yoke an external trigger could not be used and the chamber had to trigger itself. This procedure, called *autotrigger* is implemented in the on-chamber electronics firmware. This trigger configuration is specific for the measurement of cosmic ray muons since the original trigger acceptance has to be modified for correct treatment of strongly inclined muons. Two types of trigger patterns are defined. *H* (high) represents four aligned hits in one superlayer, recognized in the BTI and *L* (low) refers to the recognition of three aligned hits in one superlayer, see figure 5.8.

(a) *H: four aligned hits. The red cell indicates a noise hit discarded by the trigger.*

(b) *L: three aligned hits*

Figure 5.8: *Trigger patterns*

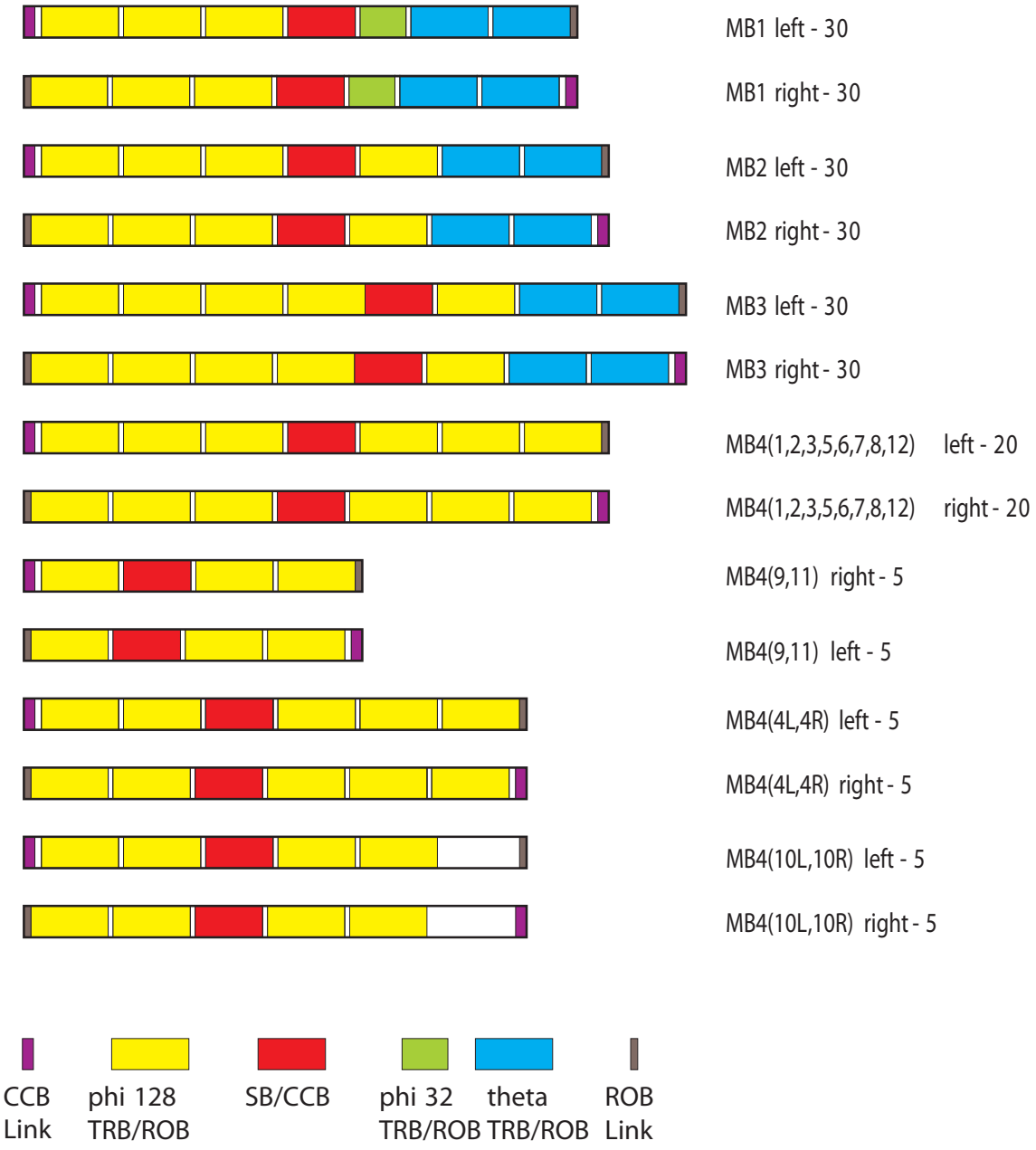

Figure 5.7: *A sketch of the different chamber types MiniCrate layout. Depending on the type, three to six boards for the Φ-superlayers' trigger and readout are integrated. Each chamber has one central control board and one link to it, as well as one link for readout. All chambers, but MB4s have two boards for the Θ-superlayer trigger and readout. [51]*

In the chamber commissioning the following trigger configurations were used:

- *HH+HL* requires four aligned hits in one Φ-superlayer and a minimum of three aligned hits in the other Φ-superlayer.
- *Hanytheta* demands either the prerequisites of the HH+HL configuration or an uncorrelated H in one Φ-superlayer but confirmed by the Θ-superlayer with either H or L.
- *Default* asks for either four aligned hits in one Φ-superlayer and a minimum of three aligned hits in the other Φ-superlayer or the recognition of four hits in one Φ-superlayer confirmed by an uncorrelated recognition of at least three hits in the other Φ-superlayer or the Θ-superlayer.

If the conditions for the current trigger configuration are fulfilled, the readout is started with a constant latency.

5.2.4 Test Pulse Run

The ability to generate test pulses was implemented in the MiniCrate to allow a test of the front-end electronics without wire signal. No high voltage or gas is needed and even cells with disconnected wires may provide a test pulse, since the test signal is generated in the on-chamber electronics and does not propagate along the wire.

The test pulse run during the commissioning is done to determine the latency of individual cells. Due to different cable lengths and minor differences in the arrangement of the electronics each channel has a unique latency. To improve the resolution of the DT muon system, the drift-times are corrected by the latency values in the reconstruction (6.3.2) of the muon track to align the synchronization of individual cells. Since these latency offsets are a fixed chamber characteristics, they can easily be absorbed in a database. The data gained in the commissioning will be used by the final DAQ system.

For the determination of the latency offset a signal is driven to the front-end board generating simulated hits and causing the trigger to start the read-out. Subsequently the TDC times are compared, thus determining the relative latencies [16].

Inside the chamber two different cables inject the test pulses. One cable serves the even layers $L2$ and $L4$, the other one the odd layers $L1$ and $L3$. Since the signal injection cables have a latency too, an additional offset per layer has to be taken into account. A distribution of the latency values can be seen in section 8.1.

5.2.5 Taking Data

A minimum of one million events of cosmic ray muons is recorded to obtain a uniform illumination of the chamber and enough statistics for the analysis. Depending on the trigger rate and the chamber size this takes about two hours. For MB1, MB2

and MB3 chambers the *Hanytheta* trigger configuration is used, MB4 chambers lack the Θ-superlayer and hence are configured with the *HH+HL* trigger configuration. Smaller data samples of about 100 000 events are taken with the other trigger configurations.

Directly after data taking, a subset of the data gets processed by the so-called *Data Quality Monitor* (DQM), a data analyzer based on the CMS specific software ORCA (6.1), to have a fast feedback on the quality of the data. This step provides an instantaneous control of the recorded data to ensure their correctness and exclude possible misconfigurations of the DAQ or MiniCrate which would result in useless data.

Additionally the DQM generates diagnostic keyplots allowing a glance overview to the recorded data without the need of an additional analysis software. These keyplots are published on the internet shortly after commissioning. The data taking for the single chamber commission in the surface hall took place in several rounds between May 2005 and February 2007.

6 Tools for Reconstruction

6.1 The Reconstruction Software Framework

For the analysis of the data the software framework CMSSW [52] has been used. CMSSW is "the software of CMS", an object orientated data analysis framework written in C++. It contains the necessary code for the analysis and the reconstruction of physics objects of all subdetectors, as well as the ability to generate Monte Carlo simulations of the data measured in the CMS detector, visualize events in an event display or do calibration and alignment tasks. For all these functions only one executable is needed. In order to perform a specific task a configuration file is read in, where the job is defined. This configuration file contains the information which modules to run, the order of the modules and all individual parameters for them [53]. CMSSW is still under development and new versions are released frequently. It is a further development from its predecessor framework ORCA [54]. Although a major part of the framework has been rewritten when moving from ORCA to CMSSW the basic characteristics of the local muon reconstruction in the drift tubes has not changed. For that reason the following descriptions focus on the reconstruction chain of CMSSW. For the analysis described in this thesis, the versions CMSSW_1_1_0, CMSSW_1_2_0 and ORCA_8_7_3 have been used.

CMSSW is structured using a data model called *Event Data Model* (EDM), with the physics event (i.e. a muon passing the detector) on top of the hierarchy. Technically an event is the result of the readout after a single trigger. These data are stored in a C++ object container. All objects derived from the events are accessed through the event object and stored in the event object container. Thus the event object contains all data from the triggered physics event up to the reconstructed tracks, allowing to access every stage of the reconstruction chain and even reprocess from any stage on.

The user can write a C++ program using the classes and objects provided by CMSSW for the analysis tasks. This allows an unbiased analysis and leaves the freedom to the user to implement algorithms for any quantity which is to be examined. The format in which the output data is given, is that of the data analysis and visualization software framework ROOT [55]. With ROOT it is possible to plot, fit and process the data. The objects created by CMSSW for different chambers or runs can be evaluated at once, providing the ability to perform systematic studies.

6.2 Monte Carlo Simulation

Since version CMSSW_0_7_0, a cosmic muon Monte Carlo generator called CMSCGEN [56] is implemented in the software framework. The generator has been developed in the Physics Institute IIIA at the RWTH University. The parametrization of the cosmic muon flux is based on the one used for the generator for the LEP L3+Cosmics [57] experiment. The generator provides data of simulated cosmic muons arriving at the CMS detector at the surface of point SX5, as well as in the underground cavern. This simulated data allows a comparison with the real data taken by the CMS muon chambers for a scrutiny of the detector and software performance.

The simulated cosmic muon spectrum accounts for the dependence on the energy and the incident angle, in a precise parameterization, to obtain a realistic model of the cosmic muon spectrum, including the charge ratio and the absolute flux. Due to the uncertainty in the cosmic muons arrival time inside the 25 ns time window of the LHC clock cycle, the starting time of the muons are uniformly distributed between −12.5 ns and +12.5 ns. The simulation covers a momentum range from 2 GeV to 10 000 GeV. The simulated events are passed to the CMS detector simulation, which translates the particle properties into simulated detector response, producing a file, similar to files containing the cosmic data, as recorded by the DAQ.

Processing the simulated data the same way as the recorded cosmic data through the complete reconstruction chain, provides the ability to find potential problems in the reconstruction software. The simulation always gives access to the generated properties of each simulated muon, which can be compared with its reconstructed properties.

6.3 The Reconstruction Chain

The reconstruction of a muon track is performed in severals steps, starting with the raw data, channel per channel and ending with three dimensional chamber wide tracks. All steps are presented in the following chapter, a schematic chart of the reconstruction chain can be seen in figure 6.1.

6.3.1 Reconstructed Objects

Cosmic muons show a different event topology than particles from pp collisions. Particles produced in a pp collision originate from a central vertex. This information is used in their reconstruction, avoiding ambiguous tracks. Cosmic muons instead can reach the detector from all directions and with strong inclination. Due to this fact the reconstruction algorithm has to be modified, disabling any vertex constraint. Potential ambiguities are solved in later steps of the reconstruction.

Raw Data

The initial data for the offline reconstruction of cosmic muons with CMSSW is a continuous stream of data written into a file during the run. It consists of the raw TDC data, like the measured TDC times, TDC identifiers, but also status information of the TDC, like TDC errors. In the first step of the reconstruction an unpacker identifies events inside the data stream and separates all TDC information belonging to one event. Then each TDC measurement is mapped to a specific wire in the chamber by evaluating the internal TDC identifier and the TDC channel of the measurement. This information is stored in a so-called *Digi*.

Uncorrected Drift-Time

The Digi contains the unpacked, digitized data. In the case of drift tubes this is simply an uncorrected TDC time and the information in which channel this time has been recorded. This time is a sum of several components: first of all the drift-time of the secondary electrons, but also contributions from the trigger latency, the propagation time of the signal along the wire and an offset caused by the processing in the electronics and different cable lengths. For cosmic ray muons an additional uncertainty of the arrival time of the cosmic inside the 25 ns long TDC window has to be accounted for.

The propagation time along the wire gets corrected in the following reconstruction steps, when the position of the hit is known. The t_0 offset due to the cable lengths is corrected (6.3.2) using the delay times obtained in the test pulse runs (5.2.4).

Reconstructed Hits

In the next step of reconstruction the hit position is derived from the drift-time. CMSSW allows the use of different parametrizations for the time-to-drift-distance relation inside the drift cell. For the commissioning data a linear time-to-drift-distance parametrization with a constant drift-velocity of $v_{\text{drift}} = 54.3\,\mu\text{m/ns}$. is used:

$$x_{\text{hit}} = v_{\text{drift}} \cdot t_{\text{drift}} \tag{6.1}$$

This is a sufficient approximation for cosmic muons, which implies the simplifying assumption of a homogenous electrical field. More sophisticated parametrizations also take into account the incident angle of the muon, inhomogeneities of the electrical field in the cell and the outer magnetic field (which is zero for commissioning). Since these are relatively small effects of second order [58] for the commissioning data the linear time-to-drift-distance relation is of ample accuracy. Furthermore, in a later step of the reconstruction an additional event-based correction due to the uncertainty in the arrival time of the cosmic is performed, which additionally diminish effects resulting from the simplification of the time-to-drift-distance relation.

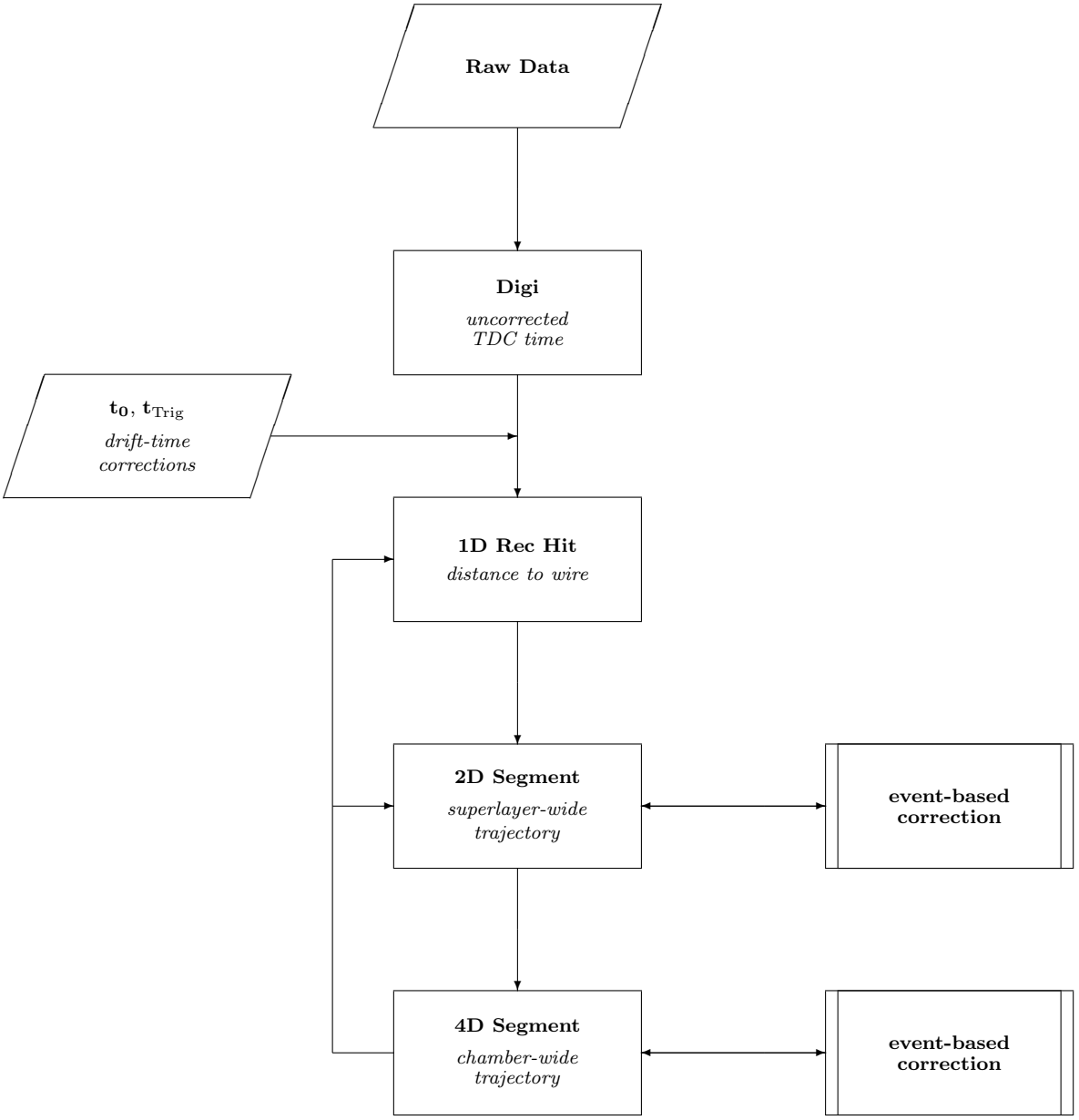

Figure 6.1: *Flow chart of the reconstruction chain.*

The position is stored in the container for reconstructed hits, the *1D RecHit*. In an initial step, the stored position is based on the plain drift-time and therefore contains only the one dimensional information about the distance of the hit to the wire, with a yet unsolved left/right ambiguity. In the following steps of the reconstruction the position is more precisely determined by combining hits to segments. This information is used to create updated copies of the 1D RecHit: First the left/right ambiguity is solved by a combinatorial pattern recognition, the incidence angle is determined and then the position of the hit along the wire is written in the updated 1D RecHit.

Superlayer Segments

In this step of reconstruction, sequences of 1D RecHits are formed to superlayer-wide tracks. Typically this superlayer-wide mini-tracks are composed of four hits, one hit in each layer with the hit cells adjacent to each other. But it may also happen that one cell missed a hit or that a noise hit occurs in the vicinity of the cells traversed by the muon. For these cases the pattern recognition identifies ensembles of candidates of hits belonging to one event. The appropriate combination of hits is chosen by a linear fit with a χ^2 minimization. The fit with the lowest χ^2 forms the superlayer-wide track which is stored in a container called *2D Segment*. The 2D Segment then contains the two dimensional projection of the muon track in the superlayer, including the fit parameters and updated copies of the 1D RecHits used for the fit. The projection of the muon's incident angle to the plane corresponding to the superlayers orientation (r-ϕ plane for Φ-superlayer and r-z plane for Θ-superlayer) is also stored in the 2D Segment. A segment cleaner algorithm deletes discarded segment candidates. Not in all cases the fitted track with the lowest χ^2 is matching the real track of the muon in the superlayer. The combination of hits can lead to ambiguities and in some cases the false fit has a lower χ^2 than the fit for the real track. Usually these false tracks are strongly inclined. Since the version CMSSW_0_9_x the segment cleaner offers for ambiguous tracks the choice to keep the track with lower χ^2, the one with the lower angle or both versions. This reco problem had been revealed in the analysis of the commissioning data due to an unexpected angular distribution of 2D Segments. A further description of this problem can be found in section 8.3.

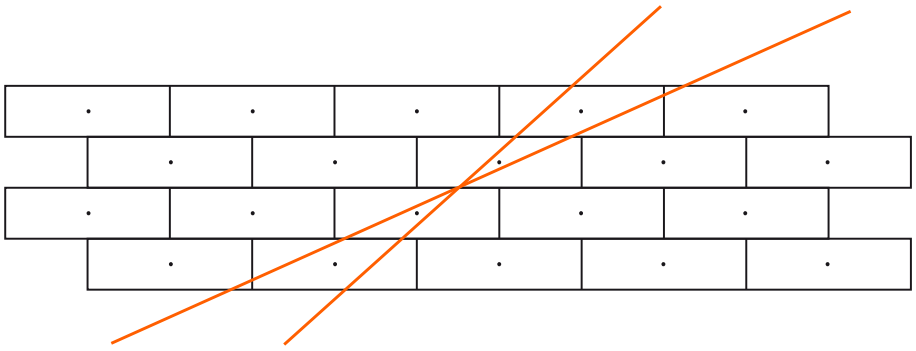

Figure 6.2: *Ambiguous segments. The plain drift-times in each cell are the same for both segment candidates drawn. The track with the lower χ^2 matches not necessarily the real muon path. This ambiguity can be solved at a higher reconstruction level.*

Chamber Segments

In the final step of the reconstruction the 2D Segments from both Φ-superlayers are combined to a *superphi segment*, which is subsequently combined with the 2D segment from the Θ-superlayer to obtain the three dimensional information about the muon track. For the superphi segment a new, additional track fit is performed using (in the ideal case) eight hits, four from each Φ-superlayer. The information concerning the Θ-superlayer is adopted unchanged. This final chamber-wide track is stored in a container called *4D Segment*. The name 4D results from the combination of two 2D Segments. In an ideal case a 4D Segment has been reconstructed out of 12 hits. Since the exact position of the hits is known now, the signal propagation time along the wire can be computed and an updated copy of the 1D RecHits is created. Potential ambiguities in 2D Segments from Φ-superlayers can be solved now and updated copies of them are also created. For the analysis of the commissioning data a selection on single 4D Segments has been applied.

6.3.2 Corrections to the Drift-Time

Several effects can cause an offset to the drift-time. Depending on the origin of the offset the correction is performed prior to data taking, after data taking or after reconstruction.

Individual Corrections of Cell Latencies

Since the cable length between front-end board and MiniCrate differs for each channel and the specific chamber types have minor differences in the arrangement of their electronic components, an intrinsic relative latency for every cell, has to be subtracted from the drift-time. This latency, typically in the range of ±10 ns, called t_0, is determined by test-pulse runs (5.2.4) for every cell. All latencies obtained here

are relative values, normalized to the mean value of the total latency. They are stored in an ASCII file for the use in ORCA. CMSSW needs to read this data from a SQLite database [59], but provides tools to convert ASCII data into a SQLite database with the required structure. For the LHC runs these data are migrated to an Oracle database [60]. The t_0 value is automatically subtracted from the Digi by CMSSW. The 1D RecHit contains the corrected drift-time.

Trigger-Latency Time Pedestal

The time pedestal referred to as *tTrig* represents the time recorded in the TDC for the absence of any drift, i.e. a drift-distance of zero. Several effects contribute to this offset of the drift-time: the major one is caused by the trigger latency of around 3.2 µs. Other contributions are caused by the time of flight of the muon, the signal propagation time along the anode wire and the latency due to the cable length from the cell to the MiniCrate. For the latter two only the average values are taken into account. The exact correction of the signal propagation time along the anode wire is done in the segment reconstruction, the relative timing differences among each channel are stored in the t_0 value. Due to that, the value of tTrig can be computed per superlayer since the single cells are synchronized.

The time pedestal is determined by identifying the beginning of the combined drift-time spectrum (7.1) from all cells of one superlayer and fit the rising edge with an integral of a Gaussian, as shown in figure 6.3. The tTrig value is computed by the mean of the fit $\langle t \rangle$ minus the width of the fit σ, whereas the width is weighted by an optimization factor obtained from residuals minimization, to account for the width of the rising edge k [61]:

$$t_{\text{Trig}} = \langle t \rangle - k \cdot \sigma \tag{6.2}$$

The tTrig latency is typically given with a precision of ±5 ns. Noisy channels can be masked in the calibration, since they would spoil the fit. A precise determination of the time pedestal is important for a good resolution of the muon chambers. The tTrig value is automatically subtracted from the Digi by CMSSW. The 1D RecHit contains the corrected drift-time.

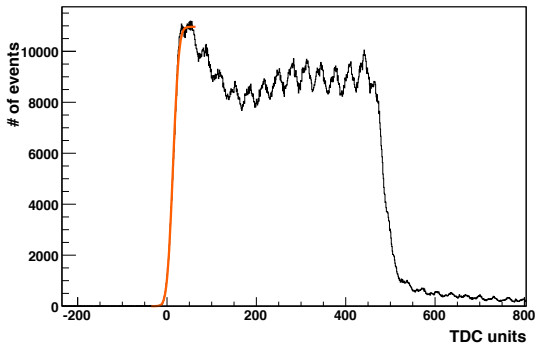

(a) *Drift-time spectrum with raising edge fitted with an integral of a Gaussian.*

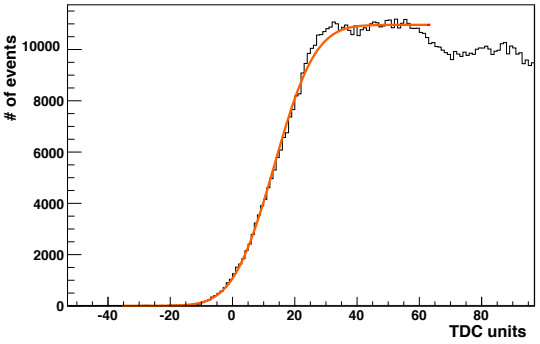

(b) *The raising edge of a drift-time spectrum and the fit with an integral of a Gaussian zoomed in.*

Figure 6.3: *Drift-time spectrum. The spectra have been normalized to tTrig to illustrate the accounting of the width $k \cdot \sigma$ of the rising edge.*

Event-Based Correction

The event-based correction adjusts the shift of the drift-time for each event independently. This can reduce the error in the time-to-drift-distance relation when the linear relation instead of the simulated parametrization is used, since the accuracy of the linear relation is depending on the distance of the hit to the wire. Another improvement is the correction of errors because of the change of the drift-velocity due to variations of the ambient pressure or due to fluctuations in the mixture of the gas. For cosmic muons, the dominating improvement is the is the correction of the error in the drift-time due to the uncertainty in the arrival time of the cosmic muon.

The external timing clock provides a 40 MHz signal representing the rate of one bunch crossing per 25 ns at LHC. The trigger evaluates the signals from the wire once per clock cycle. For LHC conditions this is sufficient, since events are expected once per bunch crossing. Cosmic muons cross the detector continuously and an uncertainty of the arrival time of the cosmic muon inside this 25 ns windows occurs. The drift-time spectrum is smeared by a 25 ns wide flat distribution. To minimize the impact of these effects, the event-based correction is performed. The shift of the drift-time is a priori not known, but after the reconstruction of the segments the obtained muon tracks can be refitted with adjusted parameters optimizing the muon tracks. The algorithm is minimizing the track residual (9.2), i.e. the distance between the position of the hit and the reconstructed track by adjusting the drift-time and the drift-velocity for each segment i, as follows [62]:

$$S = \sum_i (x_i - v_{\text{drift}} \cdot t_{i\ \text{drift}})^2 = \sum_i (x_i - (v_{0\ \text{drift}} + \delta v_{\text{drift}}) \cdot (t_{0\ i\ \text{drift}} + \delta t_{\text{drift}}))^2 \quad (6.3)$$

S is the square of the track residual and the value to be minimized, while x_i is the position of the reconstructed track in the ith cell, v_{drift} the adjusted drift-velocity, $v_{0\ \text{drift}} = 54.3\,\mu\text{m/ns}$ is the unchanged standard value of the drift-velocity and δv_{drift} the adjustment. $t_{i\ \text{drift}}$ is the corrected drift-time in the ith cell, the recorded drift-time is $t_{0\ i\ \text{drift}}$ and the change of the drift-time δt_{drift}. Four parameters, the two dimensional spatial information of the new track direction, δt_{drift} and δv_{drift} are determined in a way as to minimize S by solving a system of four linear equations, given at least five hits are contributing to one superphi segment. For segments of the Θ-superlayer with a maximum four hits, only three parameters are fitted, setting $\delta v_{\text{drift}} = 0$.

Accounting all corrections to the drift-time the measured value is corrected as follows:

$$t_{\text{drift}} = t_{\text{measured}} - t_0 - t_{\text{Trig}} - \delta t_{\text{drift}} \tag{6.4}$$

The 1D RecHits are updated incorporating the optimized values for the drift-time and the drift-velocity. Then the segments are recomputed, but the error of the segments is not updated with respect to the changes due to the event-based correction. Later versions of CMSSW may rectify this.

7 Chamber Operation

The goal of taking cosmic ray data in the chamber commissioning period is to verify the chamber performance, study the reconstruction algorithms and identify inefficient cells or other problems. Although tested before at the production sites, all chambers are under scrutiny after their installation at the final position in the CMS return yoke. The data used in the following analysis has been taken in the chamber commissioning (5.2). This implies that only single chambers were readout, and the muons were triggered by a dedicated standalone autotrigger (5.2.3).

One wheel of the CMS barrel yoke is divided into twelve sectors, as seen in figure 7.1, equipped with chambers in four stations, as described in section 3.7. Aside from chambers in station MB4, where the size differs between individual chambers, all chambers per station are equal and interchangeable. Consequently, a priori all chambers of one type are expected to behave similarly. By mounting the chambers in the barrel yoke they obtain an inclination in ϕ, individual for each chamber per wheel. But the chambers are designed for LHC conditions, where the muons come from the interaction point in the center of the detector and strike the chambers coming from a direction distributed around the perpendicular to the chamber surface. Cosmic ray muons instead hit the detector coming from the zenith and are distributed $\propto \cos^2 \alpha$ as described in section 5.1. In the following analysis one of the foci are set on the systematic comparison of the data from different sectors inside one wheel and station, to study the reconstruction of inclined muons and to identify outlying values from chambers with potential problems. Systematic effects due to the different inclinations of the chambers are explained.

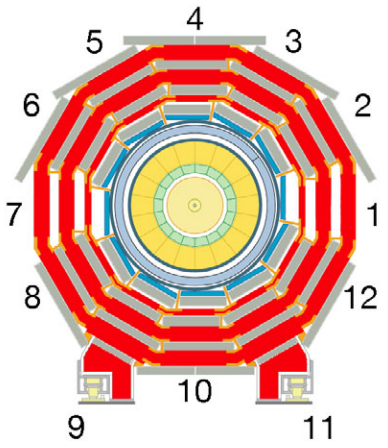

Figure 7.1: *DT sectors. View from the +z side.*

For the study of these effects a symmetry can be utilized. Two opposing chambers should underlie the same effects of inclination and so do chambers mounted with the same inclination, but in different directions. The angle between the perpendicular to two adjacent chambers is 30° and thus effects of sector inclination can be shown

using just three chambers, instead of all ten[1], as long as shielding effects or the muon flux are not important.

The period of the chamber commissioning was a time of continuous working on all subdetectors. Due to this the wheels were often moved, changing the shielding conditions. Most time the barrel yoke wheels were open on both sides, i.e. there was a gap between the wheel with the commissioned chamber and the neighboring wheel. The distances between the wheels were given by the requirements of the proceeding works. The HCAL Barrel (HB) and the solenoid were already mounted inside the wheel YB0, providing additional shielding for chambers in this wheel. This special circumstances for data taking exist only during the commissioning and will not occur in LHC conditions.

The most basic part of the data analysis is to look at the time-boxes and occupancies. These plots are based on data of an early step in the chain of muon tracks reconstruction, only 1D RecHits are needed. The trigger selection has been applied, but yet no track reconstruction algorithm. As basic plots they are powerful indicators to see if the chamber hardware works accurately, without the influence of potential errors of the track reconstruction software. Due to the application of the trigger selection, geometrical effects can already be seen in this step of the reconstruction chain.

7.1 Time-boxes and TDC spectra

7.1.1 The CMS DT cell drift-time spectrum

The *TDC spectrum* is the histogram of arrival times of drift electrons at the anode wire, measured in TDC units, as recorded by the TDC. The drift-time spectrum plotted in ns is referred to as *time-box*. Since the relation between TDC units and time (4.3) - one TDC unit is $^{25}/_{32}$ ns long - is linear and fixed, the information contained in both histograms, the TDC spectrum and the time-box is the same, just the scale is different. Oftentimes the TDC spectrum is normalized to t_{Trig}, to let the spectrum start at 0.

The drift-time varies from zero, for the case that the muon passed the drift cell at the anode wire, up to the maximum value t_{max} for the case that the muon passed near the cathode. t_{max} is the drift-time for half of the cell width, since the distance from the cathode to the wire is half the cell width. A typical time-box is shown in figure 7.3 for better statistics the time-boxes of all cells from one superlayer are added up here. An unnormalized TDC spectrum from a different chamber is shown in figure 7.2 (note the different units at the x axis).

[1]Remember that the upright chambers in sector S1 and sector S7 were not mounted during the chamber commissioning. See section 3.7.

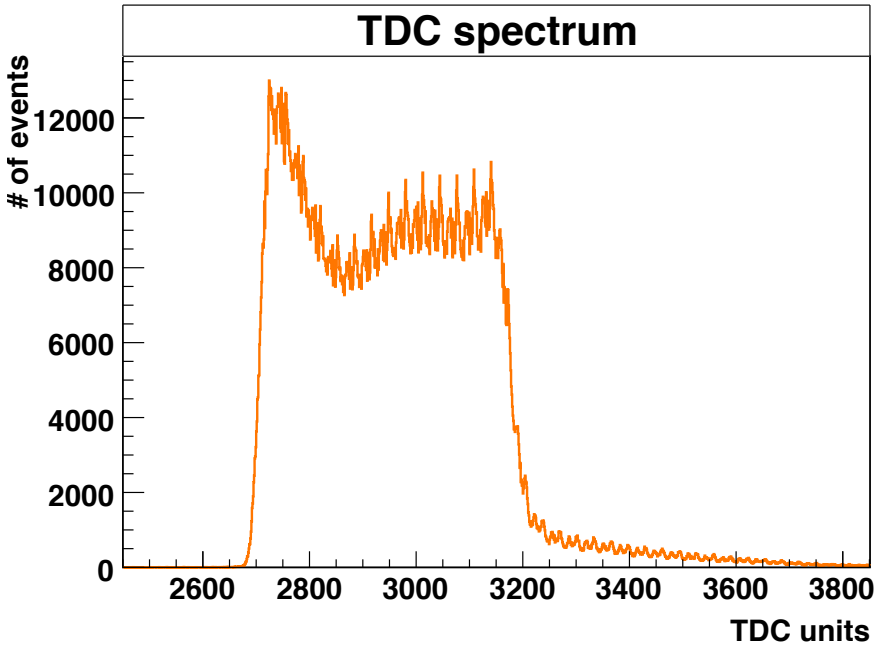

Figure 7.2: *TDC-spectrum, added up for all cells in one superlayer.*

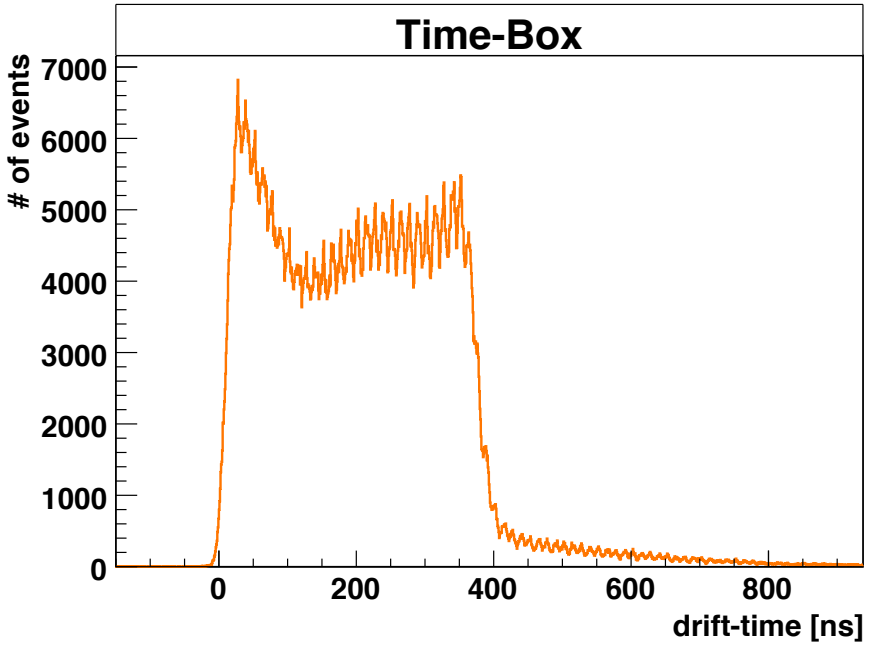

Figure 7.3: *Time-Box, the drift-time spectrum in* ns *added up for all cells in one superlayer.*

The maximum time, the electrons drift in the cell is

$$t_{\max} = \frac{x_{\max}}{v_{\text{drift}}} = \frac{20.9\,\text{mm}}{54.3\,\mu\text{m/ns}} \approx 380\,\text{ns} \quad . \tag{7.1}$$

It is the time the electron needs to drift the maximum distance $x_{\max}$ from the cathode to the wire. But due to the uncertainty of the arrival time of the cosmic ray muons inside the 25 ns windows of the TDC, for cosmic muons the spectrum is smeared and the measured maximum drift-time can be up to $t_{max} = 405$ ns. Since the TDC spectrum is plotted using 1D RecHits, the signals travel-time along the wire is already corrected by CMSSW.

In the vicinity of the wire the electric field is very strong, and consequently the drift-velocity is higher than in the other regions of the cell. Thus the drift-time spectrum peaks for short drift-times. A constant drift-velocity would result in a square-shaped time-box. Therefore, the assumption of a constant drift-velocity is not absolutely correct, but for cosmic muons the errors due to this are negligible, compared to the uncertainties in the arrival time of the cosmic muons.

Due to the gas amplification in the vicinity of the wire, photons are produced by annihilation of electrons and positrons. If these photons hit the cathode, secondary electrons are emitted. These electrons drift to the anode wire and cause a signal, which is responsible for the tail in the drift-time spectrum. These signals are called *afterpulses*.

The jitter in the shape of the time-box is an aliasing effect due to the 40 MHz sampling rate of the TDC.

7.1.2 Performance checks with Time-Boxes

As seen in figure 4.5 each drift cell has three electrodes (anode wire, cathode and strip) which should be powered correctly. Obviously a cell lacking the anode wire cannot provide a signal, but if one of the other two electrodes is not correctly powered, the cell will function partially, manifested in a distorted spectrum. For example if one field strip is missing or out of function, the electrons in the outer area, near the cathode are attracted by the other, working field strip. Hence only electrons near the anode wire are able to reach the wire and produce a signal. This results in a shorter drift-time spectrum.

For the case that one cathode is out of function, the electric field can not be held up to the outer regions of the cell, since the cathode is at zero and not at -1200 V. Hence the drift-time for electrons crossing the cell near the defect cathode is longer, which spreads the drift-time spectrum to longer drift-times. This leads to a smoother end of the drift-time spectrum; for longer drift-times there are less entries, the missing events are in the tail of the spectrum. This is superimposed by the correct spectrum from the other side of the cell with a working cathode. A typical distribution for that case is shown in figure 7.4. A detailed description of the distortion of time-boxes due to defect electrodes can be found in [45].

During chamber commissioning a few chambers showed such problems. Either caused by the high voltage distribution box (junction box), the input to the chamber or the power supply.

The shape of the drift-time spectrum can also help to identify problems with the gas. An air filled chamber would provide almost no triggers, and thus no data. If a chamber is not flushed with the right gas mixture or the gas is contaminated with air, the measured spectra are distorted. Figure 7.5 shows the drift-time spectrum added up for all cells of one superlayer for a chamber with a problem in the gas connection. Due to a non airtight connection the gas was contaminated. Since both, oxygen and nitrogen are electronegative, a high fraction of drift electrons are captured before reaching the anode wire, resulting in a decrease of registered signals for increasing drift-distances.

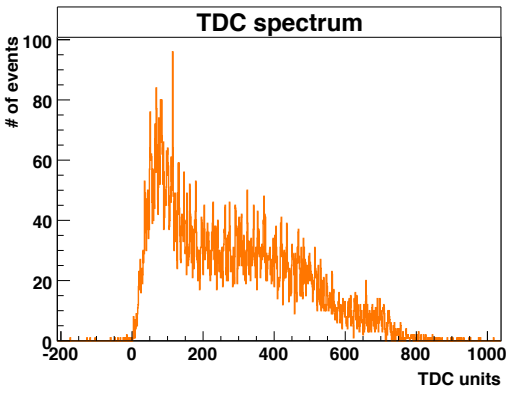

Figure 7.4: *TDC spectrum for a cell with a missing cathode, normalized to* t_{Trig}.

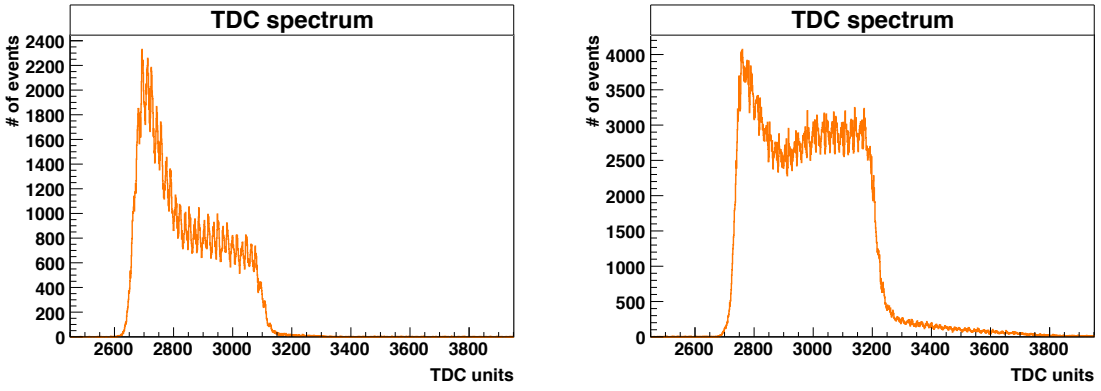

(a) *TDC spectrum of a superlayer filled with gas, contaminated by air.*

(b) *TDC spectrum of the same superlayer after three days of correct gas flow.*

Figure 7.5: *Influence of air contamination on the shape of the TDC spectrum*

In the data quality check (5.2.5), performed directly after data taking, an automated test of the ratio of number of events between the begin and the center of the drift-time spectrum (*head to belly ratio*) and the ratio of number of events between the center and the end of the spectrum (*tail to belly ratio*) is performed to directly identify such problems.

7.2 Occupancy distributions

7.2.1 Distribution of Reconstructed Hits

A superlayer has about 600-800 cells; when taking data, each provides a unique time box. For a short view on each cell this is way too much. A quick overview about all cells operation is provided by the *occupancy*. It is the histogram of the triggered hits (6.3.1) per wire. For each triggered hit, there is one entry in the bin corresponding to the cell in which the signal was measured. Due to the trigger correlation between the two Φ-superlayers, the occupancy for a Φ-superlayer underlies different effects than the occupancy distribution from a Θ-superlayer. A typical occupancy for a Φ-superlayer is shown in figure 7.6, where all four layers of a superlayer are added up.

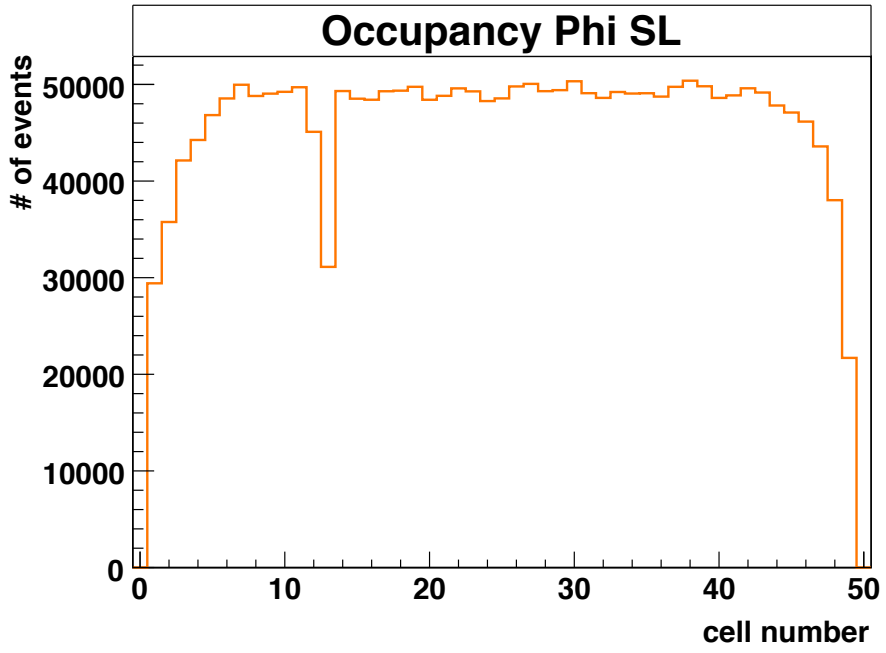

Figure 7.6: *Occupancy of a horizontal Φ_2-superlayer (all four layers added up). The drop in channel 13 is due to a dead cell in one of the four layers. At the edges, the number of entries decreases, due to an effect of geometrical acceptance.*

The rise and fall at the edges of the occupancy for a Φ-superlayer is an effect of geometrical acceptance due to the shift in the relative position in-between the two Φ-superlayers. Naturally the illumination of the chamber at the edges is as good as in the center, but not all tracks crossing the chambers edges fulfill the trigger conditions, resulting in a drop of the number of triggered events for cells lying at the superlayers edges.

If for example a moderately inclined track hits the upper Φ-superlayer, but not the lower, the event does not get triggered, as indicated by the red line in figure

7.7(a). Consequently the occupancy is steeper on one side of a Φ-superlayer and less steep on the opposite side.

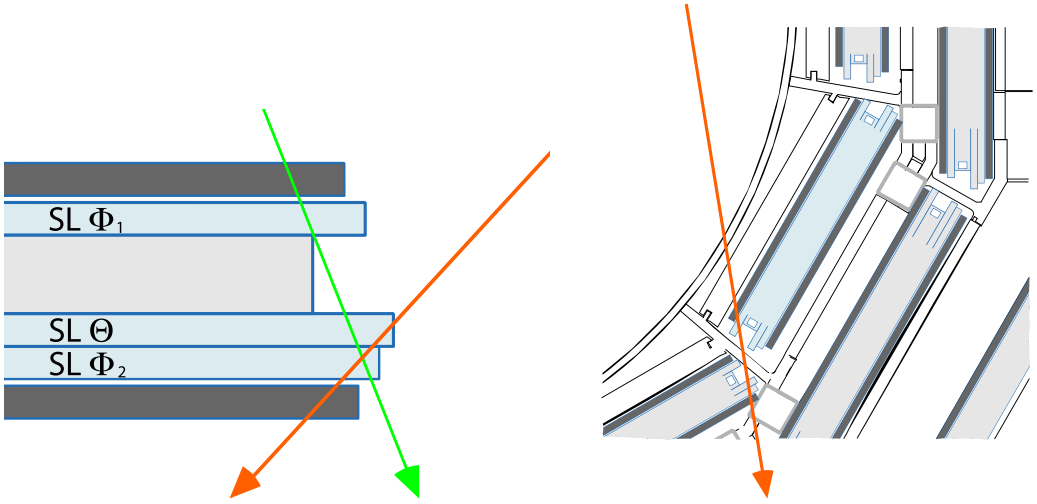

(a) *This detail from a chamber's edge shows how both Φ-superlayers are positioned against each other. The muon track indicated by the red line does not fulfill the trigger conditions, the track indicated by the green line does.*

(b) *This detail from a wheel shows a slightly inclined muon track hitting a chamber in sector S12, inclined by* 60°, *which does not fulfill the trigger conditions.*[2]

Figure 7.7: *Geometrical acceptance.*

7.2.2 Sector Comparison

Geometrical Acceptance and Sector Inclination

The geometrical acceptance varies with the inclination of the chamber. With increasing inclination the rise of the occupancy near the edges is less steep on one side and steeper on the other. Figure 7.8(a) shows the occupancy for the Φ_2-superlayer for three adjacent sectors: sector S10 with no inclination, sector S11, with 30° inclination and sector S12, which is inclined by 60°. Besides the geometrical acceptance, another effect can be seen in the occupancy of an inclined chamber. A pattern of a minimal rise and fall, repeated every four cells occurs in these chambers. This is is an effect due to the trigger correlation between both Φ-superlayers by the TRACO (4.3) and does not occur in the Θ-superlayer.

[2] Although this track does not fulfill the trigger conditions for the chambers in sector S11 and sector S12 in station MB1 it would fully hit a chamber in another station and thus not missed if all chambers were read out.

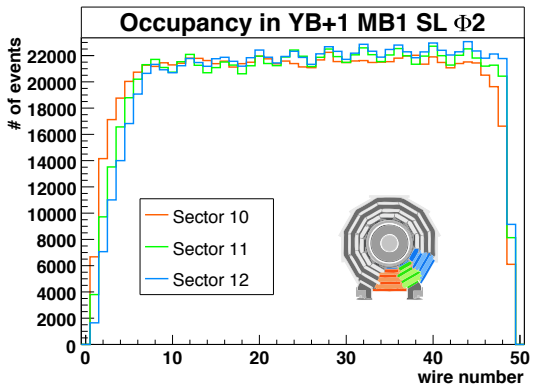

(a) *Occupancy for sector S10, S11 and S12 of MB1 chambers in YB+1 for the Φ_2-superlayer. With increasing inclination the rise of the occupancy near the edges is less steep on one side and steeper on the other.*

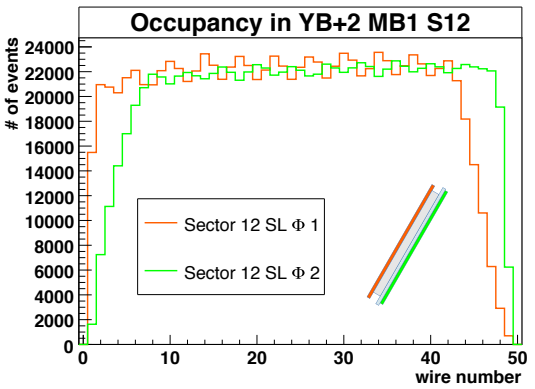

(b) *Occupancy for the Φ_1- and Φ_2-superlayer in sector S12. The effect of the geometrical acceptance is mirrored for the two Φ-superlayers of one chamber. The small sketch inside the plot shows the two Φ-superlayers in their right position and angle. The high wire numbers are on the lower left side.*

Figure 7.8: *Geometrical acceptance of inclined chambers*

In figure 7.7(b) a detail of the CMS barrel yoke in sector S12 can be seen. The chamber is inclined by 60° and the position of the superlayers inside the chamber is shown. A slightly inclined muon track is drawn as example. The track hits the edge of the Φ_1-superlayer, but not the Φ_2-superlayer and therefore does not fulfill the trigger conditions. Let α be the angle between the path of a cosmic muon and the zenith. The more a chamber is inclined, the lower is the angle α, for which cosmic ray muons are not hitting both Φ-superlayers, if they pass the chamber near the superlayers edges. On the other edge of the superlayer nearly every track traverses also the other superlayer, only strongly inclined tracks do not hit the other superlayer. Therefore the effect of geometrical acceptance is intensified for inclined chambers.

The geometrical acceptance follows a symmetry in-between the different chamber inclinations. The occupancy of chambers with an inclination of 30° (60°) show the same shape like the one from the opposing chambers with an inclination of 210° (240°). The chambers inclined by 120° (150°) show a mirrored pattern, viz the effect of geometrical acceptance turns up on the other end of the superlayer, and so do their opposing chambers at 300° (330°). In respect to the position and the wheel, the chambers are mounted with positive oder negative orientation, a negatively orientated chamber shows an additional swap of the effect in respect to a positive chamber. Between the two Φ-superlayers inside one chamber the effect is also mirrored. The steep side of one Φ-superlayer is the side with less entries for the other Φ-superlayer and vice versa, as shown in figure 7.8(b) for sector S12. This

behavior can be understood from figure 7.7(b). For cosmic muons originating from a symmetric distribution around the zenith, muons passing the inner superlayer at the right end nearly always hit the outer, and muons passing the outer superlayer at the left end, mostly hit also the inner one.

For a Θ-superlayer the situation is different. A smaller effect of geometrical acceptance can be seen for the wires near the superlayer edges. Depending on the trigger type (5.2.3) no hits or just uncorrelated hits are required in the Θ-superlayer. Moderately inclined tracks passing a Φ-superlayer near the front end side may not hit the outer cells of the Θ-superlayer, resulting in less triggered hits in these cells. The slope is symmetric between both ends of a Θ-superlayer, without an angular dependence. A typical distribution can be seen in figure 7.9(a).

The Monte Carlo simulation CMSCGEN (6.2) for comics muons in CMS does not contain a full trigger simulation, but a modeled simulation of the trigger efficiency. The modeling affects only the angular acceptance of a complete chamber, but not single cells, so no effect of geometrical acceptance can be seen in the occupancy of Monte Carlo simulated events. Figure 7.9(b) shows the occupancy of a Φ_2-superlayer with Monte Carlo generated cosmic data. The hits are equally distributed over the whole superlayer.

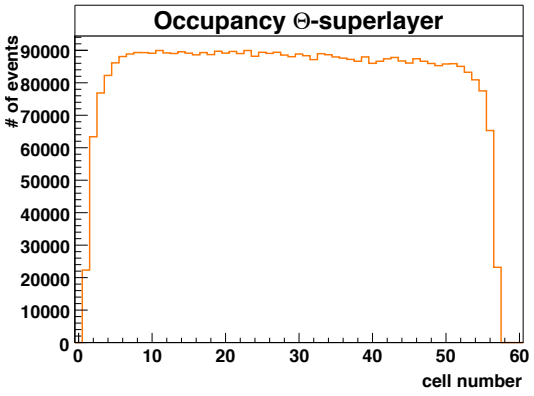

(a) *Occupancy Θ-superlayer (all four layers added up)*

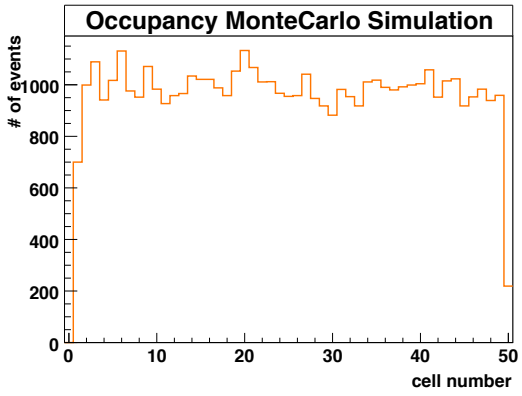

(b) *Occupancy of Monte Carlo simulated events. The trigger has not been modeled in this simulation, consequently no geometric acceptance effects can be seen. The uneven steps in the distribution are due to the low statistics.*

Figure 7.9: *Geometrical acceptance*

7.2.3 Shielding

The occupancy of the Θ-superlayer shows a different shape for some chambers, especially in the sectors S2 to S6. The number of entries increases for the channels at both ends of the superlayer. This is an effect due to the conditions during data

taking. As pointed out in the beginning of the chapter, the wheels were standing separately usually with a gap in-between, although these conditions were a subject of constant change. Since the wires from the Θ-superlayer run parallel to the gap between two wheels and perpendicular to the beam line, the wires at the edges of the Θ-superlayer are directly exposed to muons, without being shielded by the iron of the return yoke, depending on the muon's direction. This leads to the higher occupancy for the outer cells, if the wheels are not closed. Figure 7.10(a) shows the occupancy of the Θ-superlayer in wheel YB+1 for four sectors. The two upper chambers in sector S3 and S5 have similar occupancies and so have the lower in sector S9 and S11. Whereas the occupancies distributions in the upper sectors shows the effect of more entries at the edges. At the time of data taking the neighboring wheels YB+2 and YB0 were standing just a few meters next to YB0. Thus muons were able to cross the gap between the wheels and hit the outer wires of the chambers in sector S3 and S5. The edges of the chambers in sector S9 and S11 were shielded by the neighboring wheels, resulting in a constant shielding over the whole length of the superlayer.

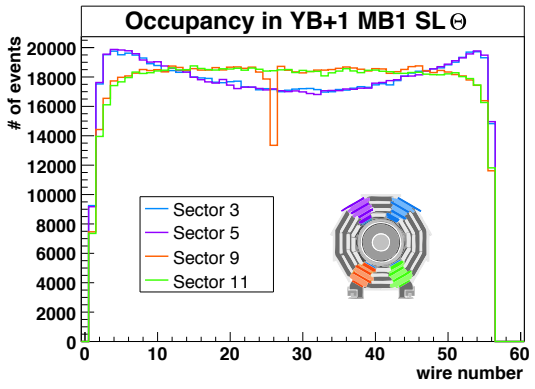

(a) *Occupancy Theta for different inclinations. The drop in the distribution of sector 9 is due to a dead channel at wire 26.*

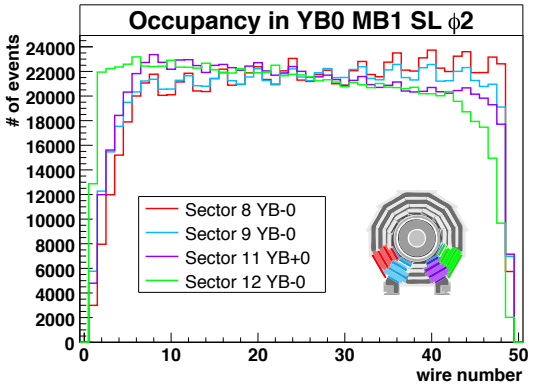

(b) *Occupancy Phi*

Figure 7.10: *Shielding effects in the occupancy distributions.*

The comparison of data from the same sector and station but different wheels shows the stability in the chamber quality. One would expect similar distributions, since effects of the inclination or shielding by the return yoke of the wheel are the same for chambers in the same position. Nevertheless shielding effects have a high impact on the variation of the data distribution between the same chambers in different wheels, since the data taking took part in a period of heavy working in the assembly hall SX5. The wheels have been moved often, and sometimes the chambers have been shielded by another wheel standing directly next to them, sometimes there was enough distance between the wheels, that no remarkable shielding occured at

all. The barrel of the hadronic calorimeter has been mounted inside wheel 0, while commissioning of the muon barrel chambers took place. With its high density, the calorimeter shields the soft part of the cosmic ray muon spectrum. These shielding effects can be seen best in the occupancies.

Figure 7.10(b) shows the occupancy in the Φ_2-superlayer for four chambers of wheel YB0. In the plot a superposition of two effects can be seen. First due to the orientation of the chamber inside the wheel: The chambers in S8, S9, S12 are mounted on the negative side of YB0, the chamber in S11 is mounted on the positive side of the wheel, viz. the orientation of the chamber in sector S11 - in respect to the other chambers - is rotated by 180° around the z-axis of the local chamber coordinate system (4.2.1). For chambers with the same orientation the effect of geometrical acceptance would be mirrored for sector S8 and S12 as well for sector S9 and S11. But since sector S11 has a different chamber orientation, the shape of the occupancy has the steep fall-off at the same side as sector S8 and S9. The second effect is a shielding effect, due to the HCAL Barrel (HB), which was already mounted in YB0 during data taking. Over the range of all channels, the occupancy shows a continuous decrease of events. For sector S8 and S9 from the high to the low wire numbers and for sector S11 and S12 from the low to the high wire numbers. Being minimum 5.8 interaction lengths thick, the HB shields the soft part of the cosmic ray muon spectrum.

7.2.4 Performance Checks with the Occupancy

The occupancy plot is the ideal tool to identify dead or noisy cells at a glance. In the example of figure 7.9(a) it is easy to identify that cell number 13 has less entries. This is a clear indicator for one of the layers having a dead channel 13. During chamber construction a small number of dead cells $<<$ 1% was unavoidable. The first channel of layer 4 normally has no wire, since the space where normally an I-beam is placed is needed for the superlayer frame (C profile). A few more dead cells were observed in the commissioning. Some of them could be traced with the help of testpulses to broken front end channels and were repaired by replacing the front end board. Apparently no wire broke, since no short circuits in the high voltage were observed.

Another issue which can be easily found with the help of the occupancy plot is a wrong configuration of the trigger. The trigger configuration (5.2.3) depends on the chamber orientation (4.2.1), because the shift between the superlayers is different for left- and right-orientated chambers. If the chamber has been configured with the wrong orientation the illumination with triggered events is not uniform anymore. The occupancy shows a strong pattern of rise and fall, repeated every four cells as shown in figure 7.11. This effect is particularly apparent in the HH+HL trigger configuration, which is the standard trigger for MB4 chambers.

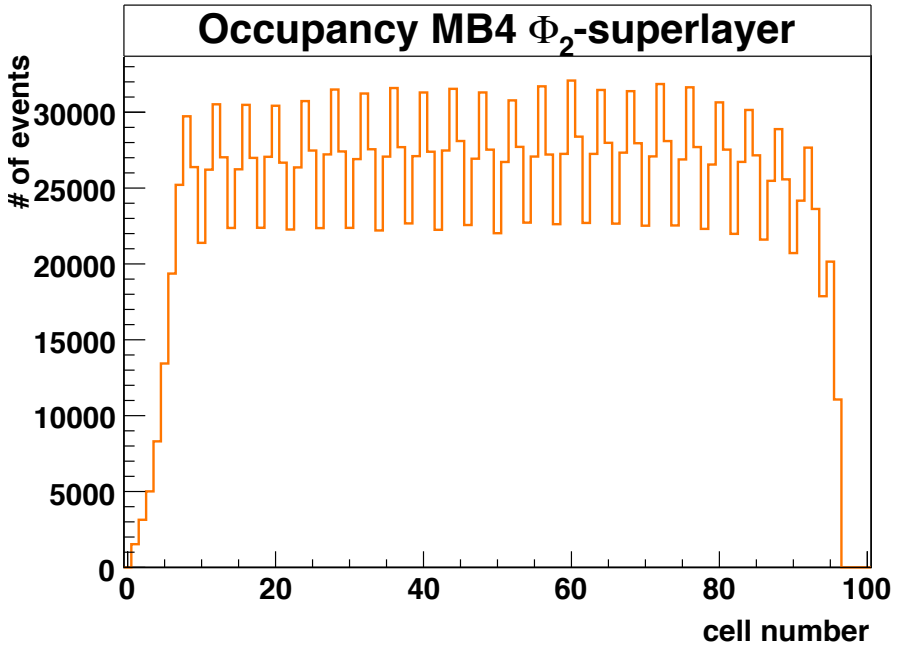

Figure 7.11: *Occupancy of chamber with wrong trigger configuration. A right orientated chamber was mistakenly taken to be a left one.*

7.3 Noise

A muon ionizing the gas should be the only source for a signal detected by the drift tube chamber. Any unwanted signal, produced by other effects is noise. Possible reasons for noise hits are a signal injection from the high voltage cabling, by the low voltage power supply or can result by outer factors, like moving the crane in the CMS assembly hall or work at other subdetectors at the time of data taking. Noise signals can occur due to an ionization in the gas which is not caused by muons, or may be induced in the electronics of the chamber.

To identify noisy channels, the fact that signal hits only occur inside the time-box (7.1) can be utilized. Noise hits appear at any time but signal hits are expected only between $t = 0$ and $t = t_{\max}$. Each hit, recorded when the TDC window is open, but outside the time-box is regarded as noise. TDC spectra with noise hits are shown in figure 7.12. By plotting the occupancy only for events outside of the time-box, an easy identification of noisy cells is possible, since only a few background events are expected before the time-box for a non-noisy cell. Figure 7.13(a) shows the occupancy for events occurring before the time-box. Noisy channels also appear clearly in the occupancy plot for all hits (in- and outside of the time-box), since noise leads to a considerably higher occupancy, peaking out of the uniform distribution, as seen in figure 7.13(b).

Once identified, eventually the noisy cell can be fixed, if not it is possible to exclude a too noisy cell from the analysis, but during commissioning this was never necessary. A cell showing constant noise can be masked by the on-chamber electronics.

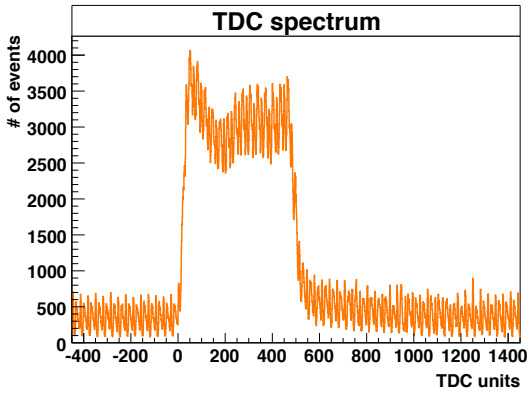

(a) *TDC spectrum added up for all cells of one layer. A continuous noise background superimposes the drift-time spectrum. Only single channels in this layer are noisy.*

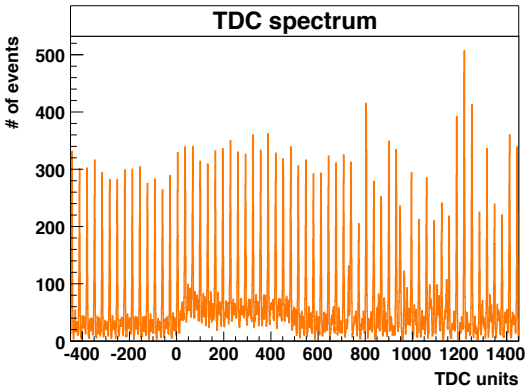

(b) *Noisy TDC spectrum for a single channel. The number of events for the noise peaks exceed the drift-time spectrum, which can be seen between* 0 *and* 500 TDC units.

Figure 7.12: *TDC spectra with noise.*

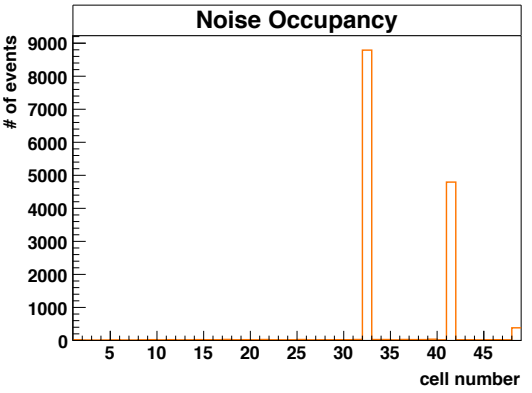

(a) *Occupancy of noise hits. Only hits before the drift-time spectrum are regarded, showing only noisy cells.*

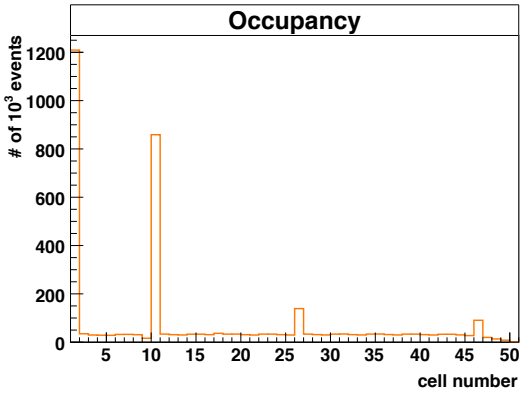

(b) *Occupancy with noise hits. The normal occupancy distribution with about* $50 \cdot 10^3$ *events is superimposed by the hits from four noisy cells with up to* $1200 \cdot 10^3$ events.

Figure 7.13: *Occupancy distributions showing noise.*

If noise hits occur inside the time-box, or even close to a hit, it can disturb the track reconstruction (6.3.1) algorithms. But most of the noise as seen in the commissioning occurred in single channels and thus did not affect the track reconstruction in a

substantial way. In this step of the commissioning less than 0.015% of the cells of all MB1 chambers showed noise peaks in the occupancy with 20% more events than the uniform distribution. More than half of the cells showing noise were in cells at the layer's edge.

Another technique to quantify noise is to take data with a random trigger. The gate of the TDC is opened for a constant time, typically several μs at a randomly chosen moment. Noise is expected to appear at any time, whereas the contribution by muons crossing the chamber during the time of the open gate is negligible. The number of noise hits per gate width gives the noise rate in Hz. The amount of noise increases after final cabling, since all power supply cables - for high-voltage and low-voltage - are fixed on the chambers and at the return yoke, instead of single cables hanging loose as it was the case during the commissioning phase. Random trigger noise data has been recorded after final cabling. A typical cell shows a background noise of about 10 Hz, above a noise rate of 40 Hz a cell is regarded as noisy. The average noise rate of noisy cells is about 1000 Hz, while cells showing strong noise can reach noise rates of 100 kHz and above. The fraction of noisy cells, as measured with random trigger is about 0.025%.

8 Chamber Functionality

8.1 Cell Latency

The individual cell latency offset t_0 (6.3.2), measured with test pulses (5.2.4) is in a range of about $\Delta t = \pm 10\,\text{ns}$. A typical distribution of latency offsets per wire is shown in figure 8.1. The latency values are split into groups of 16 wires, with a spread of the t_0 value of about $\pm 1\,\text{ns}$, corresponding to the 16 channels of one front end board (4.3). In-between the front end boards (FEBs) the t_0 values differ by about 4 ns due to the individual lengths of each FEBs cable connection. The cables used for the injection of the test pulses have themselves an intrinsic latency superimposing the individual cell latency [63]. The t_0 value is determined for all cells. The total latency for a cell is the sum of the mean latency tTrig (6.3.2) and the individual cell latency t_0.

$$t_{\text{latency}} = t_0 + t_{\text{Trig}} \tag{8.1}$$

Cells in a Φ-superlayer usually have a negative t_0 offset, cells in a Θ-superlayer a positive one.

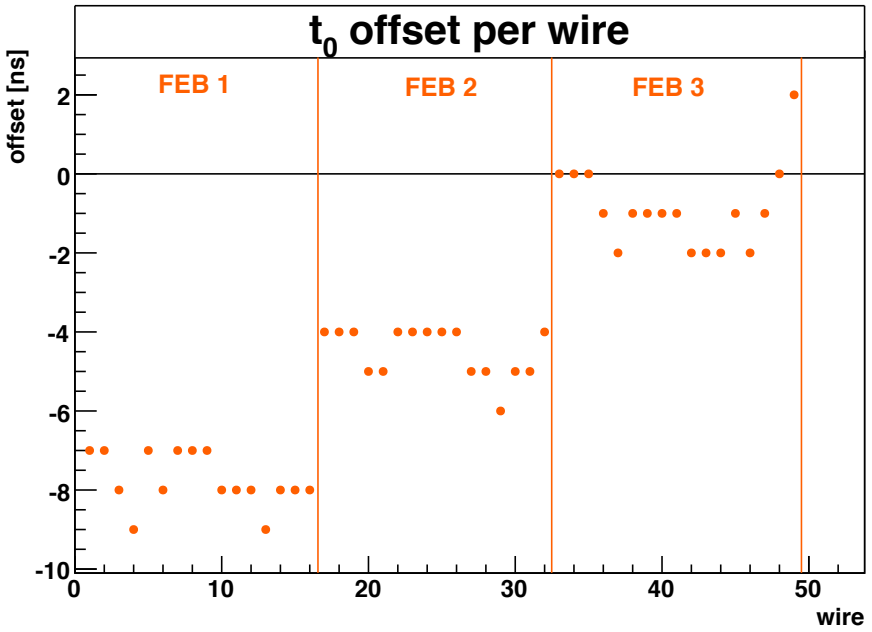

Figure 8.1: *t_0 latency for all channels of one layer in a Φ-superlayer*

8.2 Number of Hits per Segment

The number of hits used to built a segment is a helpful quantity to estimate the efficiency as well as to find problems with the geometry. In an ideal case a superphi segment is built of eight hits and a theta segments of four hits. Consequently a complete 4D Segment is built of 12 hits. Figure 8.2(a) shows a typical plot for superphi segments and figure 8.2(b) one for theta segments. In each plot the number of hits per segment for cosmic muon data and for Monte Carlo simulated (6.2) events are shown.

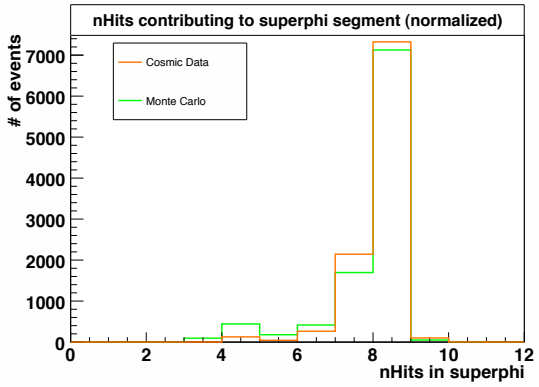

(a) *Number of hits contributing to a superphi segment*

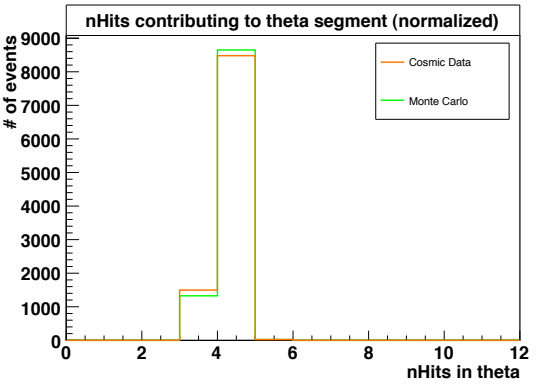

(b) *Number of hits contributing to a theta segment*

Figure 8.2: *Number of hits contributing to a segment.*

The Monte Carlo simulated data and the cosmic muon data mainly coincide. The simulated data has about 4.5% less superphi segments built out of seven hits and about 3.5% more superphi segments built out of only four hits. The number of hits contributing to a 4D Segment may deviate from the ideal case, if the muon traversed the cathode or passed an inefficient cell. Then the segment is built using less hits. It is also possible, but rare, that secondary hits from afterpulses or noise hits get taken into account for the segment building process, leading to segments with too many hits. About 1% of the 4D Segments have more hits than in the ideal case. Using a wrong geometry for analyzing the chamber has direct bearing on the

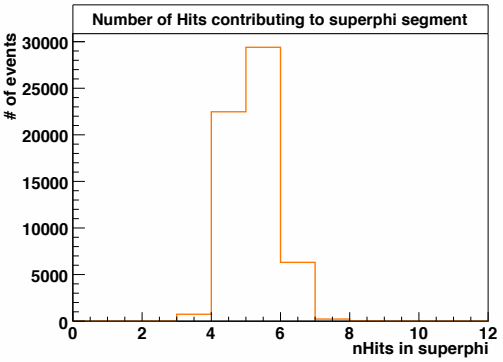

Figure 8.3: *Number of hits for segments, built with a wrong geometry database mapping.*

number of hits used to build a 4D Segment. The segment algorithm finds a 2D Segment in the upper and one in the lower Φ-superlayer, but since for different chamber types the staggering between the superlayers is different it is not possible to build one superphi segment if the algorithm assumes another geometry. The superphi segments are then built with four or five, instead of eight hits. An example for this can be seen in figure 8.3, showing superphi segments from chamber YB-1 MB4 S3. Up to the version CMSSW_1_4_0 a wrong geometry was used by CMSSW causing the reconstruction of superphi segments to fail. This bug was found by analyzing cosmic muon data.

Since the reconstruction algorithms are optimized for muons from the pp collision interaction point, inclined tracks are less often built out of eight hits than tracks perpendicular to the chamber. The effect of a cut on tracks with an inclination angle of $\varphi < 10°$ can be seen in figure 8.4(a), where φ is the angle between the path of a cosmic muon and the normal to the chamber measured in local chamber coordinates (4.2.1). The fraction of superphi segments built out of eight hits is about 20% higher than for the full angular spectrum. Thus the inclination of the chamber does only have a marginal effect on the number of hits per segment, but the normally the number of hits per segment is dominated by the fluctuation of parameters like gas quality, drift-time correction or noise.

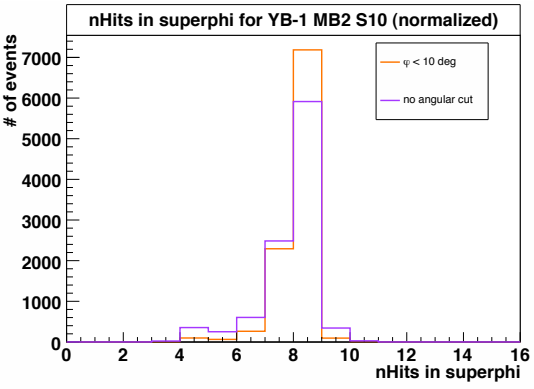

(a) *Number of hits contributing to a superphi segment with and without an angular cut on* $\varphi < 10°$.

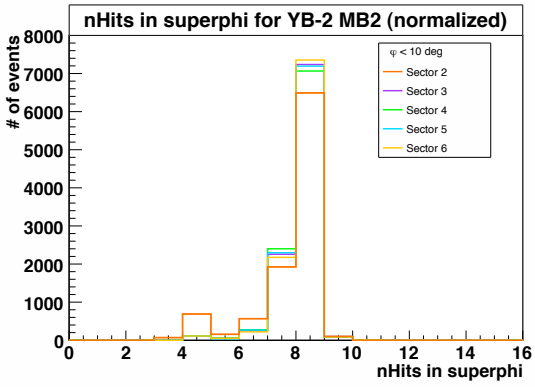

(b) *Number of hits in superphi segment for different sectors. An angular cut on* $\varphi < 10°$ *has been applied.*

Figure 8.4: *Angular dependence of the number of hits per superphi segment.*

8.3 Angular Distribution

The angular distribution of reconstructed tracks is affected by several factors. First of all there is the angular distribution of the cosmic ray muons. As pointed out in section 5.1 cosmic ray muons are distributed $\frac{dN}{d\cos\alpha} \propto \cos^2\alpha$. This distribution is

modulated by the angular acceptance of the trigger. Up to $\varphi = \pm 35°$ the trigger acceptance is flat, and then decreases to about 50% around $\varphi = \pm 60°$ as shown in figure 4.10. The incident angle of the muon track is measured in the r-ϕ plane[1] by the Φ-superlayers and in the r-z plane by the Θ-superlayer. Since there are two Φ-superlayers, but just one Θ-superlayer, the measurement of the angular distribution differs for the projection onto the r-ϕ plane from the projection onto the r-z plane, because ambiguities in ϑ can not be solved when measuring only with single chambers. The inclination of the chamber additionally shifts the angular distribution, since the zenith of the cosmic distribution stays constant, whereas the trigger acceptance rotates with the chambers inclination. Furthermore, the angular distribution is affected by shielding effects. An asymmetric shielding of the chamber deforms the distribution accordingly.

The projection of the angular distribution onto the r-ϕ plane for a horizontal chamber without asymmetric shielding can be seen in figure 8.5. The maximum is around $\varphi = 0°$ and tracks are reconstructed up to $\varphi = \pm 58°$. Very few tracks have incident angles between $\varphi = \pm 60°$ and $\varphi = \pm 70°$.

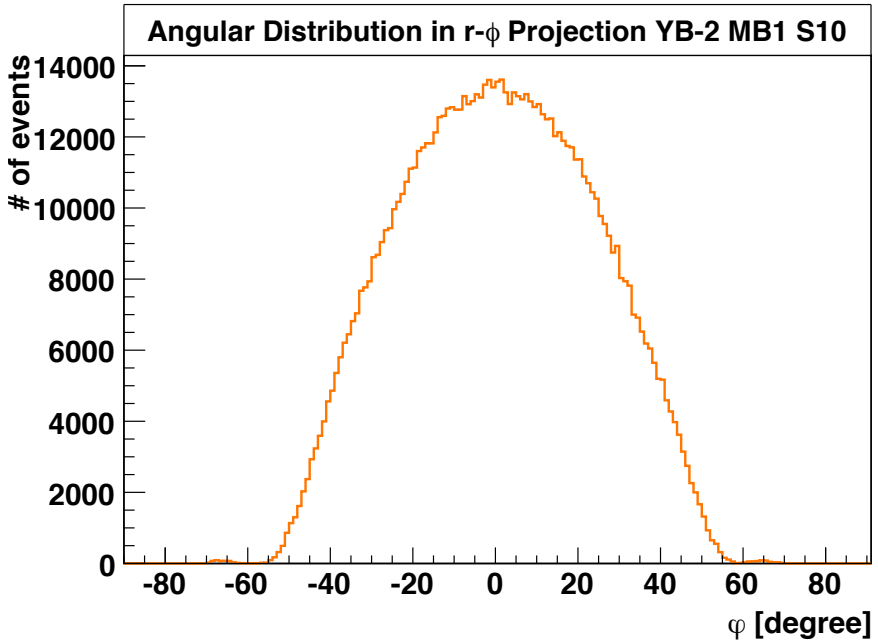

Figure 8.5: *Projection of the angular distribution of reconstructed 4D Segments onto the r-ϕ plane for a horizontal chamber.*

For some combinations of 1D RecHits two ambiguous 2D Segment candidates can be constructed, where the false segment may even have the better χ^2 and therefore is the preferred segment candidate. Since these tracks are strongly inclined, as shown in figure 6.2, they can easily be seen in the angular distribution. The segment cleaner (6.3.1) can be set to keep the candidate with the lower angle in the case of

[1]Remember, the r-ϕ plane is the bending plane of the solenoid's magnetic field.

an evident ambiguity, reducing the number of false segments. When combining the segments from both Φ-superlayers the ambiguities are solved automatically, since only the right segments matches. The remaining mismatches can be seen in figure 8.5 as very small bumps at $\varphi = \pm 66°$. The number of remaining mismatched segments on chamber level is about 0.05%. Nevertheless it is possible to correct this at higher reconstruction levels, i.e. between several chambers, when they are read out synchronously.

In figure 8.6(a) the projection of the angular distribution onto the r-ϕ plane is shown for three adjacent sectors. The horizontal sector S4, sector S5 with an inclination of 30° and S6 which is inclined by 60°. The trigger acceptance rotates with the chamber, while the cosmic ray muons are distributed around the zenith. With increasing inclination of the chamber, the peak of the angular distribution shifts to higher angles. For sector S5 to 18° and for S6 to 28°. Due to the symmetry between the sectors, the r-ϕ projection of the angular distribution of the remaining sectors shifts accordingly to the shown sectors. Sector S4 and S10 have the same angular distribution and so do sector S5 and S11 and sector S6 and S12. The sectors S2 and S8 are mirrored versions of the distribution from sector S6 and the angular distributions of sector S3 and S9 are mirrored to sector S5. Additionally, the r-ϕ projection of the angular distribution from negative chambers are mirrored with respect to the distributions from positive chambers.

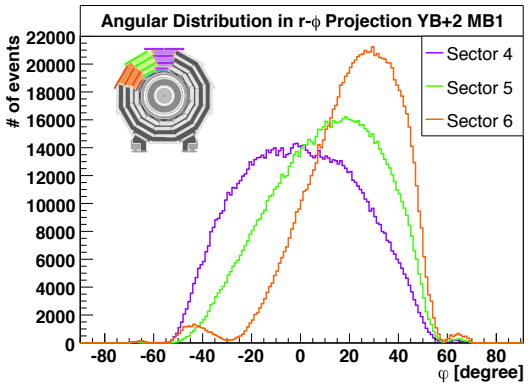

(a) *Angular distribution in r-ϕ projection for sectors S4, S5 and S6. The chamber in sector S4 is mounted horizontally, S5 is inclined by* 30° *and S6 has an inclination of* 60°.

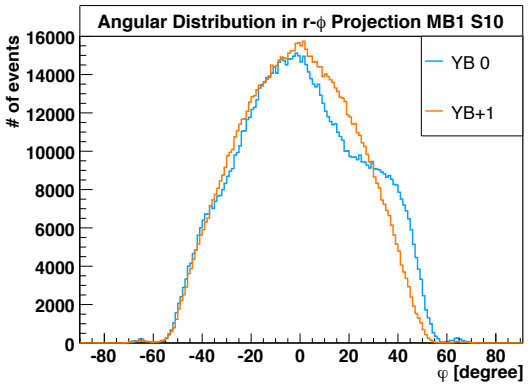

(b) *Angular distribution in r-ϕ projection for wheel YB+1 and YB0. Due to shielding, the angular distribution for YB0 is distorted.*

Figure 8.6: *r-ϕ projection of angular distributions for different sectors and different wheels.*

Figure 8.6(b) shows the r-ϕ projection of the angular distribution for the horizontal sector S10 for two different wheels. In wheel YB0, this sector was shielded by the HCAL Barrel (HB) and due to this the angular distribution is deformed. The position of the MB1 chamber in sector S10 is not centered in the barrel yoke, as

shown in figure 3.9, because the position of the chamber is determined to minimize the gaps between the chambers. Thus, the shielding due to the HB is not symmetric, and muon tracks with an incident angle around 15° are shielded by the HB.

The information of the incident angle in the projection onto the r-z plane is determined using just one superlayer, the Θ-superlayer. Therefore ambiguities cannot be solved and the angular distribution shows more misidentified tracks, visible as bumps between $\vartheta = \pm 60°$ and $\vartheta = \pm 70°$. As the inclination of the chamber due to the installation in the barrel yoke is in the r-ϕ plane, the projection of the angular distribution to the r-z plane shows no sector dependence. But the angular distribution in the r-z plane differs for chambers in the upper part of the barrel yoke from one in the lower part, due to a shielding effect. This is the same shielding effect which can be seen in the occupancy for a Θ-superlayer in section 7.2.3. The wires from the Θ-superlayer run parallel to the gap between two wheels and the outer channels were fully exposed to the cosmic ray muon flux, without shielding. The incident angles for those tracks is dominating the projection of the angular distribution to the r-z plane. Chambers in the lower part of the wheel were shielded by the neighboring wheel and don't show this effect. Figure 8.7(a) shows the angular distribution in the r-z plane and figure 8.7(b) shows a distribution with the effect of unshielded edges of the Θ-superlayer.

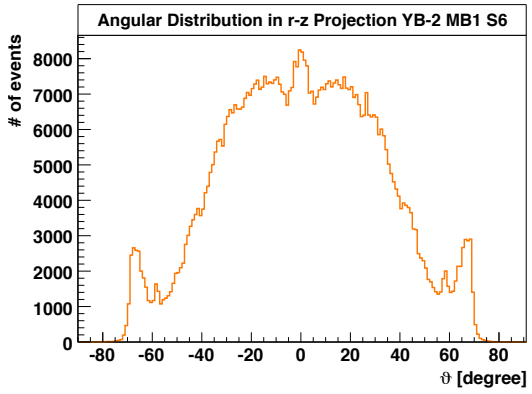

(a) *Projection of the incident angle to the r-z plane for a chamber in the upper part of the barrel yoke.*

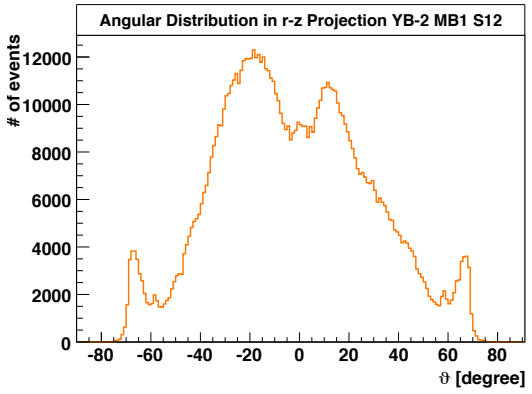

(b) *Projection of the incident angle to the r-z plane for a chamber in the lower part of the barrel yoke. Perpendicular tracks are shielded, while tracks with an incident angle around 20° could hit the chamber directly. The shielding is asymmetric, since this chamber resides in an outer wheel.*

Figure 8.7: *Angular distribution in r-z projection.*

8.4 Trigger Rates

Assuming a constant cosmic ray muon flux, the trigger rates depend on two fixed geometrical properties: Apparently the chamber's surface area has a direct influence on the number of muons passing the chamber in a given time. The inclination of the chamber affects the trigger rate, due to the angular distribution of cosmic ray muons (5.1). Thus the flux is maximal for horizontal chambers and hence the trigger rate. Besides geometrical reasons, the trigger rate depends on shielding effects and the trigger efficiency. The shielding of the chamber during the data acquisition is hard to calculate, since the barrel yoke wheel is not the only source of shielding, but also the neighboring wheels as well as parts of other subdetectors, like the endcaps. In an environment being heavily under construction, these parameters changed occasionally several times a day and are mostly undocumented. Some asymmetric shielding effects are studied in section 7.2.3. Table 8.1 shows recorded trigger rates from the commissioning runs for the different trigger configurations:

	HHandHL [Hz]				**Hanytheta [Hz]**			**Default [Hz]**			
	MB1	MB2	MB3	MB4	MB1	MB2	MB3	MB1	MB2	MB3	MB4
S02	100	110	180	230	130	160	240	155	200	250	400
S03	160	210	-	520	225	280	420	260	340	480	800
S04	-	-	530	550	-	-	470	-	-	-	740
S05	160	250	300	530	220	290	400	260	350	-	820
S06	85	130	170	230	120	170	230	170	220	260	-
S08	85	95	100	130	120	140	150	145	160	175	210
S09	160	165	195	140	240	250	260	290	305	310	210
S10	100	180	190	100	140	230	260	170	-	300	200
S11	80	120	135	320	120	150	120	140	185	250	220
S12	80	100	100	120	125	140	150	165	160	170	230

Table 8.1: *Event rates in* Hz *for different trigger configurations. For the blank fields no rates have been measured. Since MB4 chambers have no* Θ*-superlayer no data can be acquired for them in the Hanytheta configuration.*

The default trigger has the least constraints on accepting an event and hence the highest trigger rates for a given chamber. The *Hanytheta* configuration includes the requirements of the *HH+HL* configuration and extents them to the Θ-superlayer, thus the trigger rates for *Hanytheta* are above the ones for the *HH+HL* configuration.

8.5 Trigger Dependence

Comparing the reconstructed hits and segments and the derived measurement values, only very few deviations between the different trigger configurations can be seen. The occupancy (7.2) for horizontal chambers has a similar shape for the *Hanytheta*

trigger configuration and for the *HH+HL* configuration. For chambers in inclined sectors the occupancy shows a pattern of rise and fall, repeated every four cells, as mentioned in section 7.2.2. This effect is more distinct for the *HH+HL* trigger configuration (5.2.3) than for the *Hanytheta* configuration (5.2.3). Figure 8.8(a) shows the occupancy for an inclined sector in both trigger configurations, *HH+HL* and *Hanytheta*. Around channel 13 a minor drop of triggered events can be seen. The other superlayer has one dead cell in this channel and thus the BTI connected to this channel can only provide the *L* (low) trigger pattern. If for any reason the corresponding BTI in the other superlayer also just provides the *L* trigger pattern, then the requirements of the *HH+HL* trigger configuration are not fulfilled and the event does not get triggered. The number of triggered events for this channel is reduced by about 2% for the *Hanytheta* trigger configuration and by about 4% for the *HH+HL* configuration.

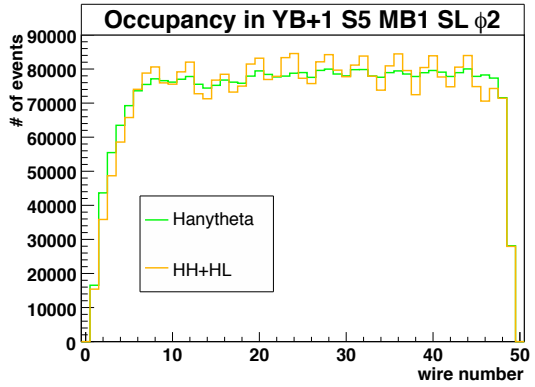

(a) *Normalized trigger dependence of the occupancy. The minor drop of events around channel 13 is due to a dead cell in the other* Φ *– superlayer and is more evident in the HH+HL trigger configuration.*

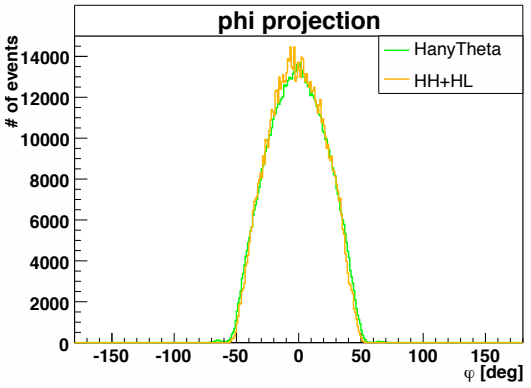

(b) *Normalized angular distribution in r-*ϕ *projection for different trigger configurations.*

Figure 8.8: *Trigger configuration dependence of the occupancy and the angular distribution.*

The angular distribution is independent of the trigger configuration. In figure 8.8(b) the projection of the incident angle onto the *r*-ϕ plane is shown for a chamber configured in the *HH+HL* trigger configuration and for the same chamber, configured in *Hanytheta* configuration. Since less events have been recorded for *HH+HL*, the distribution has been normalized to the *Hanytheta* distribution, leading to the uneven shape of the *HH+HL* distribution.

9 Chamber Quality

9.1 Meantime

9.1.1 Meantime Definition and Properties

The *meantime* is one of the key quantities for the CMS muon drift tube chambers. It is a solely geometrically based value, defined for three consecutive layers inside one superlayer, as follows: the mean of the drift-distance a measured in the first layer and c in the third layer plus the drift-distance b measured in the second layer.

$$MT = \frac{a+c}{2} + b \tag{9.1}$$

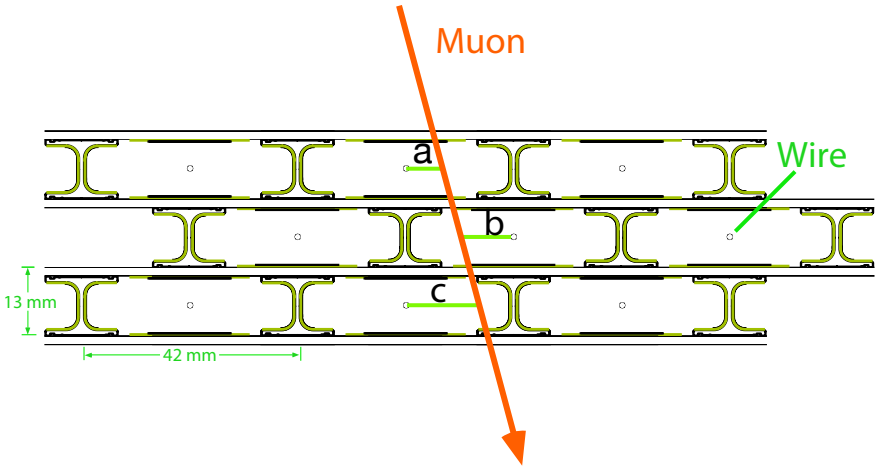

Figure 9.1: *Definition of meantime. The drift-distance is measured in three consecutive layers. [46]*

Due to the theorem on intersecting lines the mean of a and c is the distance from the straight line between the wires of the first and the third layer to the start-point of b. Thus the mean of a and c plus b is exactly the shift between the layers, which corresponds to half of the cell pitch (4.2.1), as seen in figure 9.1.

A measurement of the meantime in units of the drift-distance implies the imprecision due to the used time-to-drift-distance relation, as well as uncertainties due to a bad gas mixture and pressure differences, since the directly measured value is the drift-time, not the drift-distance. The meantime is a useful tool for the examination

of chamber quality parameters. A typical meantime distribution is shown in figure 9.2. It should peak at 21 mm, corresponding to half of the cell pitch.

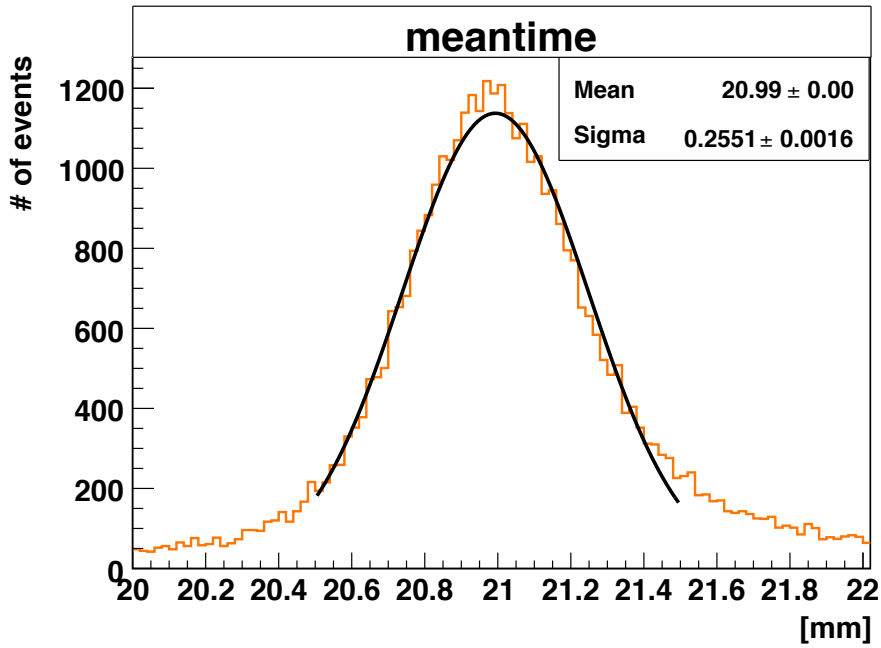

Figure 9.2: *A typical meantime distribution. The distances are taken from 4D Segments. The mean value is at* 20.99 mm

The meantime distribution tends to have some entries in the tails for lower meantimes due to δ-ray electrons (4.1) arriving at the wire earlier than the drifting secondary electrons produced by the passing muon, thus pretending shorter drift-times. The event-based correction (6.3.2) of the drift-time has to be disabled for the examination of meantimes, since the algorithm shifts the meantime to the optimal value by adjusting the drift-time and the drift-velocity, making the meantime distribution meaningless.

There are several types of meantimes. Depending on the combination of the examined layers inside one superlayer. Layers L1, L2 and L3 are used for the so-called *upper-meantime* and layers L2, L3 and L4 for the so-called *lower-meantime*. Furthermore it is distinguished on what side of the cell - in terms of left or right from the wire - the muon track passes the cell in the upper of the examined layers.

9.1.2 Performance check with the Meantime

The meantime provides the ability to check various parameters, since it compares a measured value with a known value. Chamber inherent parameters can be measured as well as problems related to the data taking during the commissioning. A chamber inherent parameter, measurable with meantimes is the precision of the positioning of the layers. Therefore the construction precision can be verified with meantimes. Inside one superlayer the layers are supposed to be shifted alternating by half a cell

width. An imprecise layer alignment results in a shift of the peak of the meantime distribution (assuming a correct wire position). According to the definition of the meantime, a shift in the second of the examined layers would shift the complete meantime by the dislocation of the layer. A shift in the position of the first or third of the examined layers results in a shift of the meantime distribution by half of the layers dislocation. By evaluating all four types of meantimes a dislocation of one layer inside a superlayer can be identified unambiguously. Table 9.1 shows all possible combinations of shifted meantimes for one dislocated layer. An example illustrating the meantime distributions for the case of one dislocated layer is given in figure 9.3. A detailed analysis on the precision of the layer alignment can be found in [46].

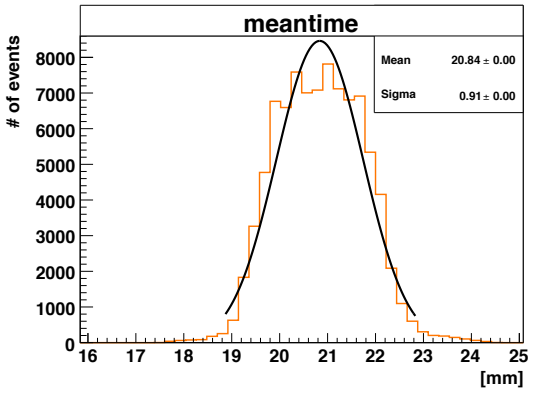

(a) *left upper meantime*

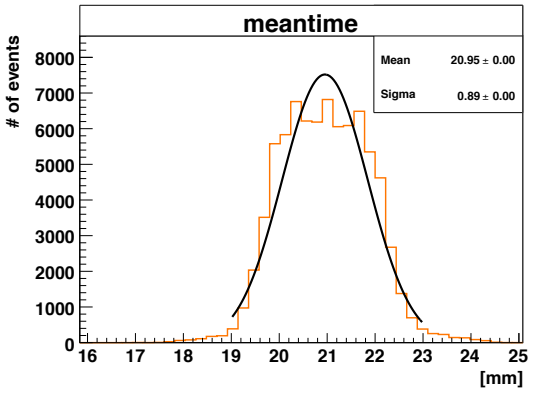

(b) *right upper meantime*

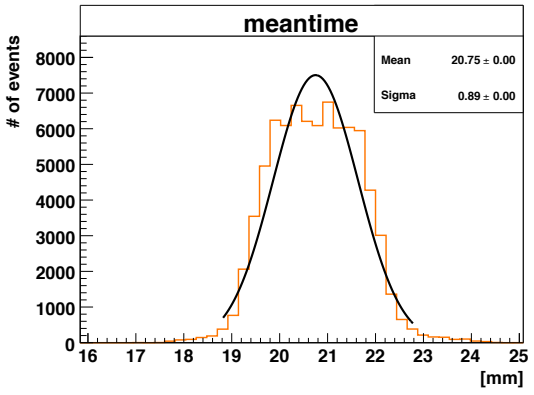

(c) *left lower meantime*

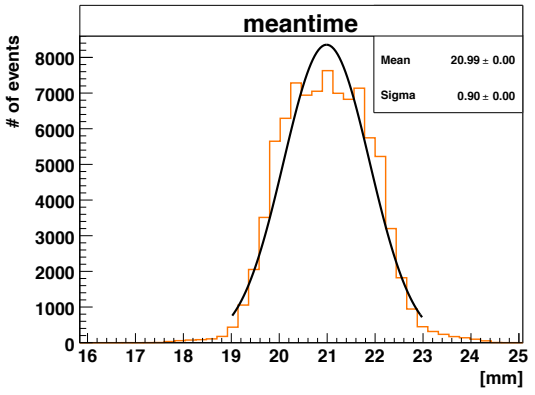

(d) *right lower meantime*

Figure 9.3: *Meantime distribution of all layers in one superlayer, with a dislocated layer.*

	L1	L2	L3	L4
MT_{LU}	$+\frac{1}{2}\Delta x$	$-\Delta x$	$+\frac{1}{2}\Delta x$	0
MT_{RU}	$-\frac{1}{2}\Delta x$	$+\Delta x$	$-\frac{1}{2}\Delta x$	0
MT_{LL}	0	$+\frac{1}{2}\Delta x$	$-\Delta x$	$+\frac{1}{2}\Delta x$
MT_{RL}	0	$-\frac{1}{2}\Delta x$	$+\Delta x$	$-\frac{1}{2}\Delta x$

Table 9.1: *Each column of this table gives the combination of shifted meantime distributions for the identification of a displaced layer. For example, a dislocation of layer 1 by Δx results in a shifted peak of the meantime distribution by $+\frac{1}{2}\Delta x$ for the peak of the left-upper meantime (MT_{LU}), a shift by $-\frac{1}{2}\Delta x$ for the right-upper meantimes (MT_{RU}) peak and no shift for the peaks of the left-lower meantime (MT_{LL}) and right-lower meantime (MT_{RL}).*

The law of error propagation connects the error of the meantime with the error of each individual time measurement. This allows to estimate the spatial resolution (9.3) of a chamber by evaluating the widths of the meantimes.

If the meantime is expressed in terms of the drift-time and not as drift distance, it represents the time the electrons would need to drift the distance of the cell pitch, which is the maximum drift-time in the cell plus the drift-time for the distance of half of the I-Beam (0.5 mm). Assuming a linear time-to-drift-distance relation and a correct layer alignment, the position of the peak of the meantime distribution gives a good estimation for the drift-velocity, since the pitch of the cell is known and the drift-time for that distance can be determined using the meantime. Using this technique, the drift-velocity computes as follows:

$$v_D = \frac{\text{cell pitch}}{\overline{t_{\mathrm{MT}}}} \tag{9.2}$$

With a few hundred events the average drift-velocity can be determined with an accuracy of about 0.2% [16].

9.1.3 Meantime studies

As a chamber inherent parameter, the meantime is expected to be independent from the inclination of the chamber. Furthermore it is expected to be constant with time. A measured meantime should be the always the same if measured under the same conditions. During the tests at the production site of the muon chambers the meantimes of all chambers have been measured with cosmic ray muons to quantify the mechanical precision of the layer position. These tests have been done for a horizontal chamber orientation. A comparison of this data with the measurements of the meantime in the commissioning is shown in figure 9.4. The mean value of the meantimes measured at the production site in Aachen (indicated by red dots) is shown in comparison with the mean value of the meantimes measured in

the commissioning at CERN (indicated with blue dots) for chambers produced in Aachen (MB1).

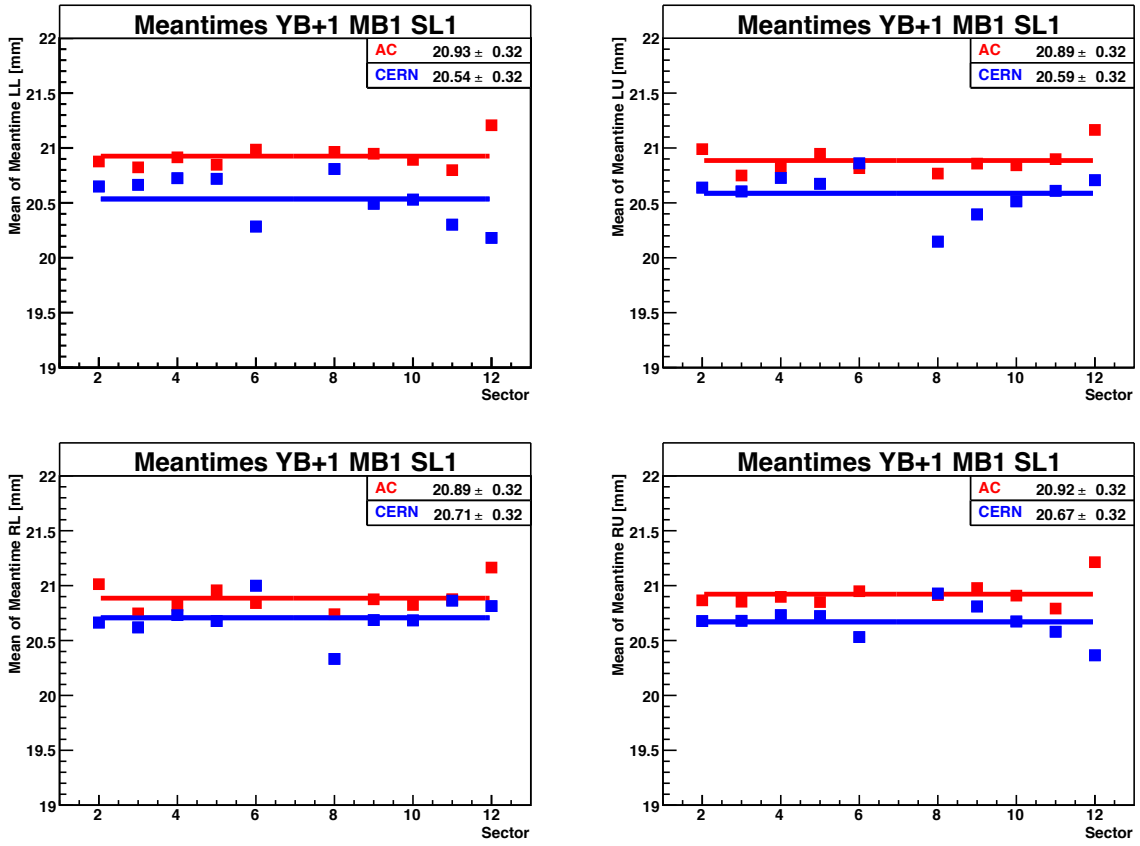

Figure 9.4: *Mean value of the meantime distributions in YB+1 MB1 SL1 commissioning data in blue, production site data of the corresponding superlayer in red.*

Both data, from the production sites and the commissioning mainly coincide, but the data taken in the commissioning tend to lower meantimes than the data taken at the teststand at the Aachen production site.

The drift-velocity, and therefore the measured meantime depends on the pressure. Naturally, the environmental pressure is a subject of constant change. The mean air pressure at the production site in Aachen is about 99.1 kPa, whereas the mean air pressure at CERN is about 97.0 kPa. Since the gas pressure in the drift tube chambers depends on the atmospheric pressure, a change of the environment has an impact on the drift-velocity. For electric fields of the strength as in the drift tube chambers the drift-velocity decreases linear by about 0.037 $\frac{\mu m/ns}{kPa}$ [64]. The difference between the mean air pressure in Aachen and at CERN of $\Delta p = 2.1\,\text{kPa}$ thus results in a change of the drift-velocity of $\Delta v_{drift} = 0.08\,\mu\text{m/ns}$. With the parametrization used in the commissioning, the reconstruction software assumes a constant drift-velocity of $v_{\text{drift}} = 54.3\,\mu\text{m/ns}$. Since the directly measured value is the drift-time, the drift-distance is calculated using the assumed drift-velocity. A change of the

real drift-velocity due to environmental changes, which is not accounted for by the software, consequently shifts the measured drift-distance.

An additional condition being different in both sets of measurement is the gas system and the gas quality. In Aachen, a gas of welding gas quality has been used, with a nominal purity of 99.7%. A measurement of the relative O_2 content at the bottle showed values between 100 ppm and 200 ppm [64]. Assuming that the contamination of the gas is due to air, the N_2 content is between 400 ppm and 800 ppm. A simulation of the drift-velocity for different purities using the software Magboltz [65] predicts an increase of the drift-velocity by about 0.09 µm/ns per 100 ppm of N_2 for the electrons drifting in an electric field of the strength as in the drift tubes chambers. The gas mixture used at CERN was the final one, with a purity of 99, 995%, corresponding to a N_2 content of about 150 ppm. Nevertheless, the gas flow at CERN was lower, which reduced the gas quality in the chambers. The gas system used was not final which sometimes had an impact on the purity of the gas in the chambers. For the final operation of CMS, each wheel will be equipped with a drift-velocity monitor system [66][64], to guarantee a quasi just in time surveillance of the electron drift speed, eliminating the uncertainties due to outer factors.

The average drift-velocity for both data sets, Aachen and CERN can be calculated following equation 9.2. Assuming a perfect alignment of the layer, the cell pitch is 21 mm. This is the position, where the meantime distribution is supposed to peak. The average of all meantimes in YB+1 MB1 SL1 from the CERN data is $\overline{MT} = 20.63\,\text{mm}$. Expressed in terms of drift-time, the average meantime is $t_{\text{MT}} = 380\,\text{ns}$, since a constant drift-velocity of $v_{\text{drift}} = 54.3\,\mu\text{m/ns}$ is assumed by the software. The average drift velocity for those chambers in the commissioning as measured with the meantimes computes as follows:

$$v_{\text{drift}}^{\text{CERN}} = \frac{\text{cell pitch}}{\overline{t_{\text{MT}}}} = \frac{21\,000\,\mu\text{m}}{380\,\text{ns}} = 55.3\,\mu\text{m/ns} \tag{9.3}$$

The mean of all YB+1 MB1 SL1 meantimes at the production site in Aachen is $\overline{MT} = 20.91\,\text{mm}$, corresponding to $t_{\text{MT}} = 385\,\text{ns}$. For the average drift-velocity of those chambers follows: $v_{\text{drift}}^{\text{AC}} = 54.5\,\mu\text{m/ns}$.

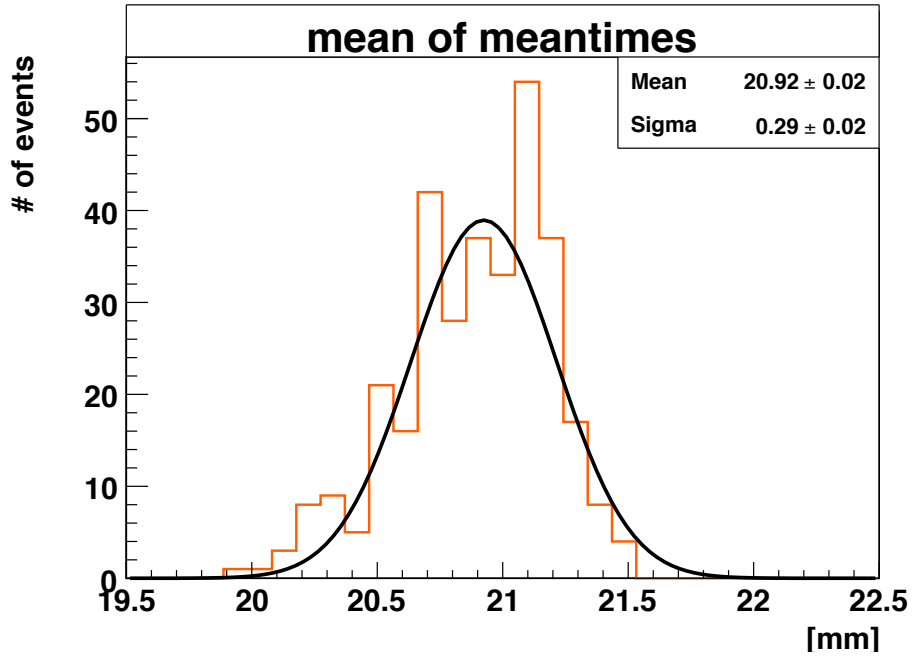

Figure 9.5: *Mean value of the meantimes for different sectors/all MB1 s*

In figure 9.5 the mean values of all meantimes from all MB1 chambers in the wheels YB0, YB+1 and YB+2 are plotted. They spread around 20.9 mm with a width of $\sigma = 290\,\mu m$. The quality control requirements ask for a precision of $\sigma_x = 250\,\mu m$ per layer. According to the relation between meantime and resolution (9.3) a spread of the meantime up to $\pm 350\,\mu m$ is sufficient according to quality control requirements.

9.2 Track Residual

9.2.1 Residual Definition and Properties

An important quality parameter is the *track residual*. It is defined as the distance between the position of a hit in the cell and the position of the fitted segment (6.3.1) inside the cell and therefore indicates the correctness of the segment.

$$RES = x_{\text{hit}} - x_{\text{segment}} \tag{9.4}$$

The segment can be a 2D Segment for the examination on superlayer-level or a 4D Segment for chamber wide studies. The segment is a straight line, close-by the hits, and normally will not square with the hit exactly due to statistical fluctuations. Deviations are as likely for both cases, that a segment is nearer to the wire than the hit oder farther. Thus the histogram of track residuals is distributed around zero. The less hits are taken into account for the segment fit, the smaller are the residuals, but the greater will be the distance to the real muon track. A typical distribution is shown in figure 9.6. The distribution has been fitted with a gaussian shape with the mean value around zero and a width of $\sigma_R = 212.5\,\mu m$.

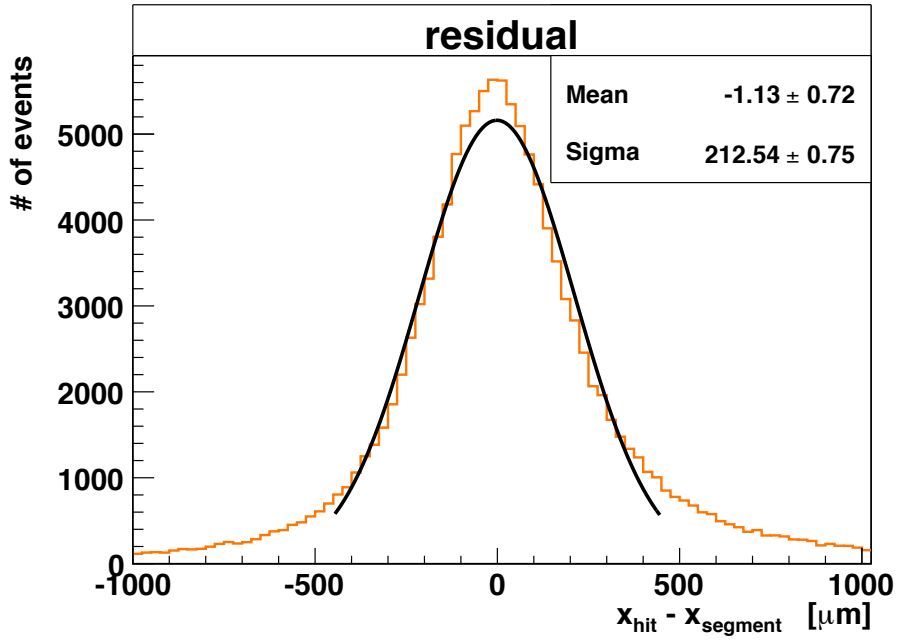

Figure 9.6: *A typical track residual distribution for a superphi segment with 8 hits. A cut has been applied to select only tracks with an inclination angle of* $|\varphi| < 10°$.

The width of the track residual distribution is a measure of the resolution (9.3) of the chamber, and underlies all factors that have an impact on the resolution. In particular, the event based correction (6.3.2) of the drift-time reduces the width of the track residual distribution.

The position of the peak of the track residual distribution is related to the precision of the determination of the time pedestal tTrig (6.3.2), offering an additional possibility to increase the precision of the correction to the drift-time. If the tTrig pedestal is a few ns too low, the measured drift-time increases by that amount, thus increasing the track residual. Since tTrig is computed for a complete superlayer and the cells are altering by half a cell pitch, a reconstructed 2D Segment track is not falsified by a minimally wrong tTrig value, but the residual will shift. With increasing error of tTrig, the reconstruction efficiency decreases.

9.2.2 Residual studies

The width of the fit of the residual distributions from all MB1 chambers in YB+1 is shown in figure 9.7. Aside from in sector S6 and sector S9 all widths are around or below 250 µm. The mean value of all widths is $\overline{\sigma_R} = 249\,\mu\text{m}$.

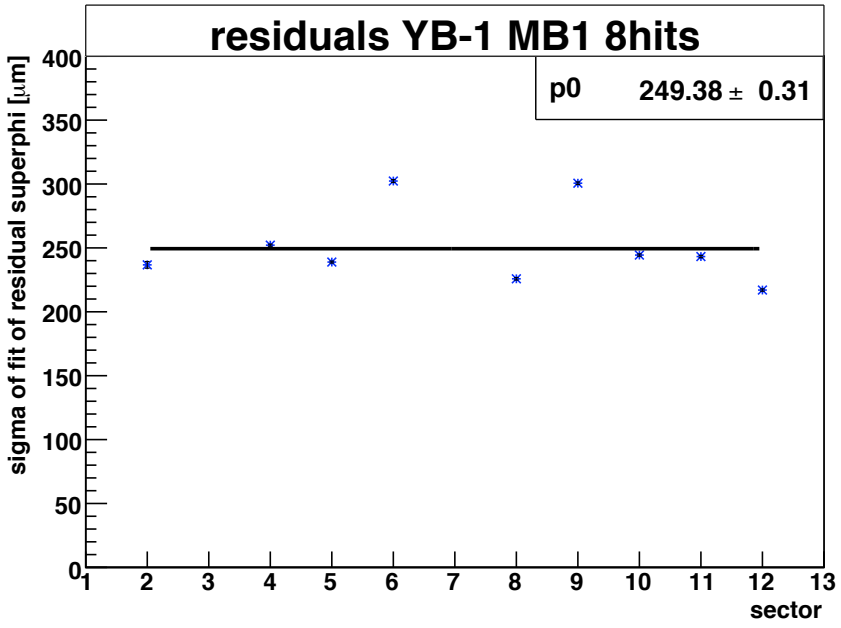

Figure 9.7: *Width of residuals in YB-1. Only superphi segments with eight hits were taken into account.*

The number of dead cells in the chambers is low enough, so that dead cells do not affect the resolution of the chamber. All chambers have less than 1% dead cells (7.2.4). Figure 9.8 shows the widths of residuals from all chambers of YB-2 MB2, in dependence of the number of dead cells. The segments included in the residual were not corrected with the event-based drift-time correction and consequently the widths of the residuals are wider. No correlation between the number of dead cells and the width of the residuals can be seen.

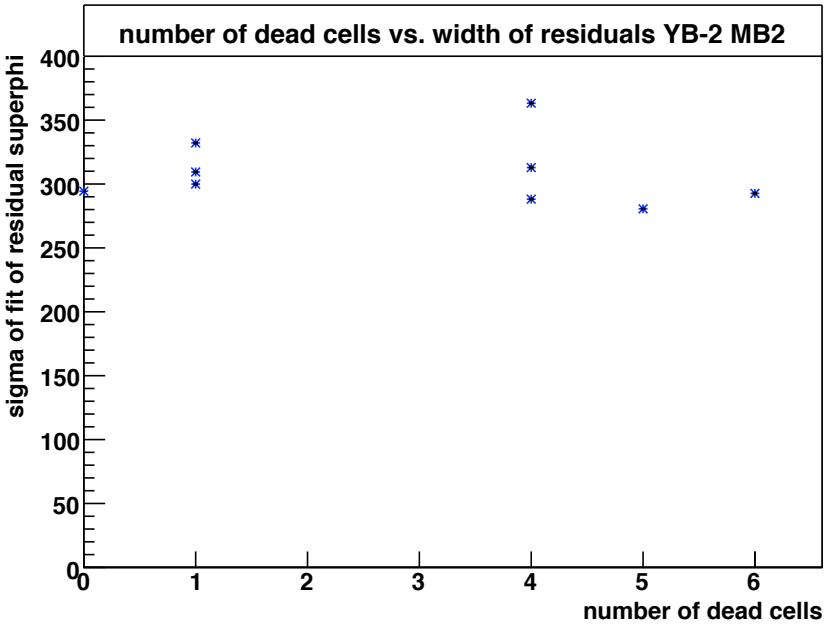

Figure 9.8: *Width of residuals in dependence of the number of dead cells for several MB2 chambers.*

9.3 Resolution

Possibly the most interesting chamber property is the spatial resolution. A precision of $\sigma_{\text{chamber}} = 100\,\mu\text{m}$ is required for the drift tube chambers to provide the desired reconstruction quality and thus momentum resolution [22]. To achieve this a resolution of $\sigma_{\text{x}} = \sqrt{8} \cdot \sigma_{\text{chamber}} \approx 250\,\mu\text{m}$ per layer is mandatory.

For an evaluation of the resolution either meantimes or track residuals can be used. The determination with track residuals relies on the relation between the width of the residual distribution and the resolution. To minimize track fit errors only residuals of segments built from the maximal number of hits are taken into account, since a track fit with fewer hits is closer to the measured hits, pretending narrower residuals, while the fit essentially has a greater distance from the real muon track.

The width σ_R of the residuals can be translated into the spatial resolution σ_x by applying a correction factor as follows: Let $(x_i|y_i)$, $i = 1 \ldots n$ be the n measured hits and $x(y) = ay + b$ the function of the straight line between the hits, where x is the coordinate in the drift plane. Assuming that the residual distance $(ay_i + b) - x_i$ is an independent normally distributed random variable, a χ^2 distribution can be constructed from the sum of its square:

$$\chi^2 = \sum_{i=1}^{n} \left(\frac{(ay_i + b) - x_i}{\sigma_x} \right)^2 \tag{9.5}$$

The expected value of the sum over the squares of the residual distance is n times the variance σ_R^2 of the residuals distribution:

$$\left\langle \left(\sum_{i=1}^{n} (ay_i + b) - x_i \right)^2 \right\rangle = n \cdot \sigma_R^2 \quad , \tag{9.6}$$

where the expected value of the χ^2 distribution is the number of degrees of freedom, here $n - 2$:

$$\langle \chi^2 \rangle = n - 2 \quad . \tag{9.7}$$

The evaluation of equation 9.6 and equation 9.7 provides:

$$\langle \chi^2 \rangle = \left\langle \sum_{i=1}^{n} \left(\frac{(ay_i + b) - x_i}{\sigma_x} \right)^2 \right\rangle = n \left(\frac{\sigma_R}{\sigma_x} \right)^2 = n - 2 \tag{9.8}$$

For the relation between the width of the residual and the spatial resolution follows:

$$\sigma_x = \sigma_R \sqrt{\frac{n}{n-2}} \tag{9.9}$$

For a residual of a phi segment with $n = 4$ hits the factor is

$$f_4 = \sqrt{\frac{n}{n-2}} = 1.414 \quad , \tag{9.10}$$

for a superphi track residual with $n = 8$ hits:

$$f_8 = \sqrt{\frac{n}{n-2}} = 1.155 \quad . \tag{9.11}$$

The relation assumes, that the track residuals have the same width in all layers. But due to a longer lever arm in respect to the center of mass of the segment the residuals of the outer layers are less wide than the residuals in the inner layers of one superlayer. In this analysis the different widths of the residuals are not taken into account, but only the sum off all residuals in one superlayer. The factor for a segment with four hits is for residuals from an outer layer $f_4^{\mathrm{L1,L4}} = \sqrt{\frac{10}{3}}$. For residuals from an inner layer the factor is $f_4^{\mathrm{L2,L3}} = \sqrt{\frac{10}{7}}$.

For the residual shown in figure 9.6 a fit with a gaussian shape in the range of $-450\,\mu\mathrm{m}$ and $450\,\mu\mathrm{m}$ provides a width of $\sigma_R = 212.5\,\mu\mathrm{m}$. Applying the correction factor for fits with 8 hits results in a resolution of $\sigma_x = 245.4$ which is compatible with the design cell resolution of $250\,\mu\mathrm{m}$.

Another possibility to measure the resolution is using the meantime (9.1). The relation between the width of the meantime distribution and the cell resolution can be derived from the law of error propagation, since the error of the meantime is the

squared sum of the errors of the individual drift-distance measurements in each cell [67].

$$\sigma_{MT} = \sqrt{\sum_{i=1}^{3} \left(\frac{\partial MT}{\partial x_i}\right)^2 \cdot \sigma_{x_i}^2} = \sqrt{\left(\frac{\sigma_{x_1}}{2}\right)^2 + \left(\frac{\sigma_{x_3}}{2}\right)^2 + \sigma_{x_2}^2} \tag{9.12}$$

Assuming that the individual σ_{x_i} are the same for all cells,

$$\sigma_{x_1} = \sigma_{x_2} = \sigma_{x_3} = \sigma_x \tag{9.13}$$

the relation between the width of the meantimes and the time resolution of the chamber is:

$$\sigma_x = \sqrt{\frac{2}{3}} \cdot \sigma_{MT} \tag{9.14}$$

The meantime distribution shown in figure 9.2 has been fitted with a wide gaussian shape in the range between 20.5 mm and 21.5 mm with a width of $\sigma_{MT} = 255.1\,\mu\text{m}$. The resulting cell resolution is $\sigma_x = 208.3\,\mu\text{m}$. Note that this resolution is for a different chamber than the resolution measured with the residual.

10 Conclusions

The commissioning was the first opportunity to operate, and to gain data with the CMS DT muon chambers in their final position in the CMS barrel yoke. On the other hand, the commissioning was the last opportunity to conduct minor repairs on the muon chambers, since after final cabling an intervention to the chambers is nearly impossible. An intense analysis of the data collected has been performed to assure the correct functioning and the desired performance of the chambers.

The commissioning involved connecting the chambers with a temporary cabling, configuring and testing of the on-chamber electronics and of course taking cosmic muon data. The subsequent data analysis had the goal to perform a debugging of both, hardware and software.

Nearly all hardware problems which occurred in the commissioning have been fixed right-away. About 30%-40% of the chambers were opened, mostly due to individual bad channels. The main interventions were due to the TRB (26), cabling errors (12), the link board (3), and due to the ROB (1). A few new dead cells have been revealed: seven in YB+1 and four in YB-2.

The intense use of the reconstruction software provided feedback to evolve and improve the CMSSW framework. A problem with a wrong geometry for one chamber and one with the segment cleaner algorithm has been discovered. The comparison with the data from the production site showed the dependence of the drift-velocity on changes of the ambient pressure and hence emphasized the need of an online drift-velocity monitoring. Various properties have been studied, like the influence of the trigger, shielding effects and the stability of the data. The chamber quality parameters have been verified to fulfill the requirements of a muon tracking device.

Last but not least, a lot of experience in working with the chambers and with the data has been gained. The CMS DT muon chambers are ready now to take data from LHC's pp collisions.

Bibliography

[1] E. Noether. Invariante Variationsprobleme. *Göttinger Nachrichten, Mathematisch-Physikalische Klasse*, pages 235–257, 1918. 5

[2] C. C. Noack. Das Noether Theorem - for pedestrians - , 1996. `http://www.itp.uni-bremen.de/~noack/noether.pdf`. 6

[3] H. Weyl. Gravitation und Elektrizität. *Sitzungsberichte der Preußischen Akademie der Wissenschaften*, 1918(26):465–478, 1918. 6

[4] H. Weyl. Eine neue Erweiterung der Relativitätstheorie. *Annalen der Physik*, 364:101–133, 1919. 6

[5] C. N. Yang and R. L. Mills. Conservation of Isotopic Spin and Isotopic Gauge Invariance. *Phys. Rev.*, 96(1):191–195, Oct 1954. 6

[6] D. Griffiths. *Introduction to Elementary Particles*. Wiley-VCH, 1987. 6, 10

[7] T. Hebbeker. Elementarteilchenphysik I. `http://web.physik.rwth-aachen.de/~hebbeker/lectures/ep1_04.html`. 6, 36, 37

[8] C. S. Wu, E. Ambler, R. W. Hayward, D. D. Hoppes, and R. P. Hudson. Experimental test of parity conservation in beta decay. *Phys. Rev.*, 105(4):1413–1415, Feb 1957. 9

[9] F. J. Hasert et al. Observation of neutrino-like interactions without muon or electron in the Gargamelle neutrino experiment. *Physics Letters B*, 46(1):138–140, 1973. 9

[10] Gargamelle: First Neutral Current, Juli 1973. `http://cdsweb.cern.ch/record/39468`. 10

[11] Nobel Prize 1979. `http://nobelprize.org/nobel_prizes/physics/laureates/1979/`. 10

[12] W.-M. Yao et al. Review of Particle Physics. *Journal of Physics G*, 33:1+, 2006. 10, 36, 37, 49, 50, 51, 52, 53

[13] J. Goldstone, A.s Salam, and S. Weinberg. Broken symmetries. *Phys. Rev.*, 127(3):965–970, Aug 1962. 12

[14] B. Berger. Deconstruction: Large Hadron Collider . *Symmetry*, 03(06), August 2006. 16

[15] K. Bachmann. Die Weltmaschine. *GEO Magazin*, 05:118–142, May 2007. `http://cms-project-cmsinfo.web.cern.ch/cms-project-cmsinfo/Media/Publications/CMStimes/2007/05_07/`. 17

[16] CMS Collaboration. *CMS Physics. Technical Design Report (Vol. 1: Detector Performance and Software)*. CERN-LHCC-2006-01, 2006. 18, 21, 22, 23, 26, 28, 61, 98

[17] CMS Collaboration. The CMS experiment at the CERN LHC. *Journal of Instrumentation*, 8, 8 2008. 19, 21, 23, 24, 25, 27, 28, 29, 30, 31, 42, 44, 46

[18] CMS Collaboration. *CMS The Tracker Project Technical Design Report*. CERN-LHCC-98-6, 1998. 20

[19] CMS Collaboration. *CMS ECAL Technical Design Report*. CERN-LHCC-1997-33, 1997. 21, 22

[20] CMS Collaboration. *The Hadron Calorimeter Technical Design Report*. CERN-LHCC-1997-31, 1997. 23

[21] CERN Document Server. `http://cds.cern.ch/`. 27, 33, 34

[22] CMS Collaboration. *The Muon Project - Technical Design Report*. CERN-LHCC-97-32, 1997. 28, 41, 47, 104

[23] S. H. Ahn et al. Performance of a large forward resistive plate chamber for the CMS/LHC under high radiation environment. *Nuclear Instruments and Methods in Physics Research A*, 469:323–330, August 2001. 28

[24] CMS Collaboration. *The TriDAS Project: Technical Design Report, Vol. 1: The Trigger Systems*. CERN-LHCC-2000-038, 2000. 31

[25] CMS Collaboration. *The TriDAS Project: Technical Design Report, Vol. 2: Data Acquisition and High-Level Trigger*. CERN-LHCC-02-26, 2002. 32

[26] F. Sauli. *Principles of Operation of Multiwire Proportional and Drift Chambers*. CERN 77-09, 1977. 35, 39

[27] J. S. Townsend. *Electrons in Gases*. Hutchinson, London, 1947. 38

[28] S. A. Korff. *Electron and nuclear counters: theory and use Electron and nuclear counters: theory and use Electron and Nuclear Counters: Theory and Use*. Van Nostrand, 1946. 39

[29] W. J. Price. *Nuclear Radiation Detection*. McGraw-Hill, New York, 1958. 40

[30] H. Reithler. Personal Homepage. `http://web.physik.rwth-aachen.de/~reithler/`. 43

[31] M. Aguilar-Benítez et al. Construction and test of the final CMS Barrel Drift Tube Muon Chamber prototype. *Nuclear Instruments and Methods in Physics Research A*, 480:658–669, March 2002. 43

[32] F. Gonella and M. Pegoraro. A prototype frontend ASIC for the readout of the drift tubes of CMS barrel muon chambers. *4th Workshop on Electronics for LHC Experiments*, CERN-LHCC-98-036:257, 1998. `http://cdsweb.cern.ch/record/1062709/`. 44

[33] C.F. Bedoya, J. Marin, J.C. Oller, and C. Willmott. Electronics for the CMS muon drift tube chambers: the read-out minicrate. *Nuclear Science Symposium Conference Record, 2004 IEEE*, 2:1309–1313 Vol. 2, October 2004. 45

[34] J. Christiansen. High performance time to digital converter. *CERN/EP – MIC*, 2002. 45

[35] F. Gasparini et al. Bunch crossing identification at LHC using a mean-timer technique. *Nuclear Instruments and Methods in Physics Research A*, 336:91–97, November 1993. 45

[36] C. Albajar et al. Test beam analysis of the first CMS drift tube muon chamber. *Nuclear Instruments and Methods in Physics Research A*, 525:465–484, June 2004. 49

[37] H.V. Klapdor-Kleingrothaus and K. Zuber. *Teilchenastrophysik*. Teubner Studienbücher. Teubner, Stuttgart, Germany, 1997. 49

[38] J. F. Ziegler. Terrestrial cosmic rays. *IBM J. Res. Dev.*, 40(1):19–39, 1996. 49

[39] T. Hebbeker and C. Timmermans. A compilation of high energy atmospheric muon data at sea level. *Astroparticle Physics*, 18:107–127, August 2002. arXiv:hep-ph/0102042. 49

[40] Pierre Auger Observatory. `http://www.auger.org/`. 49

[41] Cosmic Ray Flux versus Particle Energy. `http://commons.wikimedia.org/wiki/Image:Cosmic_ray_flux_versus_particle_energy.svg`. 50

[42] T. K. Gaisser. *Cosmic Rays and Particle Physics*. Cambridge University Press, January 1991. 51

[43] MINOS Collaboration. Measurement of the atmospheric muon charge ratio at tev energies with minos. 2007. arXiv:0705.3815v4 [hep-ex]. 52

[44] L3 Collaboration. Measurement of the Atmospheric Muon Spectrum from 20 to 3000 GeV. *Physics Letters B*, 598:15, 2004. arXiv:hep-ex/0408114v1. 52

[45] C. Autermann. Funktionstests von CMS-Myon-Kammern. Diplomarbeit, Phys. Inst. IIIA, RWTH Aachen/Germany, May 2002. 53, 76

[46] R. Mameghani. Analysis of Cosmic Muons Measured in CMS Drift Chambers. Diplomarbeit, RWTH Aachen, August 2004. 53, 95, 97

[47] M. Sowa. Data Acquisition (DAQ) System der CMS-Myonkammern. `http://web.physik.rwth-aachen.de/~sowa/`. 56

[48] J.M. Cela, C. Fernández, and C. Willmott. Read-Out Minicrate User Manual, 2006. `http://wwwae.ciemat.es/cms/DTE/mc_ing.htm`. 56

[49] IEEE Standard Test Access Port and Boundary-Scan Architecture. *IEEE Std 1149.1-2001*, 2001. 56

[50] LabVIEW. `http://www.ni.com/labview/`. 56

[51] CMS DT Commissioning Site. `http://dt-sx5.web.cern.ch/dt-sx5/`. 60

[52] CMSSW. `https://twiki.cern.ch/twiki/bin/view/CMS/WorkBookCMSSWFramework`. 63

[53] CMS. The CMS Workbook. `https://twiki.cern.ch/twiki/bin/view/CMS/WorkBook`. 63

[54] ORCA. `http://cmsdoc.cern.ch/orca/`. 63

[55] ROOT. `http://root.cern.ch/`. 63

[56] P. Biallass and T. Hebbeker. Improved Parametrization of the Cosmic Muon Flux for the Generator CMSCGEN. *CMS-IN-2007/033*, 2007. 64

[57] T. Hebbeker and A. Korn. Simulation Programs for the L3+Cosmics Experiment, 1998. `http://www.physik.rwth-aachen.de/~hebbeker/l3csim.pdf`. 64

[58] J. Puerta-Pelayo, M. C. Fouz-Iglesias, and P. García-Abia. Parametrization of the Response of the Muon Barrel Drift Tubes. *CMS-NOTE-2005-018*, October 2005. 65

[59] SQLite. `http://www.sqlite.org/`. 69

[60] Oracle. `http://www.oracle.com/`. 69

[61] K. Hoepfner et al. The CMS Precision Muons Chambers in the Magnet Test Cosmic Challenge (MTCC). *CMS-NOTE in perparation*, August 2007. 69

[62] A. Meneguzzo. Drift tubes chambers: A track parameters fit, September 2006. `http://www.pd.infn.it/~ameneg/t0seg/4parfit_DTseg.pdf`. 70

[63] M. C. Fouz. Test pulse analysis on recent runs. `http://indico.cern.ch/conferenceDisplay.py?confId=3090`. 87

[64] J. Frangenheim. Measurements of the drift velocity using a small gas chamber for monitoring of the CMS muon system. Diplomarbeit, RWTH Aachen, June 2007. 99, 100

[65] S. F. Biagi. Monte Carlo simulation of electron drift and diffusion in counting gases under the influence of electric and magnetic fields. *Nuclear Instruments and Methods in Physics Research A*, 421:234–240, January 1999. 100

[66] G. Altenhöfer. Development of a Drift Chamber for Drift Velocity Monitoring in the CMS Barrel Muon System. Diplomarbeit, RWTH Aachen, May 2006. 100

[67] J. Puerta Pelayo. *Estudio sobre las Camaras de Tubos de Deriva para el Espectrometro de Muones del Experimento CMS*. PhD thesis, Ciemat, Madrid/Spain, January 2004. 106

List of Figures

List of Tables

Acknowledgements

First of all I want to thank Prof. Dr. T. Hebbeker for accepting me in his group, giving me the opportunity to work on the CMS experiment and encouraging me to work directly with the detector at CERN, as well as presenting my research findings on several conferences and to enable me to attend the fall school for high energy physics in Maria Laach.

Thank you to Prof. Dr. C. Wiebusch for being my second referee.

For lots of help with words and deeds I want to thank my supervisor Dr. K. Hoepfner, for taking time and always being willing to answer my questions, review my work and for the help in gaining comprehension of detector physics in many conversations and also via email and telephone. Also thank you very much for proofreading of this diploma thesis.

Thank also goes to P. Biallass and C. Hof for introducing me into the world of ORCA and CMSSW , to G. Altenhöfer and M. Sowa, with whom I shared my office and to M. Bontenackels and J. Frangenheim for discussions.

A very special thanks goes to my friend Dr. Elma Kerz for exceptional help, support and motivation.

For her continuos support I want to thank my partner Ines Schrader.

Finally I want to thank my family, especially my parents for always believing in me and being there.